ISSN 2981-0388

International Journal of

Iron & Steel Society of Iran

# Iron & Steel Society of Iran

2022 Volume 19 Number 2

Isfahan University of Technology

Isfahan University of Technology

Iron & Steel Society of Iran

# International Journal of
# Iron & Steel Society of Iran

2022 VOLUME 19 NUMBER 2

Published each six months by Iron and Steel Society of Iran
with collaboration of Isfahan University of Technology

**International Journal of Iron & Steel Society of Iran**
**(Int. J. of ISSI)**

**Managing Editor: Prof. A. Najafizadeh** (Isfahan University of Technology, Iran)

**Editor-in-Chief: Prof. A. Saidi** (Isfahan University of Technology, Iran)

**Editorial Board**
**Prof. A. Abbaschian** (Materials Eng. Dept., University of Florida, USA)
**Prof. B. Bavarian** (Materials Eng. Dept., University of California, USA)
**Prof. J. H. Beynon** (Faculty of Engineering & Industrial Sciences, Swinburne University of Technology, Australia)
**Prof. T. Chandra** (Materials Eng. Dept., University of Wollongong, Australia)
**Prof. A. J. DeArdo** (Materials Eng. Dept., University of Pittsburgh, USA)
**Prof. H. Edris** (Materials Eng. Dept., Isfahan University of Technology, Iran)
**Prof. I. Garcia** (Materials Eng. Dept., University of Pittsburgh, USA)
**Prof. H. Henein** (Materials Eng. Dept., University of Alberta, Canada)
**Prof. P. Hodgson** (Materials Eng. Dept., Deakin University, Australia)
**Prof. M. Jahazi** (Mining Metals and Materials Eng. Dept., Iran University of Science of Technology, Iran)
**Prof. S. A. Jenabali Jahromi** (Materials Eng. Dept., Shiraz University, Iran)
**Prof. J. J. Jonas** (Mining Metals and Materials Eng. Dept., McGill University, Canada)
**Prof. N. Kanani** (Materials Science Department, Technical University of Berlin, Germany)
**Prof. A. Kermanpur** (Materials Eng. Dept., Isfahan University of Technology)
**Prof. M. Moshksar** (Materials Eng. Dept., Shiraz University, Iran)
**Prof. A. Najafizadeh** (Materials Eng. Dept., Isfahan University of Technology, Iran)
**Prof. K. Raeissi** (Materials Eng. Dept., Isfahan University of Technology, Iran)
**Prof. R. A. Rapp** (Materials Eng. Dept., Ohio State University, USA)
**Prof. A. Saatchi** (Materials Eng. Dept., Isfahan University of Technology, Iran)
**Prof. A. Saidi** (Materials Eng. Dept., Isfahan University of Technology, Iran)
**Prof. T. Sakai** (Mechanical Engineering & Intelligent Systems Dept., University of Electro Communications, Japan)
**Prof. M. Shamanian** (Materials Eng. Dept., Isfahan University of Technology, Iran)
**Prof. A. Shafyei** (Materials Eng. Dept., Isfahan University of Technology, Iran)
**Prof. R. W. Waterhouse** (Materials Eng. Dept., University of Nottingham, UK)
**Prof. J. Wood** (Materials Eng. Dept., University of Nottingham, UK)
**Prof. H. Yoozbashizadeh** (Materials Science and Eng. Dept., Sharif University of Technology, Iran)
**Dr. E. Keshavarz Alamdari** (Mining & Metallurgical Eng. Dept., Amirkabir University of Technology, Iran)

**Executive Editor:** Arash Etemad
**Typographer:** Marzieh Amini
**Publisher:** Iron & Steel Society of Iran
**Language Editor:** A. Faegh

International Journal of Iron and Steel Society of Iran is published each six month by Iron and Steel Society of Iran with collaboration of Isfahan University of Technology. Annual subscription rates are as follows: for university departments, libraries, industrials, other multiple-reader institutions in Iran 3000000 Rials and for individuals 2000000 Rials. In other countries 200 US Dollars (including packing and postage).

**Iron & Steel Society of Iran**
No A306, 12th street, Isfahan Science and Technology Town,
Isfahan University of Technology, Isfahan, 84156-83228, Iran.
Tel: +98 31 33932121-24 Fax: +98 31 33932125
Web: journal.issiran.com E-mail: journal@issiran.com

International Journal of Iron & Steel of Iran

## Referees for This Issue

**Dr. H. Mirzadeh**
*(Faculty of Metallurgy and Materials Engineering, University of Tehran)*

**Dr. A. R. Mashreghi**
*(Department of Materials & Mining Engineering, University of Yazd, Yazd, Iran)*

**Dr. M. Mosalaei**
*(Department of Materials & Mining Engineering, University of Yazd, Yazd, Iran)*

**Dr. H. Ramezanalizadeh**
*(Department of Materials and Polymer Engineering, Faculty of Engineering; Hakim Sabzevari University)*

**Dr. S. Bakhshi**
*(Department of Materials Engineering, Malek Ashtar, University of Technology, Iran)*

**Dr. H. Rastegari**
*(Department of Mechanical and Materials Engineering, Birjand University of Technology, Birjand, Iran)*

**Dr. M. R. Nasre Esfahani**
*(Institute of materials and energy, Isfahan, Iran)*

**Dr. Z. Ebrahimi**
*(Department of Mechanical Enginneering, Payame Noor University (PNU), Tehran, Iran)*

**Dr. M. Omidi**
*(Department of Materials Engineering, Najafabad Branch, Islamic Azad University, Isfahan, Iran)*

**Dr. A. Arabsolghar**
*(Department of Mechanical Engineering, Vali-e-Asr University, Rafsanjan, Iran)*

**Dr. Y. Yaghubinezhad**
*(Material Science and Engineering, Birjand University of Technology, Birjand, Iran)*

**Dr. M. H. Fotros**
*(Department of Economics, Bu Ali Sina University, Hamadan, Iran)*

**Dr. M. Kheirandish**
*(Department of Economics, Administrative Sciences, Gonbadkavos University)*

**Dr. M. H. Ranjbar**
*(Dean of Bandar Abbas Azad University)*

International Journal of ISSI, Vol. 19(2022), No. 2, pp. 1-4

# A simple metallographic technique for revealing prior-austenite grain boundaries in CK45 steel

**F. Moosavi *[1], H. H. Amel-Farzad [2]**

*[1] Bu-Ali Sina University, Dept. of Material Engineering, Hamedan, Iran*
*[2] Tarbiat Modares University, Dept. of Material Engineering, Tehran, Iran*

## Abstract

CK45 steel is medium carbon steel that has a wide range of applications in the production of widely used parts such as shafts, gears, axles, crankshafts, forging, rails, etc. Austenitizing is the first step in most heat treatment processes for steel. Revealing austenite grain boundaries is very important because the austenite grains have a significant influence on steel properties. Because no research has been done on the detection of prior-austenite grain boundaries of CK45 steel, our main aim in this paper is to reveal the prior-austenite grains of this steel. We investigated two methods of chemical etching and oxidation etching to reveal prior-austenite grains boundaries of CK45 steel. Samples of CK45 with different structures(martensite, bainite, ferrite-perlite) steel were examined, and the optical microscopic images showed that the boundaries of the austenite grains were well visible with oxidation etching while with the chemical etching method, only the structure of the steels was determined.

*Keywords:* CK45 steel, Prior austenite grain boundary, Oxidation etching, Microstructure.

## 1. Introduction

Medium carbon steels are carbon steels that usually have a carbon content of between 0.30-0.55 % and a manganese content of between 0.60-1.65 % [1]. The most common use of medium carbon steels is in the manufacture of shafts, gears, axles, crankshafts, forging, rail axles, and railway wheels [2]. CK45 carbon steel is medium carbon steel that is widely used in various industries such as auto and engine parts and due to its low cost, this steel is regularly used in the manufacture of pump shafts and hydraulic clamps [3, 4]. For metallurgists to make high-quality steels, appropriate metallographic techniques are needed to characterize microstructural features such as phases, grain boundaries, and precipitates [5]. Austenitizing is the first step in most heat treatment processes of steel [6] also determining the prior-austenite grain size (PAGS) in steel is very important because of its effect on the transformation taking place during cooling, and thus, on the final properties. In fact, because of its significant impact on microstructure and mechanical, electrical, and magnetical properties, the accurate determination of the prior-austenite grain size of steels has received a lot of attention in metallurgical studies. Since new steels come to market every year, dependable methods for revealing the austenite grain boundaries in a wide range of steel compositions are needed [7–10]. Many methods have been used for revealing the austenite grain boundaries in steels [11]. In general, the methods of revealing austenite grain boundaries are divided into two categories: a) Direct methods: Use a high-temperature microscope to observe austenite grain boundaries at temperatures above the critical point, $A_{c3}$; b) Indirect methods: Methods for observing austenite boundaries at room temperature, the most important of these methods are the following: Chemical Etching (CE) method [12,13], Carburization method [14-16], Oxidation etching method [17], Thermal etching (TE) method [18]. Among various methods to reveal prior-austenite grains, chemical etch-

---

**Corresponding author*
*Email: Fateme.moosavi68@gmail.com*
*Address: Bu-Ali Sina University, Dept. of Material Engineering, Hamedan, Iran*
*1. M. Sc*
*2. Assistant Professor*

ing is one of the most practical and widely performed methods [19], but revealing austenite grain boundaries by chemical etching could be a difficult task, especially for medium-carbon steel that showed sensibility to chemical etching [20]. In this work, we investigated two methods for the detection of prior-austenite grains in medium-carbon steel. The first method is to use an etchant based on picric acid, which has been used to reveal the primary austenite grains of several types of steels. In the second method, we used oxidation etching to reveal prior-austenite grain boundaries. The oxidation etching method involves heating a polished surface of the sample at austenitization temperatures in a furnace with an oxidizing atmosphere where the grain boundaries are revealed either by oxide accumulation or by carburizing the grain boundaries. Each of these methods was used separately to reveal prior-austenite grain boundaries in three medium-carbon steel sheets with different structures.

## 2. Materials and experimental procedure

The chemical composition of the steel is given in Table 1. To reveal the austenite grain boundaries, the specimens were first cut by a cutter (BUEHLER, America) of a CK45 bar. Six machined cylindrical specimens of 10 mm in length and 12 mm in diameter were used for this examination.

### 2.1. The first method: Chemical etching

In the first step, three of the samples were heat treated to obtain perlite, martensite, and bainite structures, then we used an etchant based on picric acid and a wetting agent for the detection of prior-austenite grain boundaries. The etching solution used consisted of 10 g of $CrO_3$, 50 g of NaOH, 1.5 g of picric acid, and 100 ml of distilled water. To make this solution, we first added $CrO_3$ to distilled water and then added sodium hydroxide(NaOH). The addition of NaOH should be done slowly because it generates a lot of heat and finally we add picric acid to the solution. In this method, the samples do not need to be heated before etching. This solution should be used at 120°C temperature due to the release of toxic fumes under the hood.

### 2.2. The second method: Oxidation etching

First, the surfaces of the other three specimens were sanded and then polished vertically to the main axis of the cylinder using standard metallographic methods, so that the cross sections of the samples are well glossy. Polished specimens are heated at a rate of 14°C/min to the above austenitization temperature (815°C) in the furnace (TC-Nicr) with oxidizing atmosphere, and the specimens are held for 1h at this temperature. Then to obtain perlite, martensite, and bainite structures respectively, one of the specimens was exited of the furnace and cooled in air, the second specimen was cooled in oil and the third specimen was austempered. For austempering, the specimens cooled to 400°C and remained at this temperature for 2h(in molten salt). In the next step, etching to reveal austenite grain boundaries was carried out with Nital-2% solution (2 ml $HNO_3$ + 98 ml of ethanol ($C_2H_5OH$)) etchant. The metallographic survey of specimens was done with an optical microscope Nikon E 100.

## 3. Results and discussion

Figure 1(a, b, c) shows the images obtained for pearlite, martensite, and bainite structures for CK45 steel after using the chemical etching method. This method was suitable for detecting prior-austenite grains boundaries in a wide range of steels with different structures but was not suitable for the CK45 steel tested and nothing other than the structure of the samples was detected, as can be seen from Figure 1.

Table 1. Chemical compositions of CK45 carbon steel bars.

| Fe | C | Si | Mn | P | S |
|---|---|---|---|---|---|
| balance | (0.42–0.5)% | 0.25% | 0.75% | max 0.040% | max 0.040% |

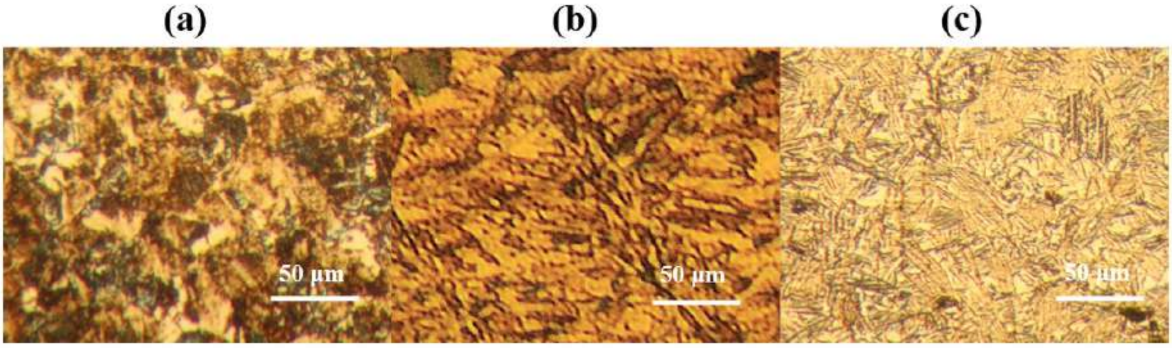

Fig. 1. Optical micrographs of: a)pearlite, b)martensite and c)bainite structures for CK45 steel.

When the specimens were held in the furnace (815$^{o}$C for 1h), their surfaces are starting to oxidation, and a film of oxide formed on the samples' surfaces, as shown in Fig 2. Since austenite grain boundaries have a greater chemical potential than other parts of the surface, they are more oxidate. The oxidation method depends on the fact that when steels are heated in an oxidizing atmosphere, oxidation takes place in part preferentially along the grain boundaries, therefore the grain boundaries are revealed by oxide accumulation. Thus before inspecting to remove this thin film, the surfaces slightly were sanded with 2000 sandpaper and then polished with alumina particles. With etching austenite, grain boundaries and structure of steels were revealed better.

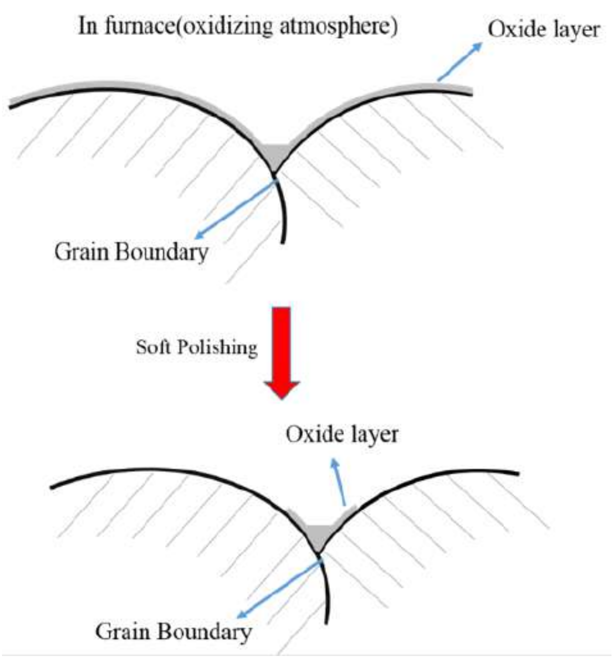

Fig. 2. Schematic of prior austenite grain boundary detection using oxidation method.

Fig 3 shows images obtained for martensitic CK45 steel heat treated at 850$^{o}$C for 1h. At low magnification, images in Fig. 3a and more magnification (Fig. 3b) show a network of grain boundaries clearly. Fig. 4a shows the results obtained for the bainite specimen after heat treatment and etching and Fig. 4b shows a higher magnification image of the microstructure for this specimen and in both images, austenite grain boundaries have been seen truly. The austenite grain boundaries and microstructure of the specimen with the ferrite-perlite structure are shown in Fig. 5(a,b). Fig. 5b shows a higher magnification image, as shown, light areas represent ferrite and dark areas represent pearlite structure. From these results, it is obvious that using the applied method in this study is extremely useful for revealing the austenite grain boundaries in a different micro-structure of CK45 steels.

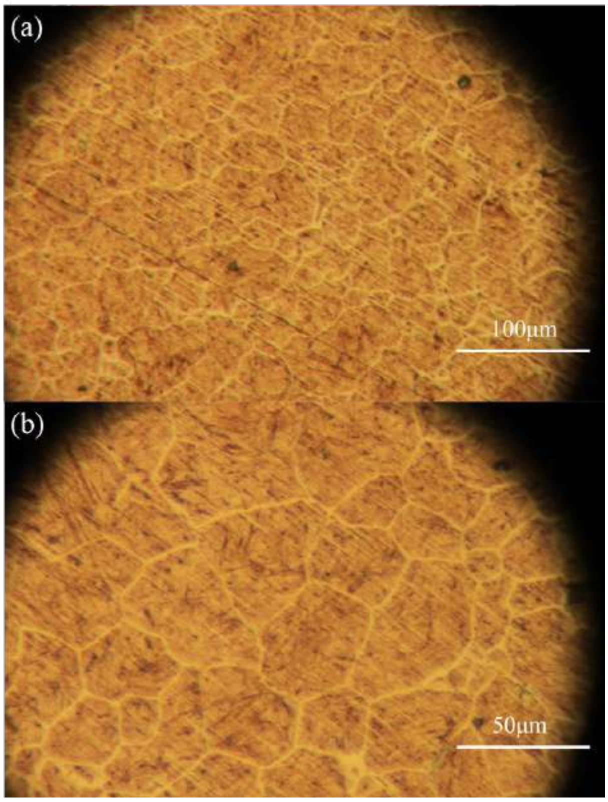

Fig. 3. Optical micrographs of the austenite grains and martensitic structure, a)200x, b)400x.

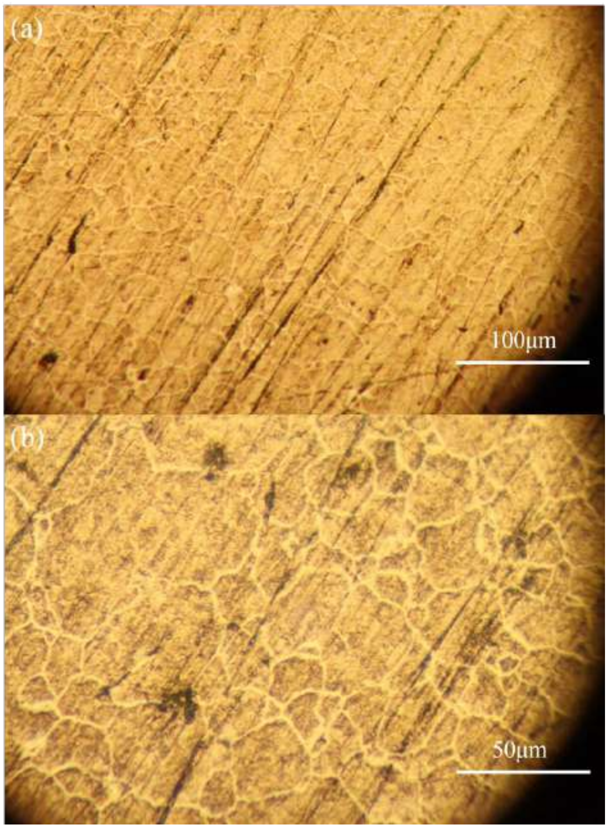

Fig. 4. Optical micrographs of the austenite grains and bainite structure, a)200x, b)400x.

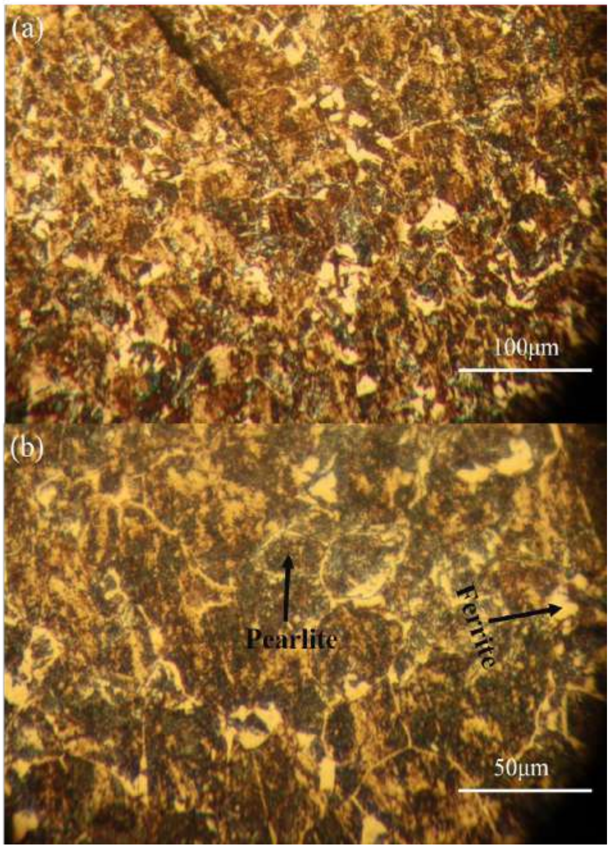

Fig. 5. Optical micrographs of the austenite grains and ferrite-perlite structure, a)200x, b)400x.

## 4. Conclusions

Revealing the austenite grain boundaries is an important step in the characterization of steel. We first used an etchant based on picric acid and a wetting agent to reveal the prior-austenite grain boundary of CK45 steel with three structures of perlite, bainite, and martensite; but the results of optical microscopy showed that the chemical etching solution used did not show sensitivity to the appearance of prior-austenite grain boundaries. Therefore, we used a two-stage method of heat treatment (oxidation) and then etching to reveal the boundaries of the prior austenite grains. Prior-austenite grain boundaries of three structures of CK45 steel (ferrite-perlite, bainite, martensite) were well revealed.

## References

[1] G. E. TOTTEN: Steel heat treatment: metallurgy and technologies, CRC press, 2006, 17.

[2] R. Singh: Applied Welding Engineering: Processes, Codes, and Standards, Butterworth-Heinemann, Oxford, UK, (2020).

[3] M. Rafati, A. Mostafapour, H. Laieghi, M. Chandra Somani, J. Kömi: Mater., 14.15 (2021), 4098.

[4] K. D. Selman: Engineering and technology journal., 29(8) (2011), 1610-1618.

[5] D. San Martin., P.E.J. Rivera Diaz Del Castillo, E. Peekstok, S. Zwaag: Mater. Charact., 58 (2007), 455.

[6] Y. Prawoto, N. Jasmawati, K. Sumeru: Mater. Sci. Eng., 28.5 (2012), 461.

[7] H. Ohtani, F. Terasaki, T. Kunitake: Tetsu to Hagané., 58.3 (1972), 434-451.

[8] NJ. Petch: Journal of the Iron and Steel institute., 174 (1953), 25.

[9] A. Grange: Strengthening steel by austenite grain refinement, ASM Trans Quart, 59.1 (1966), 26.

[10] D. San Martin, Y. Palizdar, R.C. Cochrane, R. Brydson,; A.J. Scott: Mater. Charact., 61 (2010), 584.

[11] American Society for Testing and Materials, Book of ASTM Standards Part 31, E-112-63, Standard Methods of Estimating the Average Grain Size of Metals, Philadelphia, American Society for Testing and Materials, (1969), 444.

[12] GF. Vander Voort: Metallography: principles and practice, McGraw-Hill, New York, (1984), 219.

[13] H. Modin, S.Modin: Metallurgical microscopy. Elsevier, (2016).

[14] E. Schacht, J. Richter: P, M., 35 (1998), 384.

[15] JR. Vilella: Metallographic technique for steel, OH: American Society for Metals, Metals Park, Cleveland, (1938), 26.

[16] G. Krauss: Steels: heat treatment and processing principles. Materials Park, OH: ASM International, (1988), 188.

[17] GF. Vander Voort: Metallography: principles and practice McGraw-Hill, New York, (1984), 322.

[18] WI. Halliday: ISI Special Report., 81 (1963), 65.

[19] M.W. Lui, I. LE MAY: Mater. Charact., 4 (1971), 443.

[20] P. Baldinger, G. Posch, and A. Kneisslaas: P. M., 31 (1994), 252.

International Journal of ISSI, Vol. 19(2022), No. 2, pp. 5-11

# The effect of $CaF_2$ on the contact angle of refining powder on the NiCrMoV steel at high temperature using Image Analysis and Statistical Package for the Social Sciences software

**M. Kuwaiti [1], A. R. Alaei *[2], M. Mansouri Hasan Abadi [3], R. Ebrahimi Kahrizsangi [4], H. Ghayour [5]**

*Advanced Materials Research Center, Department of Materials Engineering, Najafabad Branch, Islamic Azad University, Najafabad, Iran.*

## Abstract

Steelmaking refining powders always play an important role in reducing steel inclusions. These types of powders can be used in steel production processes for all types of low-alloy and high-alloy steels. The compositions of these powders are generally $CaO-Al_2O_3-SiO_2$. Adding $CaF_2$ values gives special properties to this type of refining powders. In this study, four types of refining powders with 3 to 6% of $CaF_2$ were melted in induction furnace under high temperature and the surface of NiCrMoV low-alloy steel was impregnated by the molten refining powders. The contact angle between the sample of the molten refining powders and the surface of NiCrMoV steel was determined using Image Analysis (IA) and was analysed using Statistical Package for the Social Sciences (SPSS). The results showed increasing the percentage CaF2 about 6 in refining powder of CaO-Al2O3-SiO2 reduces the contact angle of the molten refining powders on the NiCrMoV steel about 60%.

*Keywords:* NiCrMoV low alloy steel, Refining powder, % $CaF_2$, Contact angle, SPSS analysis.

## 1. Introduction

One of the main industries in the world of economics is the iron and steel industry, which is the raw material for a number of other important industries. After scrap metal is melted in the electric arc furnace (EAF), the molten steel is poured into the ladle and transferred to the next stage of the steelmaking unit by a crane. At this stage, ferroalloys and additives must be added to obtain the final composition of steel. By adding additives and creating special conditions, steel can be refined [1]. These additive materials can be powder and are available in various thermodynamic systems. These materials are melted in the ladle furnace stage and create special conditions for molten steel. The molten refining powders called synthetic slag are always in $CaO-Al2O_3-SiO_2$ multiple systems, and by changing the composition of these multiple systems and adding amounts of $CaF_2$ and MgO, non-metallic $Al_2O_3$ and MgO inclusions can be removed. Molten slag will have a significant effect on the removal of non-metallic inclusions by the mechanisms of flotation of non-metallic inclusion in molten metal- slag contact, separation of inclusion from molten metal to slag and dissolution of inclusion in slag [2]. A change in the chemical composition of slag will change the performance of slag. If $MnO-SiO_2-Al_2O_3$ slag is used, the combined inclusions can be predicted from the partial amounts of dissolved aluminium [3]. High-performance slag has better deoxygenating, desulfurization, inclusions removal capacity and leading to the transfer of inclusions with high amounts of $Al_2O_3$ to the low melting point $CaO-Al_2O_3-SiO_2-MgO$ inclusion system, however high basicity leads to high melting point and low

---

**Corresponding author*
*Email: alaei45alireza@gmail.com*
*Address: Advanced Materials Research Center, Department of Materials Engineering, Najafabad Branch, Islamic Azad University, Najafabad, Iran*
*1. PhD. Candidate*
*2. Assistant Professor*
*3. Assistant Professor*
*4. Professor*
*5. Assistant Professor*

fluidity. These high amounts of slag basicity have no effect on the total oxygen content of the molten steel, but lead to the entry of aluminium and magnesium into the molten iron and increase MgO-$Al_2O_3$ inclusions [4]. Depending on the sampling time-point during the treatment of the ladle furnace, a different spectrum of inclusion-composition is found. If CaO-$Al_2O_3$-$SiO_2$-MgO slag is used under certain conditions, solid alumina (2CaO.2MgO.14$Al_2O_3$ and CaO.2MgO.8$Al_2O_3$) may be formed in the steel. It is well known that non-metallic inclusions found in industrial processes are in most cases heterogeneous which reflects their development during the metallurgical treatment [5]. Improvement of slag performance and reduction of slag basicity is done by adding the amounts of $CaF_2$ in slag, but it should be noted that it will cause environmental pollution and refractory corrosion. Slags based on CaO-$SiO_2$-$CaF_2$ also with high basicity have good deoxygenating, desulfurization and inclusion removal capacity. On the other hand, CaO-$Al_2O_3$ slag creates low oxygenation potential, low melting point, low viscosity and improvement in steel cleanliness. If high levels of $Al_2O_3$ are present in the slag, due to the slag-steel reaction, high amounts of aluminium inter into the steel melt and $Al_2O_3$ and Mg $Al_2O_3$ inclusions make [4]. The physico-chemical properties of metallurgical slags are controlled principally by their structure, basicity, composition, density, viscosity and contact angle between the molten metal and non-metallic solids. These parameters affect the quality of slag in the steelmaking process. The wetting behavior and the adhesion between molten metals and solid ceramics (refining-ladle powder) are important factors which can radically affect the efficiency of any metallurgical process [6]. Examples of situations in which these phenomena can play an important role are; removal of solid inclusions from the melt, either by flotation and filtration; electron beam button melting techniques to assess the cleanness of metals; metal casting and moulding process [4-6]. Practical determination of the wetting and adhesion properties of liquid-solid system at high temperature are generally carried out by either sessile drop or tensiometric techniques. The profile adopted by a liquid drop resting in equilibrium on a flat horizontal surface, is governed by a balance between surface and gravitational forces [6]. Mathematical equations and analysis always help the researcher significantly during the research process. A method called linear regression can be used to match the obtained laboratory data that are prepared in a standard way or obtained from the results of laboratory equipment. In this mathematical method, there are hypotheses that, if the hypothesis is true, there must be a matching of the laboratory sample with the reference sample [7]. To determine the correctness of this hypothesis, it is necessary to use mathematical software. One of these softwares is SPSS, this software can analyse a lot of statistical data on the existing mathematical hypothesis. Using SPSS software with appropriate tools can provide a good analysis to achieve specific parameters in the technical knowledge of steelmaking [8]. In this study, different samples of the slag-making powders with different percentages of $CaF_2$ were prepared and the effect of different amounts of this compound in the composition of slag-making powder in high temperature induction furnace and melting temperature of these powders on the NiCrMoV steel surface using SPSS software was evaluated. IA software was used to measure the contact surface angle of the molten powder on the NiCrMoV steel surface. The process of determining the contact angle of molten slag-making powders containing $CaF_2$ (which can be used as refining-ladle powders) on the surface of NiCrMoV steel using hypotheses and mathematical equations of linear regression and with analysis by SPSS software is a new research that can lead to the improvement of research in the steel industry and especially clean steel production.

## 2. Materials and research methods

Samples of low-alloy steel NiCrMoV were prepared in a cylindrical shape with a diameter of 10 mm and a length of 60 mm (Figure 1). Four samples of refining powder were prepared by combining Table 1 and weigh 15 grams, by 20 ton press in the form of cylindrical samples according to Figure 2. These cylindrical specimens were melted at critical temperature and in high temperature induction furnace graphite crucible (Figure 3). The steel sample according to Figure 1 was immediately immersed vertically and mechanically about 10 mm in the molten powder inside the graphite crucible at a temperature of 1300 °C and in the air atmosphere and went out. This process was repeated 14 times for each sample of molten powder, and using IA, the contact angle of all molten powder samples was measured on the surface of a cylindrical steel sample (Figure 4). The standard angle is determined based on a 100 mg cylindrical specimen on a steel surface and placed at a temperature of 1300 °C in an argon gas environment and when the sample was melted, the standard contact angle of the sample on low-alloy steel NiCrMoV obtained using IA [6]. The figure 5 shows it. The values of contact angle obtained for each sample of molten powder with steel-shaped sample and also steel submersible rod in molten powder samples were evaluated using SPSS software.

Table 1. Chemical compositions of refining powders A, B, C and D
(In terms of weight percentage)

| Refining powders | %$Al_2O_3$ | %$SiO_2$ | %(CaO+MgO) | %$CaF_2$ |
|---|---|---|---|---|
| A | 19.11 | 7.77 | 50.06 | 3.08 |
| B | 18.72 | 7.92 | 49.95 | 4.04 |
| C | 18.88 | 7.97 | 49.45 | 4.98 |
| D | 18.84 | 7.66 | 49.55 | 6.01 |

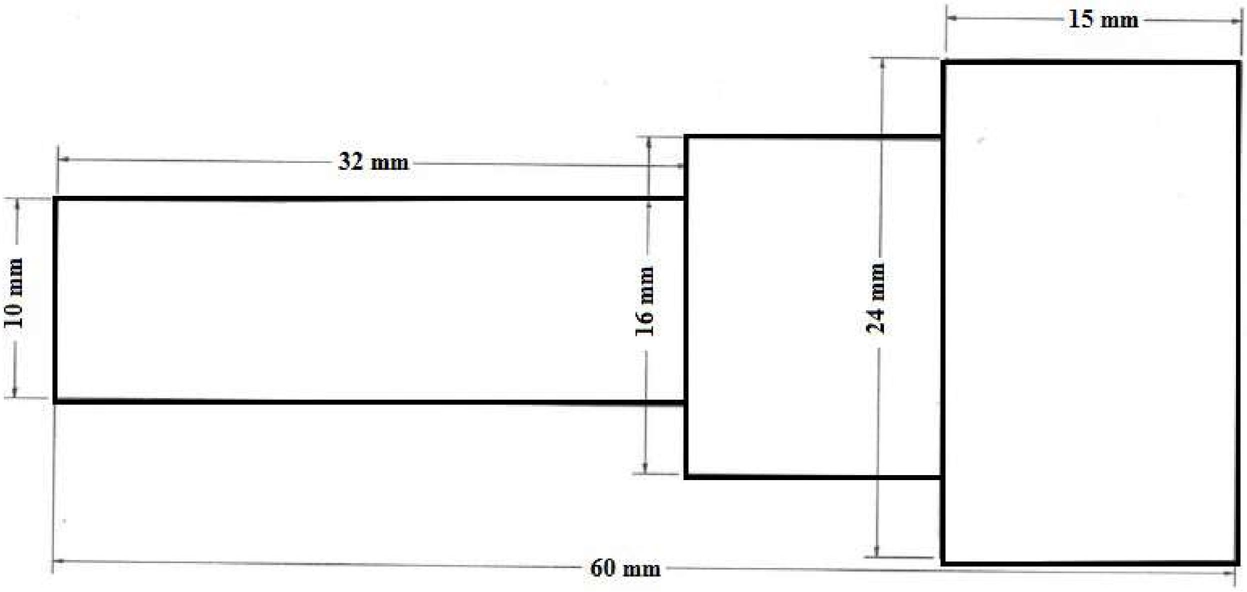

Fig. 1. Sample of low-alloy NiCrMoV steel prepared for submerging in the molten refining powder.

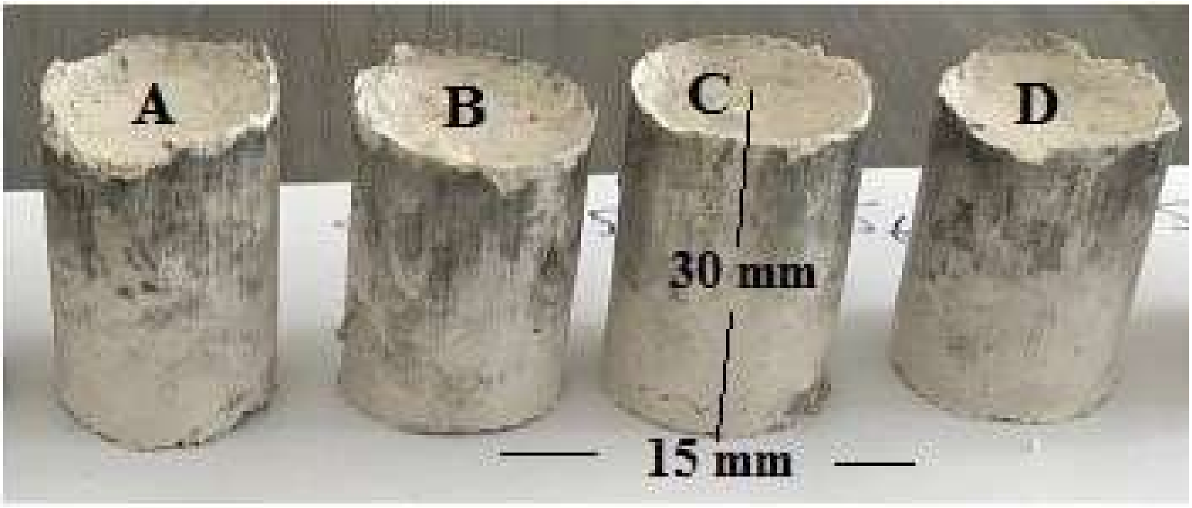

Fig. 2. Cylindrical specimens of 15 g of the pressed refining powders A, B, C and D.

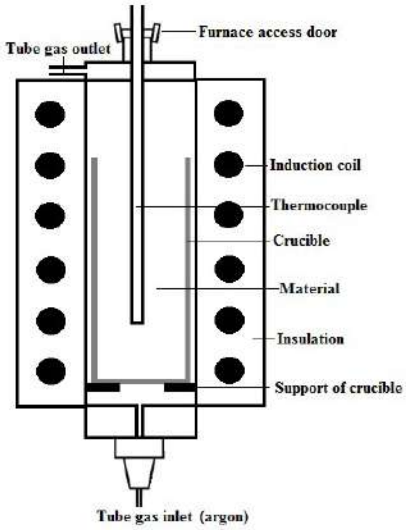

Fig. 3. High temperature induction furnace for melting 15 g and 100 mg refining powder samples.

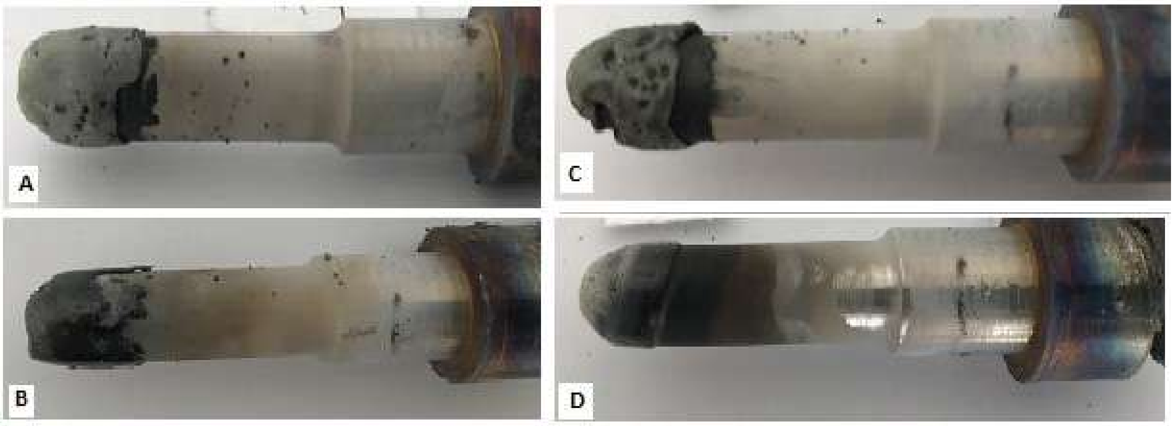

Fig. 4. Samples obtained from submerged steel cylindrical rods in the molten refining powders A, B, C and D to determination of their contact angle.

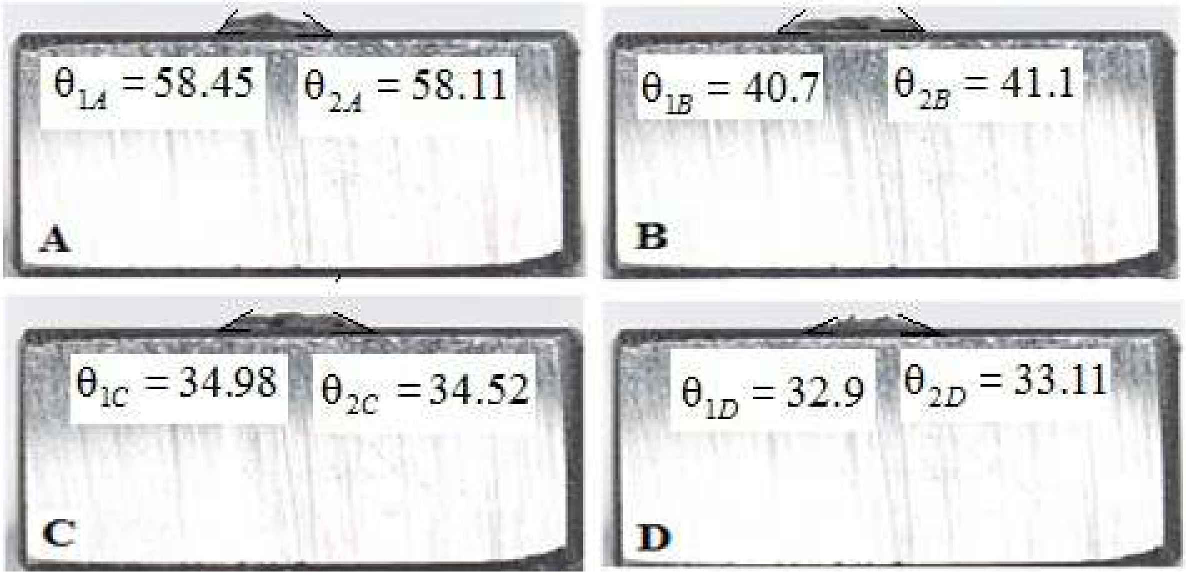

Fig. 5. The molten standard powder samples A, B, C and D on the NiCrMoV steel surface at 1300 ° C.

## 3. Results and Discussion

### 3.1. Determining the contact angle of the molten refining powders on the NiCrMoV steel surface by IA software

Four angles of the molten refining powder on the submersible rod surface were measured using IA, and then the average of these four angles for each sample (A to D) was recorded in Table 2. To increase the measurement accuracy, this process was repeated 14 times for each sample. Table 2 shows these values. The results of Table 2 can be used for SPSS analysis. Each sample was tested 14 times to obtain statistical results with high accuracy. According to Figure 5 and Table 3, the contact angles of the standard sample on the steel surface are determined. Each molten powder sample on the steel surface has two contact angles; their average was calculated and recorded in Table 3. Each sample was tested 4 times to obtain statistical results with high accuracy. Tables 2 and 3 show that the standard and measured contact angle decreases with increasing amount of $CaF_2$. This analysis is suitable for the chemical composition of the tested samples because the contact angle is lower in the chemical composition that has a high amount of CaO+MgO and the powder does not have good fluidity, but with the increase in the amount of $CaF_2$ in the chemical composition of the samples, the fluidity also increases [6]. This can have a direct effect on the contact angle of the samples.

### 3.2. Analysis of contact angle of refining powders with different percentages of $CaF_2$ by SPSS

Analysis of output data from SPSS software is done in two ways. First, it is necessary to determine the normal distribution diagram for each of the output data from the obtained angles, and after the normal distribution for four samples was determined using t-test, the contact angle values of the molten powders with the steel cylinder sample can be determined. Equation 1 shows the value of the t test [7].

$$t = \frac{\bar{x} \_ \mu_0}{S / \sqrt{n}} \qquad \text{Eq.(1)}$$

In equation 1, $\bar{x}$ is the mean value of the data (the standard value), S is the standard deviation value, and n is the number of data.

Table 2. The average angles measured by IA software for four refining samples A, B, C and D with different percentages of $CaF_2$.

| Sample | Angle A | Angle B | Angle C | Angle D |
|---|---|---|---|---|
| 1 | 72.66 | 38.34 | 32 | 34.56 |
| 2 | 72.75 | 39.28 | 33.94 | 32.96 |
| 3 | 47.89 | 38.99 | 34.80 | 30.37 |
| 4 | 53.42 | 36.98 | 32.80 | 34.08 |
| 5 | 72.89 | 33.30 | 35.36 | 29.74 |
| 6 | 62.48 | 34.99 | 35.32 | 28.82 |
| 7 | 46.45 | 39.66 | 31.46 | 27.40 |
| 8 | 54.24 | 37.26 | 33.17 | 33.11 |
| 9 | 37.23 | 38.87 | 34.69 | 33.60 |
| 10 | 44.70 | 38.04 | 33.25 | 31.82 |
| 11 | 41.38 | 39.28 | 34.52 | 38.66 |
| 12 | 68.19 | 35.98 | 35.23 | 35.07 |
| 13 | 43.91 | 36.46 | 33.35 | 24.44 |
| 14 | 45.23 | 38.95 | 34.52 | 25.52 |

Table 3. The average angles measured by IA software for four samples of the molten refining powders A, B, C and D with different percentages of $CaF_2$ on the surface of NiCrMoV steel at 1300 ° C.

| Angle A | Angle B | Angle C | Angle D |
|---|---|---|---|
| 58.28 | 40.90 | 34.75 | 33.00 |

### 3.2.1. Normal distribution diagram

The value of the normal distribution function f (x) is obtained from equation 2 [7].

$$f(x) = \frac{1}{S\sqrt{2\pi}} \times \exp(-0.5 \times (\frac{x - \mu_0}{S})^2) \quad \text{Eq. (2)}$$

Figure 6 shows the normal distribution diagram of four samples A to D. As shown in figure 6, all of these graphs have a normal state with a concordance coefficient higher than 95%, so the t-test can be used for them. Samples A to D have the normal distribution diagram (R2>0.95), but they were drawn with different dispersion; the reason can be in the chemical composition of these samples. The distribution diagram of A to D has shifted down and to the left, while the chemical composition of these four samples also showed that amount of $CaF_2$ are also increasing, so it seems that the increase of amount $CaF_2$ can reduce the value of f (x) in the equation 2.

### 3.2.2. Analysis of t-test using SPSS

Table 4 shows the analysis of data extracted from SPSS software. Data analysis by SPSS software shows that the values of the angles of the samples from A to D are 55, 38, 34 and 32, respectively. The t-test according to the standard table with relative error rate of 0.05% and for 14 samples with value of 2.16 determines that this value is greater than equation 1 for all four samples of refining powder, so the hypothesis of equation 3 is correct [7,8].

$$H_0 : \overline{X} = C \qquad H_1 : \overline{X} \neq C \quad \text{Eq. (3)}$$

Therefore, t-test completely indicates this data and the angles obtained in table 4 are in perfect match with the contact angle of refining powders on the NiCrMoV steel.

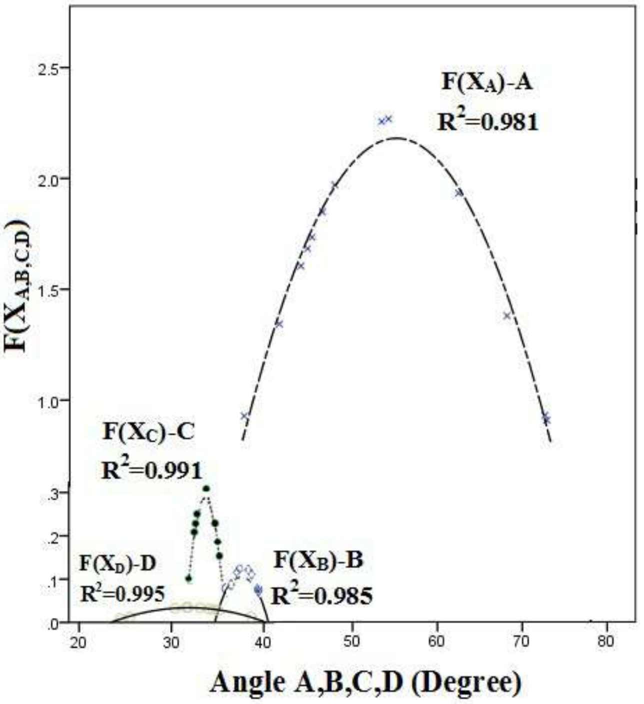

Fig. 6. Normal distribution functions for four powder samples based on the angles obtained.

Table 4. Evaluation of the angle obtained using SPSS software.

| | One-Sample Test | | | | |
|---|---|---|---|---|---|
| | df | Sig. (2-tailed) | Mean Difference | 95% Confidence Interval of the Difference | |
| | | | | Lower | Upper |
| Angle A | 13 | .000 | 54.963857 | 47.15394 | 62.77377 |
| Angle B | 13 | .000 | 37.602357 | 36.51941 | 38.68530 |
| Angle C | 13 | .000 | 33.890714 | 33.17225 | 34.60918 |
| Angle D | 13 | .000 | 32.015286 | 29.52649 | 34.50408 |

### 3.3. The effect of contact angle of the refining powder containing $CaF_2$ on the NiCrMoV steel

The angles obtained between the molten powder samples and the surface of the steel are reduced from A to D, and it is indicated the proper contact angle (wettability) of sample D on the NiCrMoV steel. Table1 shows, by increasing the $CaF_2$ values, the more suitable adhesion or wettability angle can be achieved on the NiCrMoV steel. Figure 7 shows the reduction of the contact angle by decreasing the percentage of $CaF_2$ in the refining powder sample.

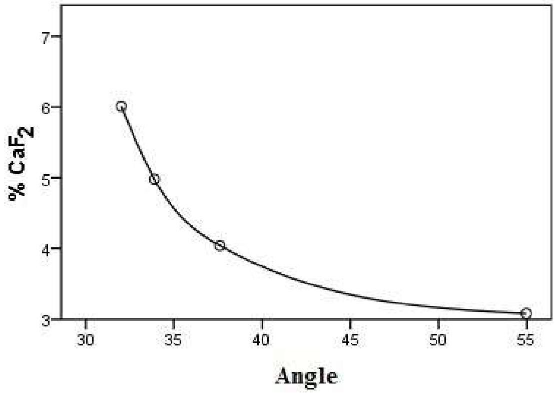

Fig. 7. Effect of percentage of $CaF_2$ refining powder on the contact angle (wettability) of NiCrMoV steel.

## 4. Conclusion

The following results were obtained from this study:

- The standardization of the contact angle (wettability) of the molten refining powders on the NiCrMoV steel surface can be done with high accuracy and 14-times repetitions.
- Increasing amount of $CaF_2$ to more than 5% does not have a significant effect on the contact angle.
- The design of refining powder can be done with proper analysis and the contact angle (wettability) using SPSS and a t-test with the lowest percentage of error and very suitable matching.

## Reference

[1] M. Fanti and G. Rotunno, " Production Scheduling in a Steelmaking and Continuous Casting Plant: a Case Study ", IEEE International Conference on Robotics and Automation, 2013, pp. 3580-3585.
[2] B. Reis, W. Bielefeldt and A. Vilela, " Absorption of non-metallic inclusions by steelmaking slags-a review", Journal of Materials Research and Technology, 3(2), 2014, pp. 179-185.
[3] S. Kobayashi, "Thermodynamic Fundamentals for Alumina-content Control of Oxide Inclusions in Mn-Si Deoidation of Molten Steel", ISIJ International, Vol. 39, No. 7, 1999, pp. 664-670.
[4] Q. Wang, L. Wang and K. Chou, "Effect of Al2O3 Content in Top Slag on Cleanness of Stainless Steel Fe-13Cr", The Minerals, Metals & Materials Society, 2016, pp. 155-163.
[5] P. Scheller and Q. Shu, "Inclusion Development in Steel During Ladle Metallurgical Treatment –A Process Simulation Model-Part: Industrial Validation", Steel Research int., 85, No. 8, 2014, pp. 1310-1316.
[6] D. Springorum, " Slag Atlas", The committee on Metallurgical Fundamentals of the German Iron and Steel Insititute (VDEh), 1995.
[7] P. Goos and D. Meintrup, " Statistics with JMP: Hypothesis Tests, ANOVA and Regression", Wiley, 2016.
[8] L. S. Meyers, G. C. Gamst and A. J. Guarino, " Performing Data Analysis Using IBM SPSS", Wiley, 2013.

# Phenomenological Arrhenius type constitutive equation for a 304 stainless steel during hot deformation

**J. Rasti *[1], A. Najafizadeh [2], S. Jafari [3], B. Khodabandeloo [4]**

[1, 3, 4] *Department of Mechanical Engineering, Qom University of Technology (QUT), Qom, Iran*
[2] *Department of Materials Engineering, Isfahan University of Technology, Isfahan, Iran*

## Abstract

The present study aimed to present a phenomenological and empirically-based constitutive model to predict the flow behavior of 304 stainless steel. Hot compression tests were performed at temperatures of 950-1100 °C and strain rates of 0.005-0.5 $s^{-1}$ up to the strain of 1. To demonstrate flow curves, three regimes were considered including the linear trend up to yield stress, the work hardening-recovery dominant region based on Estrin and Mecking model from the yield point up to the saturation stress, and the recovery-recrystallization zone from the critical stress extends toward the steady state stress. The Avrami-type equation was supposed for the kinetics of recrystallization and validated by the evolved microstructures at strain 1. Eventually, the six equations that describe the model via strain, strain rate, and temperature were presented. They have included the Arrhenius type equation for the yield, saturation, and steady-state stresses, in addition to the critical strains and the inflection strains together with the relationship for the exponent of Avrami-type recrystallization kinetics formula, all as functions of Zener-Hollomon parameter. Comparing the flow curves predicted by the model with the experimental results showed satisfactory coincidence, confirming that the proposed model can give an almost accurate estimation of the flow stresses of 304 stainless steel at different conditions.

*Keywords:* Hot deformation; 304 stainless steel; Constitutive equation; Dynamic recrystallization; Arrhenius equation.

## 1. Introduction

It has been widely confirmed that thermo-mechanical processing is an effective technology to control microstructure and obtain excellent mechanical properties in stainless steels by optimizing the process parameters, such as a measure of strain, temperature, and strain rate. A vast amount of information regarding the relationship between various factors encountered in the hot forming of materials can be expressed in the form of constitutive equations. Constitutive equations can be derived from a macroscopic or microscopic view. Phenomenological equations are derived based on the macroscopic view. This type of modeling establishes the correlation between the measurable parameters such as flow stress, strain, strain rate, and temperature, in the framework of mathematical functions [1, 2].

The most common type of stainless steel in use is grade 304. This grade offers impressive strength, as well as incredible corrosion resistance, lending it to applications in which contact with food, chemicals, or freshwater must be tolerated. Cognitive Market Research has published a market volume of 304 Stainless Steel about 30% of global production of stainless steel (~50 million tons).

Different constitutive equations have been proposed so far by various researchers. Some of these relationships can be seen in Table 1. Since these equations correlate the flow stress with temperature, strain, and strain rate, finding the proper equation and then relevant parameters is a tedious, difficult, and time-consuming task.

---

**Corresponding author*
*Email: rasti@qut.ac.ir*
*Address: Dep. of Mechanical Engineering, Qom University of Technology (QUT), Qom, Zip:1519-37195 Iran*
*1. Assistant Professor*
*2. Professor*
*3. M.Sc. Student*
*4. M.Sc. Student*

Table 1. Different constitutive equations for the modeling of flow curves.

| | |
|---|---|
| Field Backofen (FB) [1] | $\sigma = K\varepsilon^n\dot{\varepsilon}^m \qquad K = f(T,\dot{\varepsilon}), n = g(T,\dot{\varepsilon}), m = h(T)$ |
| Modified FB [2,3] | $\sigma = K\varepsilon^n\dot{\varepsilon}^m \exp(\mathrm{b}T + \mathrm{s}\varepsilon) \quad n = f(T,\dot{\varepsilon}), m = g(T), K, b, s = \text{const.}$ |
| Johnson Cook (JC) [4] | $\sigma = (A + B\varepsilon^n)\left[1 + C\ln\left(\frac{\dot{\varepsilon}}{\dot{\varepsilon_0}}\right)\right]\left[1 - \left(\frac{T-T_r}{T_m-T_r}\right)^m\right]$, $A, B, n, C, \dot{\varepsilon_0}, T_r, T_m$=const. |
| Modified JC [5] | $\sigma = (A_0 + A_1\varepsilon + A_2\varepsilon^2)\left(1 + D_1\left(\frac{\dot{\varepsilon}}{\dot{\varepsilon_0}}\right)\right)\exp\left[\left(\lambda_1 + \lambda_2\ln\left(\frac{\dot{\varepsilon}}{\dot{\varepsilon_0}}\right)\right)(T - T_r)\right]$<br>$A_0, A_1, A_2, D_1, \dot{\varepsilon_0}, \lambda_1, \lambda_2, T_r = \text{const.}$ |
| JC with grain size effect [6] | $\sigma = (A + B\varepsilon^n)\left[1 + \lambda\left(\frac{d}{d_0}\right)\right]\left[1 + C_1\ln\left(\frac{\dot{\varepsilon}}{\dot{\varepsilon_0}}\right)\right]\exp\left[\left(f\left(\frac{d}{d_0}\right) + C_1\ln\left(\frac{\dot{\varepsilon}}{\dot{\varepsilon_0}}\right)\right)(T - T_r)\right]$ |
| Arrhenius (Arr) [7-10] | $Z = \dot{\varepsilon}\exp(Q_{\text{def}}/RT) = \begin{cases} B\,{\sigma_{\mathrm{P}}}^{n'} \\ A'\exp(\beta\sigma_{\mathrm{P}}) \\ A\left(\sinh(\alpha\sigma_{\mathrm{P}})\right)^n \end{cases}$<br>$Q_{\text{def}}, B, n', A', \beta, A, \alpha, n = \text{const.}\ or\ f(\varepsilon), R = \text{gas const.}$ |
| Zerilli Armstrong (ZA) [11] | $\sigma = c_0 + B_0\varepsilon^n\exp(-\beta_0 T + \beta_1 \mathrm{T}\ln\dot{\varepsilon})$, n=0.5 in original work |
| Modified ZA [12] | $\sigma = (A_0 + A_1\varepsilon + A_2\varepsilon^2 + A_3\varepsilon^3)\exp\left[-(B_0 + B_1\varepsilon + B_2\varepsilon^2 + B_3\varepsilon^3)(T - T_r) + (C_0 + C_1(T - T_r) + C_2(T - T_r)^2 + C_3(T - T_r)^3)\ln\left(\frac{\dot{\varepsilon}}{\dot{\varepsilon_0}}\right)\right]$ |
| Hansel Spittle (HS) [13] | $\sigma = A\exp(m_1T)\varepsilon^{m_2}\dot{\varepsilon}^{m_3}\exp(m_4/\varepsilon)(1 + \varepsilon)^{m_5T}\exp(m_6\varepsilon)\dot{\varepsilon}^{m_7T}T^{m_8}$ |
| Voyiadjis Abed [14] | $\sigma = (c_1 + c_2\varepsilon^{c_3}) + c_4\left[1 - \left[-c_5T\ln\left(\frac{\dot{\varepsilon}}{\dot{\varepsilon_0}}\right)\right]^{1/q_1}\right]^{1/q_2} + c_6\varepsilon^{c_7}\left[1 - \left[-c_5T\ln\left(\frac{\dot{\varepsilon}}{\dot{\varepsilon_0}}\right)\right]^{1/q_1}\right]^{1/q_2}$ |

Among these equations, the sine hyperbolic Arrhenius type equation was used extensively for the modeling of the characteristic stresses as a function of the Zener–Hollomon parameter (*Z*) [7-10, 15, 16].

$$Z = \dot{\varepsilon}\exp(Q_{\text{def}}/RT) = A\left(\sinh(\alpha\sigma)\right)^n \text{ or} \qquad \text{Eq. (1)}$$

$$\dot{\varepsilon} = A\left(\sinh(\alpha\sigma)\right)^n\exp(-Q_{\text{def}}/RT)$$

Where $\dot{\varepsilon}$ is the strain rate ($s^{-1}$), A, $\alpha$, and $n$ are constants independent of temperature, $\sigma$ is the characteristic stress (MPa), $Q_{def}$ is the hot deformation activation energy (J $mol^{-1}$), R is the gas constant and T is the absolute temperature (K) of deformation. By mathematical manipulation, the flow stress may be rewritten as a function of *Z* as follows:

$$\sigma = \frac{1}{\alpha}\left\{\left(\frac{Z}{A}\right)^{1/n} + \left[\left(\frac{Z}{A}\right)^{2/n} + 1\right]^{1/2}\right\} \qquad \text{Eq. (2)}$$

Fig. 1a shows schematically the stress-strain curve obtained during the deformation of materials exhibiting the dynamic recrystallization process (DRX). Characteristic stresses, namely the critical stress ($\sigma_C$) for the initiation of DRX, the peak stress ($\sigma_P$), the saturation stress ($\sigma_S$), and the steady state stress ($\sigma_{SS}$) can be determined from the strain hardening rate ($\theta = d\sigma/d\varepsilon$) vs flow stress ($\sigma$) plot (Fig. 1b). The critical stress ($\sigma_C$) and consequently the critical strain for the onset of the DRX can be identified using the Poliak and Jonas method [17-19] modified by Najafizadeh and Jonas [20] as an inflection point of $\theta$-$\sigma$ plot.

After determining the above characteristic stresses for the different deformation conditions, a constitutive equation such as sine hyperbolic Eqs. (1) or (2) may be used to model them. The procedure for finding proper parameters for this equation is described below.

The graph up to the yield strength($\sigma_0$) has almost a linear trend, afterward, the stress-strain curve can be distinguished by two different domains: 1- the extent from $\sigma_0$ to $\sigma_C$ which continues to the saturation stress $\sigma_S$, where called the work hardening and dynamic recovery (WH) zone, and 2- the extent begins at $\sigma_C$ and continues toward the $\sigma_P$ and finally $\sigma_{SS}$, named as dynamically recrystallized zone (DRX).

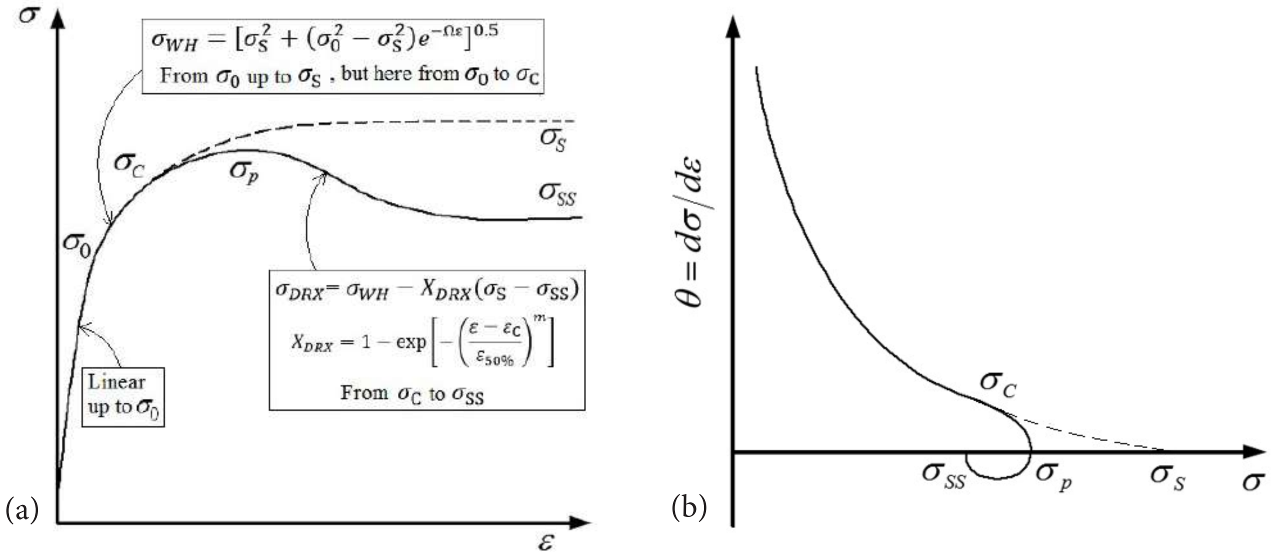

Fig. 1. (a) The schematic flow curve showing the characteristic stresses including the critical stress ($\sigma_C$), the peak stress ($\sigma_P$), the saturation stress ($\sigma_S$), and the steady state stress ($\sigma_{SS}$), and (b) the procedure of determining them by drawing the strain hardening rate vs. stress.

### 1.1. Modeling the work hardening and dynamic recovery (WH) zone

Generally, the Taylor relationship is accepted between the flow stress and dislocation density as $= \sigma_0 + M\alpha Gb\sqrt{\rho}$ . The rate of dislocation generated by the plastic work and its rate of removal by dynamic recovery determines the total work hardening:

$$\frac{d\rho}{dt} = \left(\frac{d\rho}{dt}\right)_{\text{Plastic work}} + \left(\frac{d\rho}{dt}\right)_{\text{Recovery}} \qquad \text{Eq. (3)}$$

By increasing the dislocation density, the driving force for dynamic recovery is provided. Dynamic recovery reduces that by annihilating positive and negative ones and rearranging them through dislocation climb and cross slip to create sub- or cell-structure (low angle grain boundaries). In austenitic stainless steel due to the low stacking fault energy (about 21 erg/cm$^2$), this process is not rapid, and hence, with more plastic work, dislocation density severely raises and their distribution is also heterogeneous, which causes the dense cell structure with almost small mean size of $\overline{l}$ (dislocation-free distance) interior grains [21].

Two models for change in dislocation density with strain have been presented. Kock and Mecking (KM) have expressed the following dislocation evolution model [22, 23]:

$$\frac{d\rho}{d\varepsilon} = k_1\sqrt{\rho} - k_2\rho \qquad \text{Eq. (4)}$$

Where $k_1\sqrt{\rho}$ is the storage term of mobile dislocations that are locked after distance $\overline{l}$, independent of the temperature, and the second term, $k_2\rho$ , relates to the dynamic recovery, which is a function of temperature and strain rates.

Estrin and Mecking (EM) supposed that the dislocation free distance is constant and hence the dislocation accumulation rate is fixed and the equation is rewritten as follows [24].

$$\frac{d\rho}{d\varepsilon} = k - k_2\rho \qquad \text{Eq. (5)}$$

Where $k=(bl)^{-1}$. In this model the stress-strain relationship would be as follow on a macroscopic scale;

$$\frac{\sigma^2 - \sigma_S^2}{\sigma_0^2 - \sigma_S^2} = \exp\left(-\frac{\varepsilon}{\varepsilon_C}\right) \qquad \text{Eq. (6)}$$

Where $\varepsilon_C$ is a specific strain dependent on the material and $\sigma_S$ is the saturation stress. Robert [25] also reported that at the strains above 0.05, $\theta=d\sigma/d\varepsilon$ has a linear relationship with $1/\sigma$, so the following relationship is established.

$$\theta = \frac{A}{\sigma} - B\sigma \qquad \text{Eq. (7)}$$

In this case, the dislocation density changes according to the EM equation:

$$\frac{d\rho}{d\varepsilon} = U - \Omega\rho \ \rightarrow \ \rho = \rho_0 e^{-\Omega\varepsilon} + (U/\Omega)(1 - e^{-\Omega\varepsilon}) \qquad \text{Eq. (8)}$$

And the WH flow stress equation can be expressed below which is the same as Eq. (6):

$$\sigma_{WH} = [\sigma_S^2 + (\sigma_0^2 - \sigma_S^2)e^{-\Omega\varepsilon}]^{0.5} \qquad \text{Eq. (9)}$$

### 1.2. Modeling the DRX region

The flow stress just after the onset of DRX regarding the softening effect of recrystallization phenomena against the work hardening regime with the following assumption:

$$X_{DRX}(\varepsilon) = \frac{\sigma_{WH}(\varepsilon)-\sigma_{DRX}(\varepsilon)}{\sigma_{S}-\sigma_{SS}}, \qquad \text{Eq. (10)}$$

$$\sigma_{DRX}= \sigma_{WH} - X_{DRX}(\sigma_{S} - \sigma_{SS})$$

Therefore, by knowing the recrystallized fraction at different strains ($X_{DRX}$), the flow curve beyond the recrystallization onset can be extracted. The recrystallized fraction can be also modeled with the modified Avrami-type equation as follows [26],

$$X_{DRX} = 1 - \exp\left[-\left(\frac{\varepsilon - \varepsilon_{C}}{\varepsilon_{50\%}}\right)^{m}\right] \qquad \text{Eq. (11)}$$

Where $\varepsilon_C$ is the strain for the onset of dynamic recrystallization and $\varepsilon_{50\%}$ is the strain equivalent to the 50% DRX progress (can be regarded as $\varepsilon^*$, the strain at maximum softening rate which is a function of temperature and strain rate [27]) and m is the constant showing the transformation kinetics.

Regarding the literature review, almost articles considering the constitutive equation of 304 stainless steel were based merely on the mathematical manipulation of flow curves via the curve fitting method and did not include phenomenological and microstructural insight. Consequently, this article involved in determining the expressions for the yield stress ($\sigma_0$), the saturation stress ($\sigma_S$), and the steady state stress ($\sigma_{SS}$) as well as the equations for the critical ($\varepsilon_C$) and inflection strains ($\varepsilon_i$) and the exponent of Avrami-type kinetics for the recrystallization (m), the six parameters that the proposed phenomenological model is based on those relations via strain, strain rate, and temperature.

## 2. Material and Methods

AISI 304 stainless steel with a chemical composition (wt.%) of Fe-0.033% C-9.07% Ni-18.3% Cr-1.97% Mn-0.342% Si-0.573% Mo-0.075% Ti-0.023% P was used in this study. Cylindrical samples 15 mm in height and 10 mm in diameter were machined from the hot rolled bars. The initial grain size of the hot rolled bar was 6 µm, where after annealing at 1100 °C for 30 min, the homogenized microstructure with an average grain size of 40 µm was attained before deformation based on the Heyn intercept method (ASTM E-112). Hot compression tests were carried out in order to study the recrystallization behavior during deformation. Mica plates and BN powder were used for lubricating. The samples were heated by four SiC elements set in the furnace of compression apparatus to the deformation temperatures of 950, 1000, 1050, and 1100 °C and held for 2 min for temperature homogenization. Deformation was carried out at strain rates of 0.005, 0.05, and 0.5 $s^{-1}$ to the true strain of 1, and samples were then quenched immediately (<1 s) after deformation to investigate the DRX microstructures. Samples were then cut along the compression axis and after grinding and polishing, they were etched electrochemically in a 65% nitric acid solution. In order to minimize the effect of friction on the stress-strain curves and correct them, the method of Ebrahimi and Najafizadeh was used [28].

## 3. Results and Discussion

### 3.1. Characteristic stresses evaluation

Fig. 2 shows the stress-strain curves obtained from the hot compression tests under various deformation conditions. All the samples exhibited typical DRX flow curves with a single peak stress followed by a gradual fall towards a steady state stress. At the highest strain rate tested (0.5 $s^{-1}$), a clear delay for the start of DRX can be observed, so the steady state condition is not achieved.

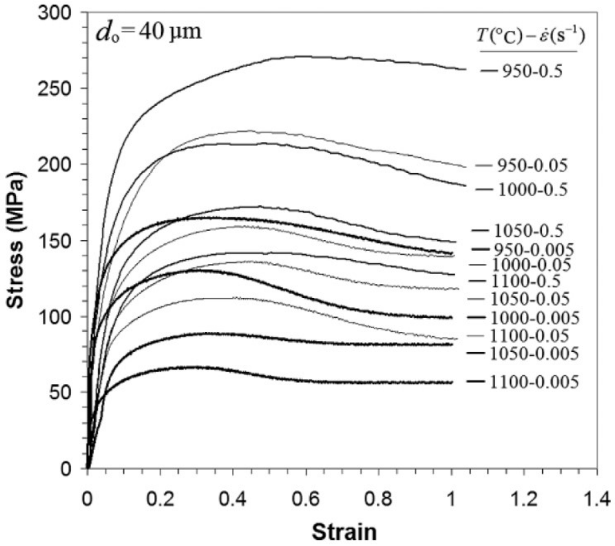

Fig. 2. Stress–strain curves at different deformation temperatures and strain rates.

Eqs. (1) and (2) can be employed for any characteristic stresses including the yield stress ($\sigma_0$), the peak stress ($\sigma_P$), the saturation stress ($\sigma_S$), and the steady state stress ($\sigma_{SS}$). Four constant parameters including A, $\alpha$, n, and Q should be determined for any of these stresses. The procedure will be described as follows for the peak stress, similarly the same trend must be straightforwardly accomplished for the other characteristic stresses aforementioned.

First, Eq. (1) should be rewritten as below:

$$\ln(\dot{\varepsilon}) = \ln A + n\ln[\sinh(\alpha\sigma_P)] - Q_{def}/RT \quad \text{Eq. (12)}$$

With the assumption of $\alpha$=0.01, the constant $n$ can be determined by the relationship between ln ($\dot{\varepsilon}$) and ln [sinh($\alpha\sigma_P$ )] as follows:

$$n = \left.\frac{\partial \ln(\dot{\varepsilon})}{\partial \ln[\sinh(\alpha\sigma_P)]}\right|_{T=\text{const.}} \quad \text{Eq. (13)}$$

By assuming that $\alpha\sigma_P$>1.2 the $\sinh(\alpha\sigma_P) \cong \frac{1}{2}\exp(\alpha\sigma_P)$, and therefore the Eq. 12 can be expressed as below,

$$\ln(\dot{\varepsilon}) = \ln A - n\ln(2) + n\alpha\,\sigma_P - Q_{def}/RT \quad \text{Eq. (14)}$$

So, the coefficient $n\alpha$ may be determined by the relationship between ln ($\dot{\varepsilon}$) and $\sigma_P$ as follows:

$$n\alpha = \left.\frac{\partial \ln(\dot{\varepsilon})}{\partial\,\sigma_P}\right|_{T=\text{const.}} \quad \text{Eq. (15)}$$

Hence, by knowing $n$, the parameter $\alpha$ can be obtained and again employed for determining the constant $n$ at Eq. (4) and this return cycle continues to finally the closely same values for $\alpha$ and $n$ acquired with variation less than 10%. After then, with knowing $n$ and $\alpha$ the activation energy of deformation can be determined by the relationship between ln[sinh($\alpha\sigma_P$)] and $1/T$ as follows:

$$Q_{def} = nR\left.\frac{\partial \ln[\sinh(\alpha\sigma_P)]}{\partial\,(1/T)}\right|_{\dot{\varepsilon}=\text{const.}} \quad \text{Eq. (16)}$$

Eventually, the parameter A can be attained from the y-intercept value of straight-line regression of data ln($Z$) as the y-axis vs. ln [sinh($\alpha\sigma_P$ )] as the x-axis.

Fig. 3 shows the above trends for the peak stress. The following constants were accordingly obtained: A=1.542×$10^{19}$ $s^{-1}$, n=4.56, α=0.0116, and $Q_{def}$= 546.7 kJ/mol.

Similarly, the same trends were employed for the other characteristic stresses. The relevant constants were then obtained as can be seen in Table 2.

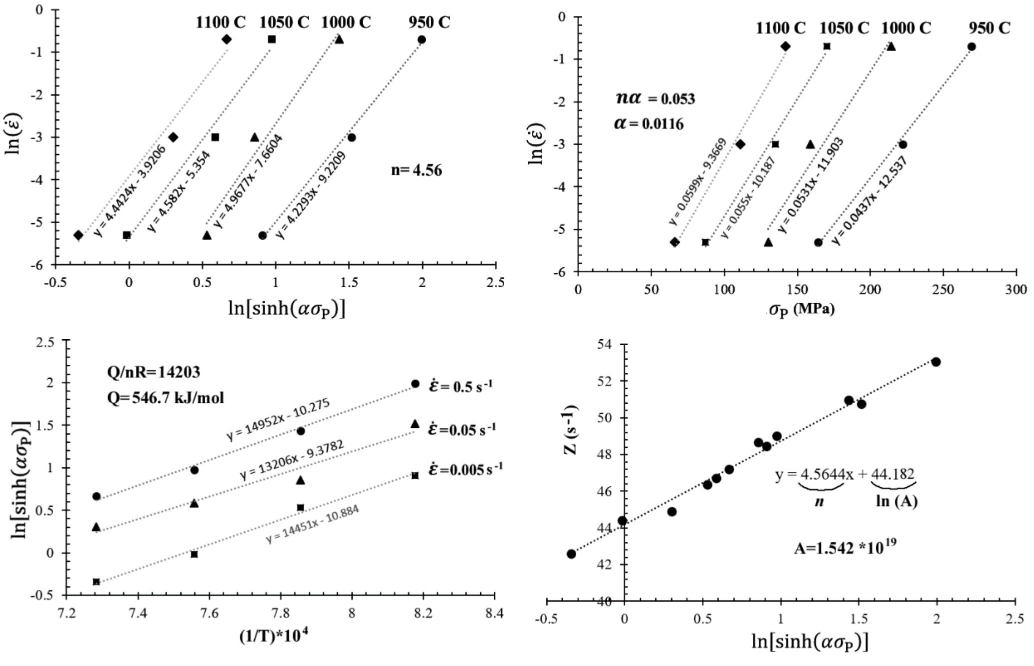

Fig. 3. Determination procedure for the constants of Eq. (1) for the peak stress.

Table 2. The constants of Eq. (1) for the different characteristic stresses.

| Stress | A ($s^{-1}$) | $n$ | α ($MPa^{-1}$) | $Q_{def}$ (kJ/mol) |
|---|---|---|---|---|
| Yield stress ($\sigma_0$) | 3×$10^{21}$ | 6.68 | 0.01 | 519 |
| Peak stress ($\sigma_P$) | 1.542×$10^{19}$ | 4.56 | 0.0116 | 546.7 |
| Saturation stress ($\sigma_S$) | 1.15×$10^{19}$ | 4.45 | 0.0099 | 544 |
| Steady state stress ($\sigma_{SS}$) | 1.6×$10^{19}$ | 6.15 | 0.0052 | 484 |

Mohebbi et al. [29] proposed the sine hyperbolic Arrhenius equation for the peak stresses of flow curves of an Nb-Ti micro-alloyed steel considering the self-diffusion activation energy as a dominant mechanism. They proposed a constant value of n=5 based on Cabera et al. work [30] where the deformation process is controlled by the mechanism of dislocation glide and climb. Indeed, in the Nb, Nb-B, and Cu-Nb-B steels, the amount of $Q_{def}$ is very close to its self-diffusion activation energy in the austenite phase, $Q_{SD}$, but in HSLA steels and austenitic stainless steels, the $Q_{def}$ value is greater than $Q_{SD}$, due to the impact influence of the precipitations and impurities on the accumulation of dislocations and microstructural changes, even at a very small extent. For example, If instead of $\sigma_p$ in the above relations $\sigma_{SS}$ is used, less activation energy is obtained, Q ($\sigma_{SS}$) < Q ($\sigma_p$) [22]. Long et al. used another approach for modeling of flow curves of a magnesium alloy considering the parameters A, $\alpha$, n, and Q as a function of temperature and strain rate [31].

## 3.2. Characteristic strain evaluation

The characteristic strains namely critical strain ($\varepsilon_C$) for the initiation of DRX, the strain corresponding to the peak stress (peak strain = $\varepsilon_P$), the strain equivalent to the inflection point on the stress-strain curve (inflection strain = $\varepsilon_i$), and the strain corresponding to the onset of steady-state flow (steady state strain = $\varepsilon_{SS}$), were also determined in this study (Fig. 4). The critical strain was identified using the Poliak and Jonas method [18] modified by Najafizadeh and Jonas [20]. In their approach, the initiation of DRX is believed to be the inflection point in the strain hardening rate ($\theta=d\sigma/d\varepsilon$) vs flow stress ($\sigma$) plot. The values of $\varepsilon_i$ were also identified from the inflection points on the stress-strain curves located between the peak and steady-state stresses. The relation of the critical strain to the peak strain was $\varepsilon_C/\varepsilon_P \cong 0.58$ which is in good accordance with the results of the previous work on 304 steel with an initial grain size of 35 µm ($\varepsilon_C/\varepsilon_P \cong 0.6$) [32] but somewhat lower than that reported by Kim and Yoo [27] for material with an initial grain size of 100 µm ($\varepsilon_C/\varepsilon_P \cong 0.73$).

In all following relationships, the parameter Z was regarded as $Z = \dot{\varepsilon}\exp\left(\frac{546700}{RT}\right)$.

$$\begin{aligned} &\varepsilon_p = 16.9 \times 10^{-3} Z^{0.0676} \\ &\varepsilon_{crit} = 2.6 \times 10^{-3} Z^{0.094} \cong 0.58\,\varepsilon_p \\ &\varepsilon_i = 7.3 \times 10^{-3} Z^{0.1} \\ &\varepsilon_{SS} = 3.9 \times 10^{-3} Z^{0.118} \end{aligned} \quad \text{Eq. (17)}$$

## 3.3. Modeling the stress-strain curve

In this study, it is supposed that the stress against strain linearly goes up until to yield stress $\sigma_0$ and the equivalent strain would be about 0.01~0.03. Beyond this region, from $\sigma_0$ to $\sigma_C$, the work-hardening region ($\sigma_{WH}$ ) exists and the final region from $\sigma_C$ to $\sigma_{SS}$ would be the DRX zone ($\sigma_{DRX}$). For the initiation of DRX, the critical strain $\varepsilon_C$ was used instead of $\sigma_C$.

### 3.3.1. The work hardening and dynamic recovery (WH) zone:

As mentioned earlier, the below equation was used for the modeling of the WH zone:

$$\sigma_{WH}(\varepsilon, \dot{\varepsilon}, T) = [\sigma_S^2 + (\sigma_0^2 - \sigma_S^2)e^{-\Omega\varepsilon}]^{0.5} \quad \text{Eq. (18)}$$

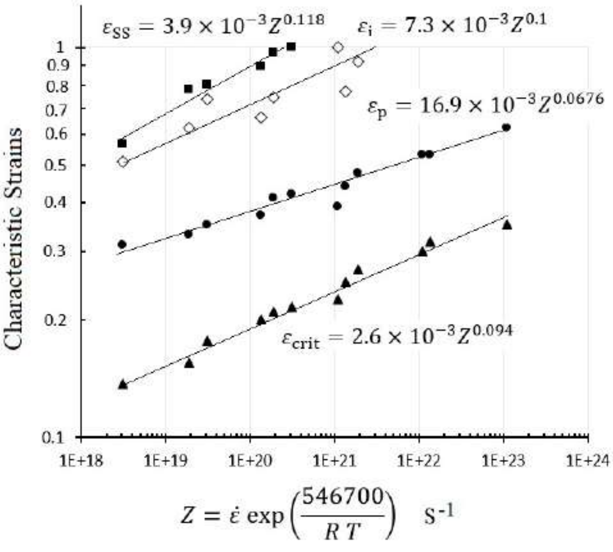

Fig. 4. Characteristic strains of flow curves.

In this equation, three parameters including $\sigma_0$, $\sigma_S$, and $\Omega$ were determined. The parameters $\sigma_0$ and $\sigma_S$ are those before expressed in Table 1 as follows:

$$\sigma_0 = \frac{1}{0.01}\left\{\left(\frac{\dot{\varepsilon}\exp(62425/T)}{3\times 10^{21}}\right)^{1/6.68} + \left[\left(\frac{\dot{\varepsilon}\exp(62425/T)}{3\times 10^{21}}\right)^{2/6.68} + 1\right]^{1/2}\right\} \quad \text{Eq. (19)}$$

$$\sigma_S = \frac{1}{0.0099}\left\{\left(\frac{\dot{\varepsilon}\exp(65432/T)}{1.15\times 10^{19}}\right)^{1/4.45} + \left[\left(\frac{\dot{\varepsilon}\exp(65432/T)}{1.15\times 10^{19}}\right)^{2/4.45} + 1\right]^{1/2}\right\} \quad \text{Eq. (20)}$$

The parameter $\Omega$ is dependent on the temperature, strain rate, and initial grain size as follows:

$$\Omega = A d_0^n \dot{\varepsilon}^m exp(Q_\Omega/RT) \quad \text{Eq. (21)}$$

Wahabi et al. [45] have obtained the below equation for $\Omega$ in 304H stainless steel regarding $Z=\dot{\varepsilon}\ \exp(280{,}000/RT)$ which we used accordingly in this model as follows:

$$\Omega = K_\Omega Z^{m_\Omega} = 110\, Z^{-0.096},\ \ Z = \dot{\varepsilon}\exp(33678/T) \quad \text{Eq. (22)}$$

### 3.3.2. The DRX zone

Once the applied strain reaches the critical strain for the onset of DRX, $\varepsilon_C$, the following equations should be used together for the modeling of the stress-strain curve.

$$\sigma_{DRX} = \sigma_{WH} - X_{DRX}\times(\sigma_S - \sigma_{SS}) \quad \text{Eq. (23)}$$

$$X_{DRX} = 1 - \exp\left[-\left(\frac{\varepsilon - \varepsilon_C}{\varepsilon_{50\%}}\right)^m\right]$$

Equations of $\sigma_{WH}$ and $\sigma_S$ are those expressed before in Eqs. 18 and 20, respectively. The equation of $\sigma_{SS}$ is that said in Table 1 below.

$$\sigma_{SS} = \frac{1}{0.0052}\left\{\left(\frac{\dot{\varepsilon}\exp(58215/T)}{1.6\times 10^{19}}\right)^{1/6.15} + \left[\left(\frac{\dot{\varepsilon}\exp(58215/T)}{1.6\times 10^{19}}\right)^{2/6.15} + 1\right]^{1/2}\right\} \quad \text{Eq. (24)}$$

The critical strain for the onset of DRX, $\varepsilon_C$ may be rewritten as follows:

$$\varepsilon_C = 2.6\times 10^{-3} Z^{0.094} = 2.6\times 10^{-3}\dot{\varepsilon}^{0.094}\exp(6181/T) \quad \text{Eq. (25)}$$

The parameter $\varepsilon_{50\%}$ which is the strain equivalent to the 50% DRX progress could be determined by regarding the strain of the inflection point in stress-strain curve ($\varepsilon_i$) in which $\varepsilon_{50\%}=k\varepsilon_i$. Because overcoming the DRX causes the curvature of the stress-strain curve to change, therefore the strain $\varepsilon_{50\%}$ must be placed before the strain $\varepsilon_i$. We used then the following equation for the strain $\varepsilon_{50\%}$:

$$\varepsilon_{50\%} = 0.7\varepsilon_i = 5.11\times 10^{-3}\dot{\varepsilon}^{0.1}\exp(6576/T) \quad \text{Eq. (26)}$$

It's worth saying that the higher the $\varepsilon_{50\%}$, the greater the width of the concavity portion of the stress-strain curve.

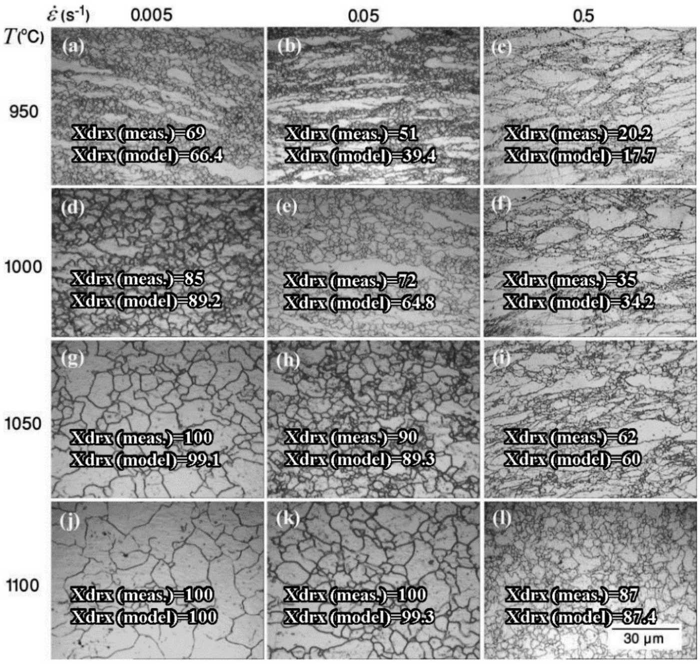

Fig. 5. Microstructures in the quench samples at strain 1 with the evaluated recrystallized fraction (Xdrx (meas.)) compared with the results of model (Xdrx (model)) at different deformation conditions.

Finally, the $m$ value which is a constant showing the transformation kinetics could be determined by considering the DRX evolution at strain 1 at different deformation conditions. The following equation was used for the exponent $m$:

$$m = 8.7 \times 10^{-7} \dot{\varepsilon}^{0.03} T^{2.1} \qquad \text{Eq. (27)}$$

Fig. 5 shows the microscopic images taken from the quench samples at strain 1 which the recrystallized fractions calculated experimentally as well as those predicted by the model. Fig. 6 implies that there is a good coincidence between the model results and the experimental evidence.

### 3.3.3. Evaluation of the model

The above equations were used to draw the stress-strain curves at different conditions. Fig. 7 shows the stress-strain curves derived from the model (dotted curve) as compared with the experimental equivalents. There is a satisfactory coincidence between them.

The advantage of the method used in this study for predicting flow curves compared to methods employing four or seven polynomial fittings for A, $\alpha$, n, and Q, [8,9] is the prediction of microstructure evolution together with the flow curve. Moreover, this model is based on well-known characteristic stresses and strains.

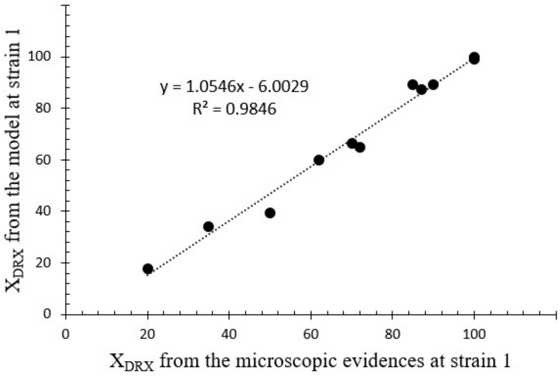

Fig. 6. DRX fraction evaluation from the microstructure against the model results.

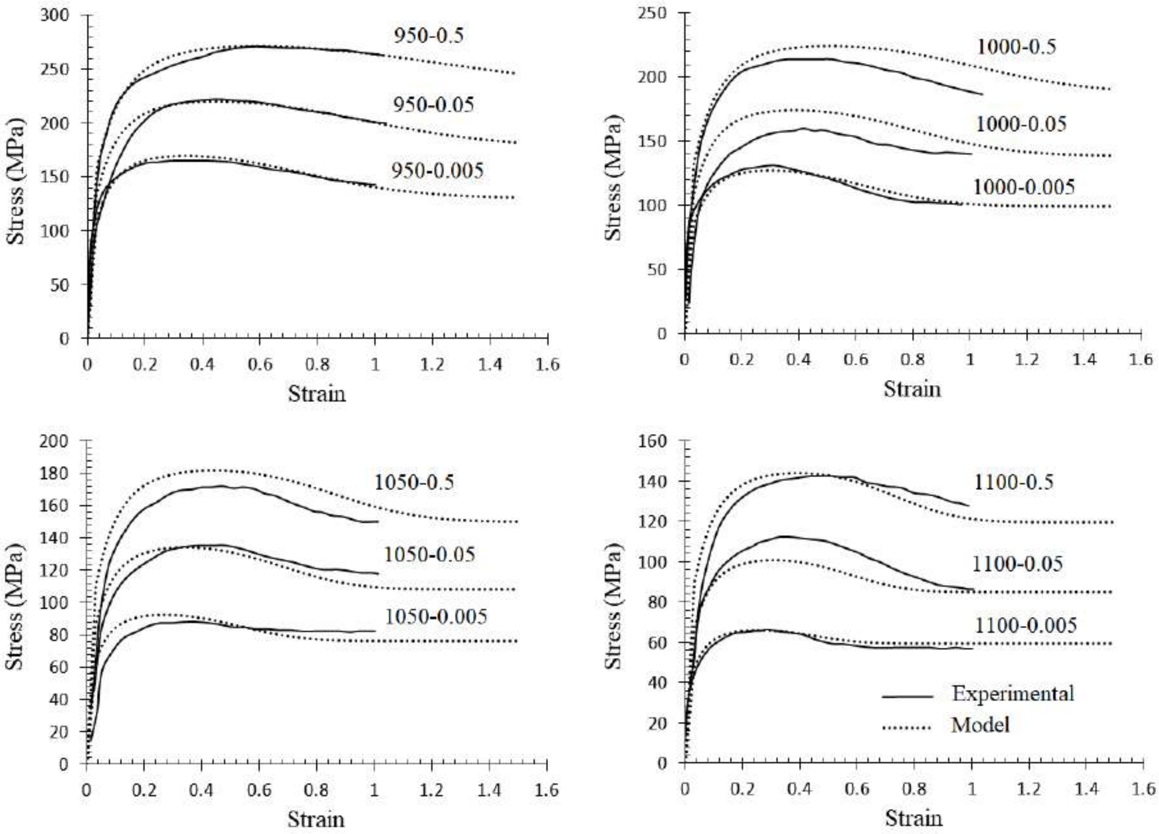

Fig. 7. Stress-Strain curves: Experimental (solid line) against the model results (dotted line).

## 4. Conclusions

In this study, AISI 304 stainless steel was used in hot compression tests at the temperatures of 950-1100 °C and strain rates of 0.005-0.5 $s^{-1}$ up to the strain of 1. The following results could be extracted:

- The characteristic stresses including yield, critical, peak, saturation, and steady-state stresses were obtained and represented via Zener–Hollomon parameter in an Arrhenius-type equation. Also, the characteristic strains were obtained as well.
- To model flow curves, equations were presented for different regions including the elastic zone up to yield stress, the work-hardening zone from yield to onset of DRX, and the DRX region from initiation point of recrystallization toward steady-state stress.
- By comparison, a satisfactory coincidence was found between the experimental results and flow curves obtained by the proposed model. Moreover, the model could predict well the kinetics of DRX as compared with the experimentally evolved microstructures.

## Acknowledgments

The present work has been supported by the vice president of education and research of the Qom University of Technology (QUT).

## References

[1] D.S. Fields, W.A. Backofen, Determination of Strain Hardening Characteristics by Torsion Testing, Proceedings-American Society of Testing Materials. 57 (1957) 1259-1272.

[2] K. Nitin, N.K. Hansoge, K.G. Amit, K.S. Swadesh, Study of Hot Deformation Behavior Using Phenomenological Based Constitutive Model for Austenitic Stainless Steel 316, Mater Today: Proceedings. 5 (2018) 4870-4877.

[3] G. Ji, L. Li, F. Qin, L. Zhu, Q. Li, Comparative study of phenomenological constitutive equations for an as-rolled M50NiL steel during hot deformation, J. Alloy Compd. 695 (2017) 2389-2399.

[4] Y.C. Lin, X. Chen, A critical review of experimental results and constitutive descriptions for metals and alloys in hot working, Materials and Design. 32 (2011) 1733-1759.

[5] W.J. Lu, L.Q. Hou, X.Q. Zhang, P.M. Xu, Thermal deformation properties and Johnson-Cook models for superaustenitic stainless steel, J. Plasticity Eng. 23 (2016) 125-130.

[6] H. R. Rezaei Ashtiani, A. A. Shayanpoor, Trans. Nonferrous Met. Soc. China. 31 (2021) 345−357.

[7] Y. Ban, Y. Zhang, Y. Jia, B. Tian, A. A. Volinsky, X. Zhang, Q. Zhang, Y. Geng, Y. Liu, X. Li, Effects of Cr addition on the constitutive equation and precipitated phases of copper alloy during hot deformation. Materials and Design. 191 (2020) 108613.

[8] S. Aliakbari Sani, G.R. Ebrahimi, H. Vafaeenezhad, A.R. Kiani-Rashid, Modeling of hot deformation behavior and prediction of flow stress of a magnesium alloy using constitutive equation and artificial neural network (ANN) model, Journal of Magnesium and Alloys. 6 (2018) 134–144.

[9]H. Wu, J. Yang, F. Zhu, C. Wu, Hot compressive flow stress modeling of homogenized AZ61 Mg alloy using strain-dependent constitutive equations, Materials Science & Engineering A. 574 (2013) 17–24.

[10] Q. Dai, Y. Deng, J. Tang, Y. Wang, Deformation characteristics and strain-compensated constitutive equation for AA5083 aluminum alloy under hot compression, Trans. Nonferrous Met. Soc. China. 29 (2019) 2252−2261.

[11] F.J. Zerilli, R.W. Armstrong, Dislocation-mechanics-based constitutive relations for material dynamics calculations, Journal of Applied Physics. 61 (1987) 1816-1825.

[12] X. Huang, B. Wang, Y. Zang, H. Ji, B. Guan, Y. Li, X. Tang, Constitutive relationships of 21-4 N heat-resistant steel for the hot forging process, J Mater. Res. Technol. 9(6) (2020) 13575–13593

[13] A. Hensel, T. Spittel. Kraft- und Arbeitsbedarf bildsamer Formgebungsverfahren. VEB DeutscherVerlag fur Grundstoffindustrie, Leipzig, 1978, ISBN: 5991fb-6601cdf532e1408fc6566c7635

[14] A. Tabei, F. H. Abed, G. Z. Voyiadjis, H. Garmestani, Constitutive Modeling of Ti-6Al-4V at a Wide Range of Temperatures and Strain Rates, European Journal of Mechanics /A Solids. 63 (2017) 128-135.

[15] C. Zener, H. Hollomon,. Effect of strain-rate upon the plastic flow of steel. J. Appl. Phys. 15 (1944) 22–27.

[16] J.J. Jonas, C.M. Sellars, M.W.J. Tegart, Strength and structure under hot working conditions. Int. Met. Rev. 14 (1969) 1–24.

[17] E.I. Poliak, J.J. Jonas, Initiation of dynamic recrystallization in constant strain rate hot deformation, ISIJ Int. 43(5) (2003) 684-691.

[18] E.I. Poliak, J.J. Jonas, Critical strain for dynamic recrystallization in variable strain rate hot deformation, ISIJ Int. 43(5) (2003) 692-700.

[19] W. Roberts, B. Ahlblom, A nucleation criterion for dynamic recrystallization during hot working, Acta Metall. 26 (1978) 801-813.

[20] A. Najafizadeh, J.J. Jonas, Int. J. ISSI. 3 (2006) 1.

[21]R. Sandstrom, R. Lagneborg, Acta Metall. 23 (1975) 387.

[22]A. Laasraoui, J.J. Jonas, Prediction of steel flow stresses at high temperatures and strain rates, Metall. Trans. A 22A…. (1991) 1545-1558.

[23]W. Wei, K.X. Wei, G.J. Fan, A new constitutive equation for strain hardening and softening of FCC metals during severe plastic deformation, Acta Mater. 56

(2008) 4771–4779.

[24] Y. Estrin, H. Mecking, Acta Mater. 32 (1984) 57.

[25] W. Roberts, Deformation, Processing and Structure, ASM Handbooks, Metals Park, OH, p. 109, 1984.

[26] J.J. Jonas, X. Quelennec, L. Jiang, M. Etienne, The Avrami kinetics of dynamic recrystallization, Acta Mater. (2009) 114-119.

[27] S.I. Kim, Y.C. Yoo, Mater. Sci. Eng. A. 311 (2001) 108.

[28] R. Ebrahimi, A. Najafizadeh, J. Mater. Proc. Tech. 152 (2004) 136.

[29] M.S. Mohebbi, M.H. Parsa, M. Rezayat, Analysis of Flow Behavior of an Nb-Ti Microalloyed Steel During Hot Deformation, Metall Mater Trans A. 49 (2018) 1604–1614. https://doi.org/10.1007/s11661-018-4536-0

[30] J.M. Cabrera, A. Al Omar,J.M. Prado, Modeling the flow behavior of a medium carbon microalloyed steel under hot working conditions, Metall Mater Trans A. 28 (1997) 2233–2244. https://doi.org/10.1007/s11661-997-0181-8

[31] J. Long, Q. Xia, G. Xiao, Y. Qin, S. Yuan, Flow characterization of magnesium alloy ZK61 during hot deformation with improved constitutive equations and using activation energy maps. Inter. J. Mech. Sci. 191 (2021) 1060-69.

[32] A. Dehghan-Manshadi, P.D. Hodgson, Metall. Mater. Trans. A 39 (2008) 28-30.

International Journal of ISSI, Vol. 19(2022), No. 2, pp. 22-32

# Effect of melt height and obstacle on fluid dynamics in six-strand tundish: A numerical study

**M. Mohammadi Soleymani [1], K. Dolati Asl [2], E. Mehrabi Gohari *[3]**

*[1, 3] Department of Mechanical Enginneering, Payame Noor University (PNU), Tehran, Iran*
*[2] Department of Mechanical Enginneering, University of Hormozgan, Bandar Abbas, Iran*

---

## Abstract

Tundish, as a continuous metallurgical operator, provides steel for continuous casting molds with optimum flow rates, constant temperatures, uniform chemical compositions, and low porosity. The cleanliness of the molten steel entering the mold is affected by the type of flow pattern and the performance of the tundish in flotation and removal of non-metallic impurities. In this paper, the fluid flow and heat transfer in a tundish in 2 cases, without an obstacle and with an obstacle, the turbo-stop, which is installed at its bottom and across the melt input, is simulated using the Ansys Fluent at melt heights of 0.5, 0.65, and 0.75 m. Results show that the formation of the second circulating flow inside the obstacle is the most important reason for the input melt velocity reduction. Increasing the melt height leads to a more uniform and less turbulent flow. Furthermore, increasing the melt height from 0.5 m to 0.75 m leads to a 3 % reduction in the average flow velocity. The highest heat transfer loss is from the top surface of the tundish and thus, the most temperature gradient exists at the top surface of the melt. The flow movement paths from the tundish input show that the melt flow velocity towards the sides of the tundish is increased with the melt height inside it. Furthermore, higher melt height causes the formation of higher stagnant melt volume inside the tundish, which negatively influences the inclusion of absorption by the slag.

*Keywords:* Continuous casting; Steel making; Tundish; Fluid dynamics; Numerical modeling; Ansys fluent.

---

## 1. Introduction

The melt in the ladle is distributed in casting lines using a distributor device called tundish, Fig. 1. The casting time period is mainly influenced by the melt height inside the tundish. According to the hydrostatic pressure of the melt, more melt exits from the outlet nozzles as the melt inside the tundish is increased [1].

In the steel continuous casting process, the tundish provides sufficient melt for creating and maintaining a continuous flow to the mold even during ladle substitutions. The ladles are periodically filled and returned from the steel-making process. Furthermore, the tundish can act as a filter container by floating the inclusions as a slag layer. If solid impurity particles are allowed to remain in the product, then surface defects such as the porosity and expansion scab can be formed in the subsequent rolling processes or lead to the internal local stress concentration which can decrease the fatigue lifetime of the product. To produce high-quality products, the molten steel needs to be protected from interacting with the air by the slag coverage on the melt free-surface and use the ceramic-made nozzles between the containers. Otherwise, the oxygen of the air reacts with the steel which leads to the formation of detrimental oxide inclusions [2-4].

---

*Corresponding author
Email: e.mehrabi@pnu.ac.ir
Address: Department of Mechanical Enginneering, Payame Noor University (PNU), Tehran, Iran
1. Assistant Professor
2. PhD
3. Assistant professor*

Fig. 1. Tundish of the South Kave Steel (SKS) Company.

Various numerical and experimental studies have been conducted to investigate the flow in the tundish by researchers [5-7]. Most researchers in the experimental method simulate water at room temperature and at uniform temperature and steady-state flow. Mickey and Thomas [8] and Sousa Rocha, et al. [9] have done mathematical modeling to analyze the flow in a tundish with a specific geometry. They simulated the three-dimensional flow of molten steel and its temperature changes in tundish in both steady and unsteady states using the K-ε turbulence model. They used the Lagrangian tracking model to analyze particle motion. In this research, the residence time and density of the number of particles with different sizes have been investigated. In a study of a ten-strand tundish in the form of physical modeling, it was found that among the ten tundish outlets, the output that has the minimum residence time and the emergence of the detector is observed earlier has the worst performance in separating the inclusions. Also, the distribution of the number of inclusions between the strands is the same for each size of the inclusions and the descending order of the number of inclusions is based on the descending order of the average retention time between the strands [10]. Other research [11-14] Using mathematical and physical modeling, the effect of using flow control equipment on porosity separation has been investigated.

In other studies, a novel swirling flow generator (SFG) is intended to be installed around the inlet of the submerged entry nozzle (SEN) in the tundish to generate a swirling flow in the SEN by utilizing gravitational potential energy. The radial pressure gradient force causes inclusion particles to move toward the center. In the central area in the SEN, the collision rate between inclusion particles and bubbles increases significantly. Thus, bubble injection in swirling flow is beneficial to the removal of inclusion particles [15, 16]. The use of experiments and numerical simulations for flow behaviors of the tundish has been done by researchers. CFD modeling methods were employed in the studies. The obtained CFD results were compared with the results of laboratory tests (using a tundish water model) [17, 18].

The South Kave Steel (SKS) company, one of the largest steel-production companies in Iran, has a plan for removing the inclusion from the melt and producing clean steel. The tundish type of this company is completely different from those used in other steel-making factories in terms of the tundish geometry, dimensions and melt capacity, input melt place, and the number of outlet nozzles. Therefore, the tundish of this company in 2 cases, without an obstacle and with an obstacle, turbo-stop, is modeled and simulated in current research. This will be used as the first phase of a larger research program which will provide for a comprehensive study of the distribution of nonmetallic inclusions flowing through tundish steel.

## 2. Materials and research methods

In the discussion of modeling, different steps should be taken. In the initial stage, it is necessary to define a specific model for the geometry of the problem. This will be done by Solid Works software and the model with a different format will be saved for reading in Ansys Fluent computing software. Finally, by selecting the appropriate modules for modeling, the constructed model is called. Since the flow of fluid at the inlet and outlet areas is turbulent, in order to mathematically model such a system, it is necessary to apply a series of assumptions to simplify the system:

A: The free surface is considered smooth. Due to the presence of slag coating on the melt, in most cases, researchers have avoided wavy movements on the melt surface and considered the surface to be smooth.

B: Any trapping of air or gas when the melt stream enters is avoided.

C: Since the density of molten steel is a function of temperature, floating forces will be generated due to the temperature difference between different points of the fluid. The presence of these buoyancy forces affects the behavior of the fluid flow in the tundish, so it will be effective in removing and floating impurities. Therefore, heat transfer is another important consideration in tundish operations. Basically, temperature changes in tundish melt are caused by the discharge of melt at different temperatures from the pan to tundish, as well as heat loss through the walls (conductive heat transfer to the atmosphere) and through the slag coating (radiant heat transfer) [13].

## 2.1. Tundish geometry

The geometric characteristics of the six-strand tundish used in South Kave Steel (SKS) Company are shown in Fig. 2. The height of the melt inside the tundish is between 50 and 80 cm, but its application range, which is mostly used in steel-making, is 60 to 65 cm. The diameter of the outlet nozzles is 17 mm. For modeling the obstacle geometry at the tundish bottom (in case 2), the obstacle is supposed to be a cylinder with a height of 27 cm, an internal diameter of 23 cm, and a wall thickness of 2 cm.

## 2.2. The governing equations

Navier-Stokes equations are used to solve the fluid dynamics inside the tundish [19].

1) Continuity equation

$$\frac{\partial \rho}{\partial t} + \rho(\nabla u) = 0 \qquad \text{Eq. (1)}$$

2) Momentum equation

$$\rho\frac{\partial u}{\partial t} + \rho[u \cdot \nabla]u = -\nabla P + \mu_{eff}\nabla^2 u + \rho g \qquad \text{Eq. (2)}$$

Where t is time, $\rho$ is the fluid density, $u$ is velocity, $p$ is pressure, $g$ is the acceleration of gravity, and $\mu_{eff}$ is effective turbulent viscosity. Which is $\mu_{eff}$ the sum of $\mu$ molecular viscosity and $\mu_t$ turbulent viscosity.

$$\mu_{eff} = \mu + \mu_t = \mu + \rho C_\mu \frac{k^2}{\varepsilon} \qquad \text{Eq. (3)}$$

and $C_\mu = 0.09$

3) Turbulence equations

Two standard equations are used to express the model $k$-$\varepsilon$ in turbulence modeling, $k$ which are two equations for the kinetic energy transfer of turbulence, and $\varepsilon$ its displacement rate. The equation for turbulent kinetic energy is as follows.

$$\rho\frac{\partial k}{\partial t} + \rho\frac{\partial k u_i}{\partial x_i} = \frac{\partial}{\partial x_j}\left[\left(\mu + \frac{\mu_t}{\sigma_k}\right)\frac{\partial k}{\partial x_j}\right] + G_k - \rho\varepsilon \qquad \text{Eq. (4)}$$

The $G_k$ kinetic energy production of turbulence is from the mean velocity gradient and is obtained from Eq. 5.

$$G_k = \mu_t \frac{\partial u_j}{\partial x_i}\left(\frac{\partial u_i}{\partial x_j} + \frac{\partial u_j}{\partial x_i}\right) \qquad \text{Eq. (5)}$$

The turbulent energy dissipation rate is obtained from Eq. 6.

$$\rho\frac{\partial \varepsilon}{\partial t} + \rho\frac{\partial \varepsilon u_i}{\partial x_i} = \frac{\partial}{\partial x_j}\left[\left(\mu + \frac{\mu_t}{\sigma_\varepsilon}\right)\frac{\partial \varepsilon}{\partial x_j}\right] + C_{l\varepsilon}\frac{\varepsilon}{k}G_k - C_{2\varepsilon}\rho\frac{\varepsilon^2}{k} \qquad \text{Eq. (6)}$$

That $x_i$ and $x_j$ are the Cartesian components of velocity and the experimental turbulence constants are shown in Table 1.

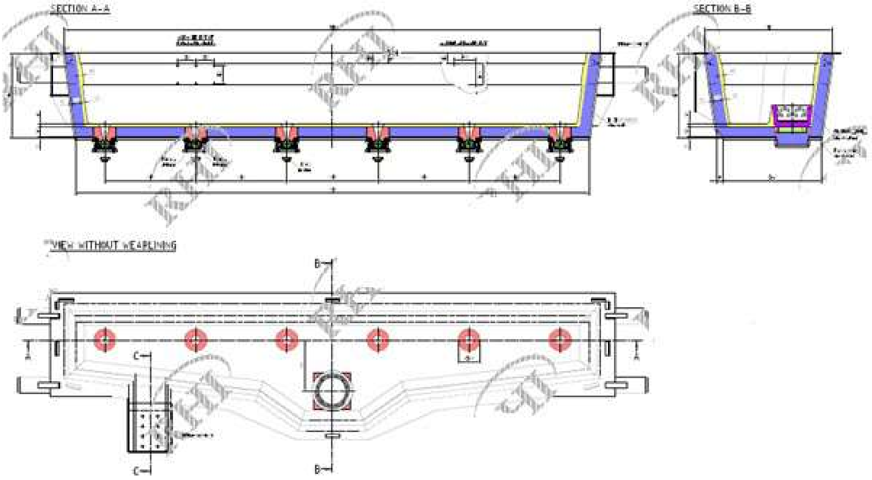

Fig. 2. Tundish geometric characteristics.

Table 1. The proposed experimental constants of turbulence [19].

| $C_{1\varepsilon}$ | $C_{2\varepsilon}$ | $\sigma_k$ | $\sigma_\varepsilon$ | $C_\mu$ |
|---|---|---|---|---|
| 1.38 | 1.92 | 1 | 1.3 | 0.09 |

4) Energy equation

An energy equation is needed to calculate the temperature of the molten fluid.

$$\frac{\partial}{\partial t}(\rho E) + \nabla \cdot [u(\rho E + P)] = \nabla \cdot \left(k_{eff}\nabla T - \left(h + \frac{P}{\rho}\right) + \left(\tau_{eff} \cdot u\right)\right) \qquad \text{Eq. (7)}$$

That $T$ is temperature and $\tau_{eff}$ is the viscous dissipation term and $k_{eff}$ is effective conductivity and from the relation $k_{eff}=k+k_t$ it follows that $k_t$ is the turbulent thermal conductivity. The energy E is obtained from Eq. 8.

$$E = h - \frac{P}{\rho} + \frac{u^2}{2} \qquad \text{Eq. (8)}$$

Also, $h = \int_{T_{ref}}^{T} C_P dT$ is and $T_{ref}$ is reference temperature and $C_P$ is constant pressure heat capacity.

## 2.3. Thermal properties and boundary conditions

The mass flow rate of the inlet melt to the tundish is 50 kg $s^{-1}$ and its temperature is 1530°C, which is close to the actual conditions. Melt density is a function of temperature and is equal to $\rho$=7010-0.883($T$-1818). The viscosity is 0.007 kg $m^{-1}$ $s^{-1}$ and the heat capacity is 720 J $kg^{-1}$ $K^{-1}$ and the thermal conductivity is 33 W $m^{-1}$ $K^{-1}$. Because the walls of the melt and the top surface of the melt exchange heat with the surrounding environment, and because the temperature of the melt and the melt is higher than the ambient temperature, heat is transferred from the melt to the environment and the melt temperature decreases. Based on previous studies [19, 20], the amount of heat loss from the top surface of the melt, hard floor, and hard walls are 15, 1.5, and 3.5 kW/$m^2$, respectively (Table 2).

Because of the symmetry in the overall geometry of the tundish, only half of the tundish is considered the computational domain, which according to Fig. 3, one side of the domain is defined by the symmetry boundary condition. The side walls and the floor of the ramp are marked with the condition of non-slip. The upper level of the solution amplitude is empty space, which is why the condition without shear stress is used. The melt flow inlet at the top of the slope is considered the velocity input and the melt flow output at the bottom of the geometry is considered the pressure output (pressure equal to atmospheric pressure).

Table 2. Thermal properties of the melt and boundary conditions of heat dissipation [19].

| Thermal properties | | heat transfer loss | |
|---|---|---|---|
| melt density | $\rho = 7010 - 0.883(T - 1818)$ | melt top surface | $15\ \mathrm{kW\,m^{-2}}$ |
| melt viscosity | $0.007\ \mathrm{kgm^{-1}s^{-1}}$ | tundish bottom | $1.5\ \mathrm{kW\,m^{-2}}$ |
| thermal capacity | $720\ \mathrm{J\,kg^{-1}K^{-1}}$ | tundish walls | $3.5\ \mathrm{kW\,m^{-2}}$ |
| thermal conduction coefficient | $33\ \mathrm{W\,m^{-1}K^{-1}}$ | | |

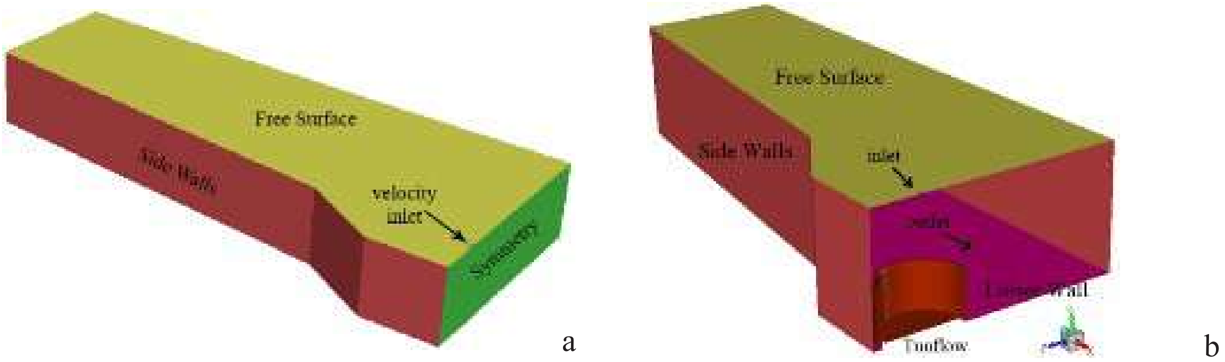

Fig. 3. Model of solution domain created in Ansys software
a) without an obstacle b) with an obstacle.

Since the height of the melted fluid inside the tundish is variable, in the present study, the amount of melt height inside the tundish is considered in three states of 50, 65, and 75 cm, based on which three solution amplitudes are modeled. In the present study, the variable h indicates the amount of melt height within the tundish. The meshes used for each case (different heights) ranged from 3.3 to 3.7 million grids. At the same time, the sensitivity analysis for the suitable mesh has also been done. A model similar to reference [19] was run in Ansys Fluent and the results were consistent. The temperature at different points of the Tundish and the exit speed of the nozzle in industrial trials were calculated and the results were consistent with the modeling of this research.

## 3. Results and discussion

In this study, the tundish behavior of the flow pattern and heat distribution in 2 cases, without an obstacle and with an obstacle, turbo-stop, was investigated. Figs 4 and 5 show part of the movement path of the input melt to the tundish at two melt heights of h = 0.5m and h = 0.75m without an obstacle and with obstacle case. As observed, the input melt flow to the tundish impacts the bottom surface (or obstacle bottom surface) inside the tundish vertically and uniformly due to the high velocity of the input flow. After impacting the obstacle walls, the flow moves upward and then the fluid flow circulation inside the tundish is started. The highest fluid flow velocity and turbulence occur in the middle part of the tundish which is nearer the input melt flow region. At the end of the tundish, the existent melt is less affected by the tundish input. A comparison between Figs. 4 and 5 shows that the movement and turbulence of the molten fluid flow are increased at the middle and end part of the tundish respectively, by decreasing and increasing the melt height inside the tundish. Furthermore, it can be inferred from the comparison that the direct input fluid flow effect and mixing and turbulence in the flow are reduced as the melt height is increased. Therefore, to have a more laminar flow that enhances the movement of inclusion towards the free surface of the fluid, the melt height is better to be increased. Besides, according to Figs. 4 and 5, the reflected flow from the nearer wall to the input melt region moves to a higher height. Therefore, reducing the intensity of this flow would be a proper way for decreasing the turbulence in the inclusion.

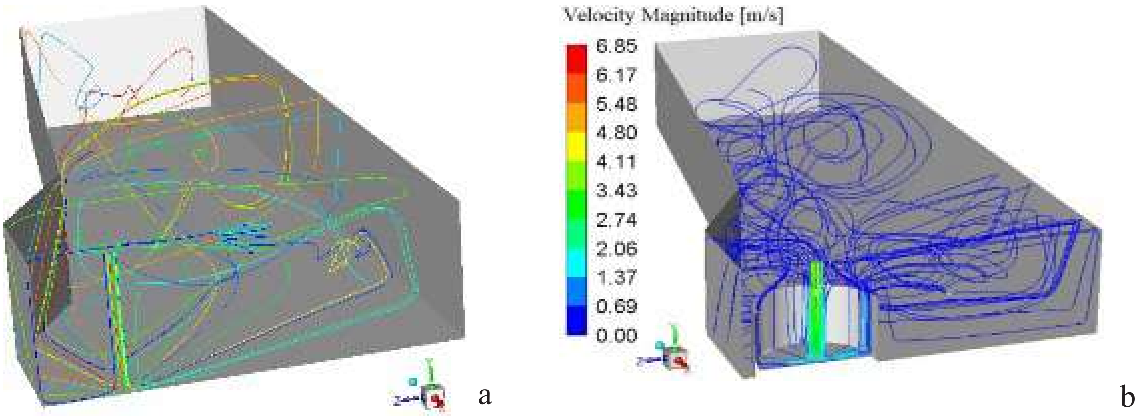

Fig. 4. Part of the path of the incoming melt to Tundish (h = 0.5m)
a) without an obstacle b) with an obstacle.

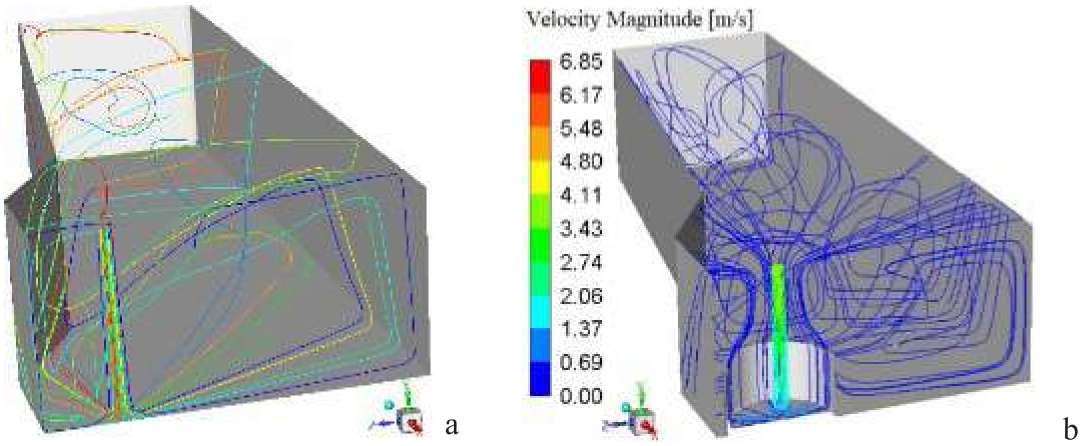

Fig. 5. Part of the inlet melt path to the tundish (h = 0.75m)
a) without an obstacle b) with an obstacle.

The obstacle at the tundish bottom (in the case of an obstacle) is installed for controlling the entering melt into the tundish, and the flow paths are shown in Fig. 6 in a magnified view. The input flow moves towards the tundish bottom with high velocity and after impacting the obstacle bottom moves upwards due to the obstacle walls. As observed, part of the reflected upward-moving flow is driven towards the input flow due to the pressure reduction near that. Therefore, a secondary circulating flow is formed inside the obstacle. Part of the obstacle which is nearer to the tundish wall has the lowest circulating flow.

Fig. 7 shows the melt velocity vector on a longitudinal plane passing through the outputs (in the case without an obstacle). It should be noted that for a better display of velocity vectors in low-velocity areas, the maximum velocity is 0.2 m/s. The melt jet strikes the impact pad hard on the floor of the tundish and the melt expands radially. In the upper part of tundish, you can see areas with above-average speed as well as an area with very low speed. When the upstream flow from the inlet to the farthest sides of the tundish, it returns from the bottom to the inlet area at above-average velocities. This produces some shock due to the downstream current. Based on Fig. 7, it can be clearly seen that there is less melt flow in places far from the center of the tundish.

The flow path in the symmetry plane of the tundish in the case of an obstacle is shown in Fig. 8. The maximum fluid flow velocity is related to the input flow and flows on the internal walls of the obstacle. As mentioned before, the secondary circulating flow inside the obstacle is harsh, which has a considerable effect on the flow velocity reduction in the tundish. According to Fig. 8, the melt flow exists in all points of the symmetry plane, but the velocity is different at different points of the plane. Finally, a more regular flow can have certain advantages for the quality of the steel, such as better thermal homogenization and greater particle removal.

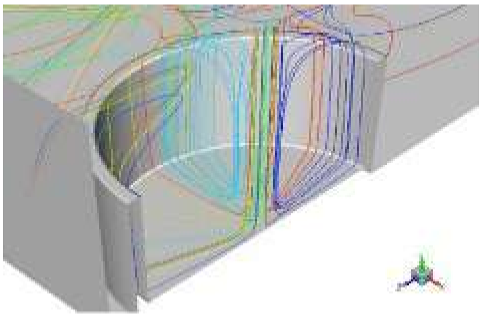

Fig. 6. The obstacle at the tundish bottom (in the case of an obstacle), which is installed for controlling the entering melt into the tundish, and the flow paths.

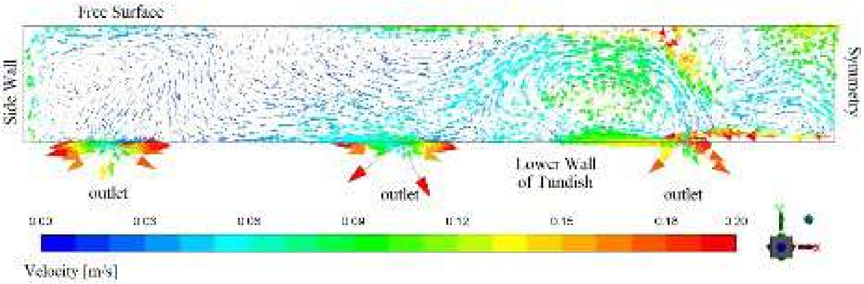

Fig. 7. The melt velocity vector on a longitudinal plane passing through the outputs (in the case without an obstacle).

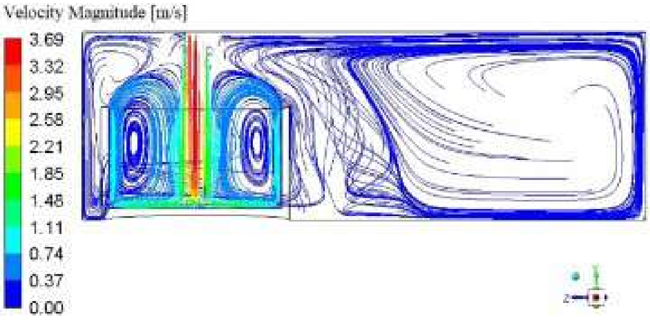

Fig. 8. The flow path at the symmetry plane of the tundish in the case with an obstacle h=0.5m.

The velocity contours in the symmetry plane of the tundish in the case of obstacle are shown in Fig. 9 and Fig. 10 for h = 0.5 m and h = 0.75 m, respectively. The highest flow velocity belongs to the input flow to the tundish, which its velocity is remarkably reduced after impacting the obstacle. The input flow has to move a longer path as the melt height is increased and because the density and viscosity of the melt are high, the input flow velocity is reduced remarkably. Therefore, the impact velocity of the flow onto the obstacle is decreased with the melt height. Furthermore, it can be concluded by comparing Figs. 9 and 10 that the circulating flow intensity and flow turbulence are considerably decreased as the melt height inside the tundish is increased, which has a considerable effect on the inclusion formation as well.

The overall absolute velocity contours on the melted top and side surfaces in 2 cases, without an obstacle, and with an obstacle, turbo-stop, are shown in Figs 11 to 13 for melt heights of 0.5, 0.65, and 0.75 m. The maximum flow velocity is 0.73 m/s occurring at the melt input to the tundish, for all three melt heights. For a better contour representation, the maximum velocity is set to 0.5 m/s to better observe the velocity changes. Since the no-slip boundary condition is applied to the sidewalls of the tundish, the flow velocity is zero there. As observed, the maximum flow velocity on the melt surface is not changed considerably with the melt height and is nearby the input melt to the tundish. The average velocity on the melt surface is calculated to be 0.0765, 0.0753, and 0.0745 m/s for h = 0.5, 0.65, and 0.75 m, respectively. Therefore, the average velocity also does not change considerably with the melt height. However, the absolute flow velocity is changed more uniformly near the melt input as the melt height is increased. Furthermore, the tundish with a higher melt height has more still regions. Higher still melt volume in the tundish has a negative effect on the inclusion absorption [4].

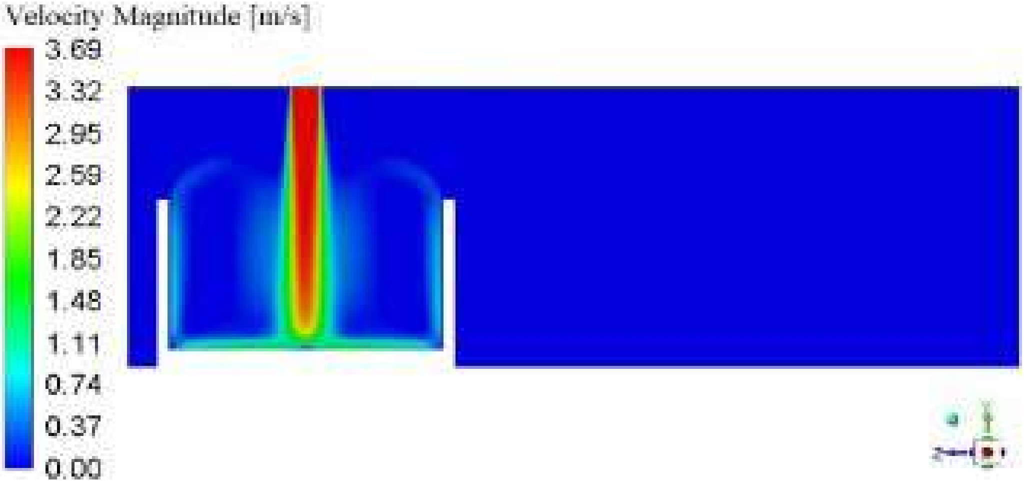

Fig. 9. The velocity contours in the symmetry plane of the tundish in the case of obstacle h=0.5m.

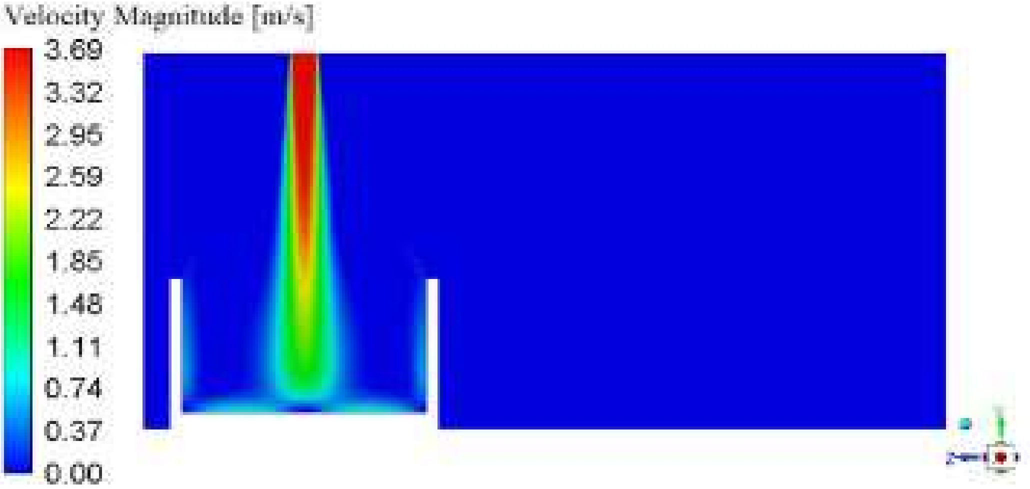

Fig. 10. The velocity contours in the symmetry plane of the tundish in the case of obstacle h=0.75m.

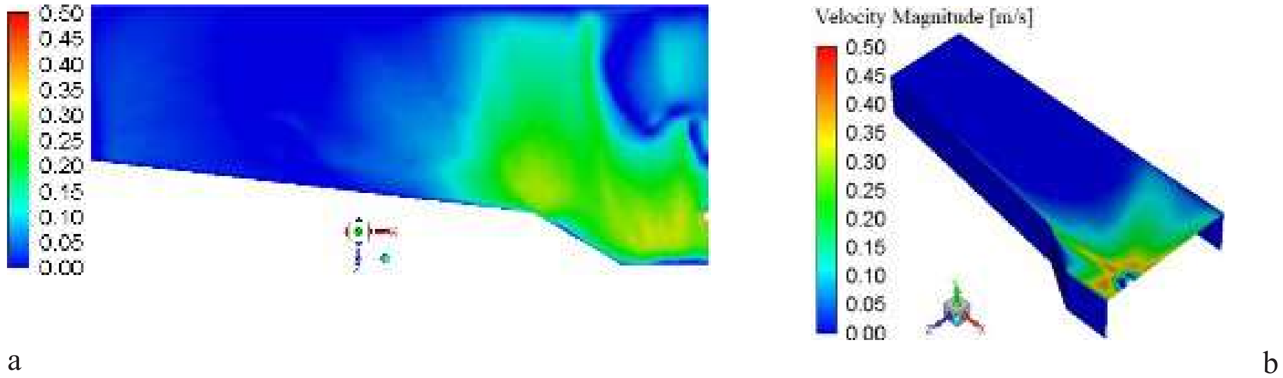

Fig. 11. The overall absolute velocity contours on the melted top and side surfaces h=0.5m
a) without an obstacle b) with an obstacle.

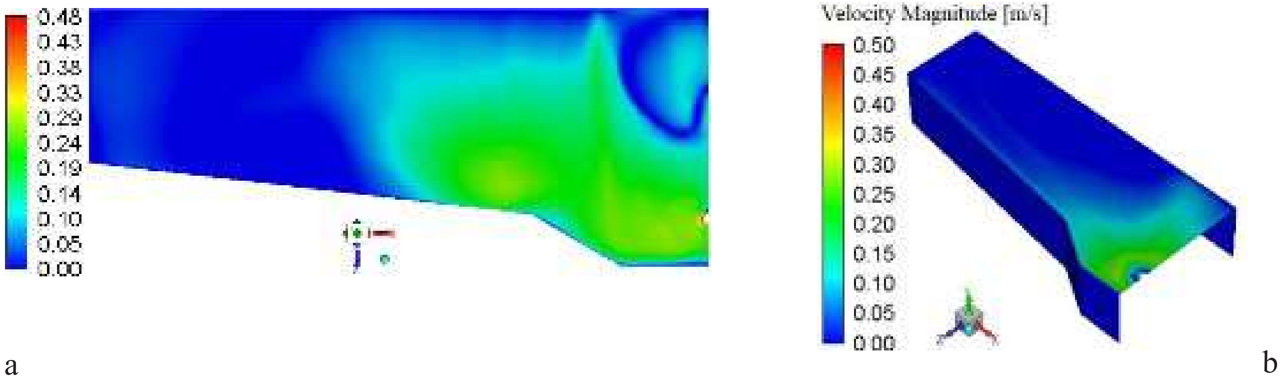

Fig. 12. The overall absolute velocity contours on the melted top and side surfaces h=0.65m
a) without an obstacle b) with an obstacle.

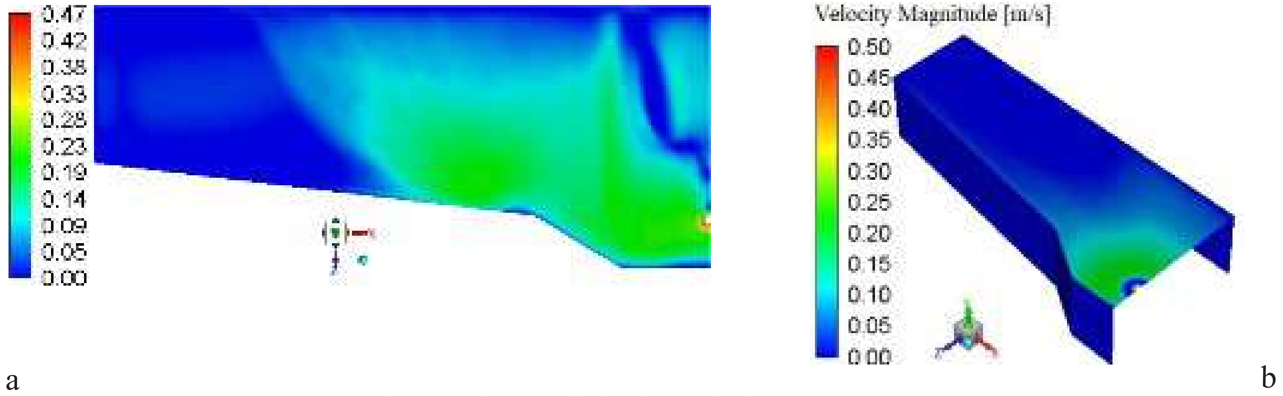

Fig. 13. The overall absolute velocity contours on the melted top and side surfaces h=0.75m
a) without an obstacle b) with an obstacle.

Fig. 14 shows the velocity vectors on a longitudinal surface passing the outlets for h=0.5 and 0.75m (in the case of an obstacle). It should be mentioned that the maximum velocity is considered to be 0.12 m/s for a better representation of the velocity vectors in low-velocity regions. In both conditions, the circulating flow regions are clearly observed with a higher intensity at h=0.5m, which influences the slag. As the melt height is increased, the outlet flow velocity is increased, leading to faster casting.

Figs 15 and 16 show the absolute temperature and velocity counters on the lateral walls of the tundish and the upper surface of the melt (in the case without an obstacle), which cause heat loss to the environment, respectively. For a better display of fluid velocity counters, the maximum velocity value in this contour is 0.45 m/s. In these two Figs, a very good correlation is observed between fluid dynamics and temperature distribution; as the melt moves faster, it loses more heat due to an increase in the amount of heat transfer coefficient. The difference between the inlet temperature (1530°C) and the coldest tundish point (1518°C) is only 12°C. One of the ways to make the outlet flow of the tundish more uniform is to make the melt in the tundish more uniform in terms of heat. Accordingly, the use of turbo stops (obstacles) to melt movement in the tundish is recommended to make the melt flow more uniform.

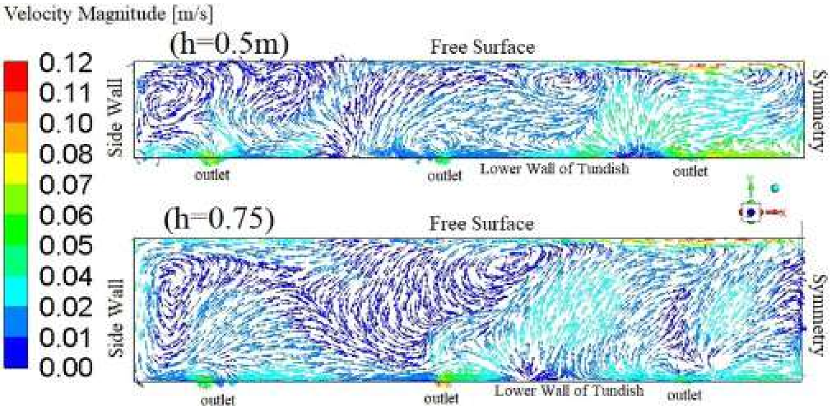

Fig. 14. The velocity vectors on a longitudinal surface passing the outlets for h=0.5m and 0.75m (in the case of an obstacle).

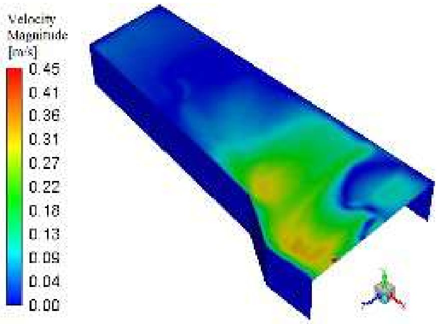

Fig. 15. The absolute velocity counters on the lateral walls of the tundish and the upper surface of the melt h=0.5m (in the case without an obstacle).

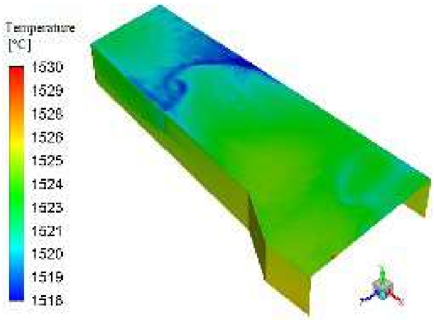

Fig. 16. The absolute temperature counters on the lateral walls of the tundish and the upper surface of the melt h=0.5m (in the case without an obstacle).

The melt temperature contours on the top and side surfaces of the tundish in the case of an obstacle are shown in Fig. 17 and Fig. 18, respectively. The average temperature on top and side surfaces is 1524.2°C and 1524°C respectively for h=0.5m and h=0.75m, which is almost the same value. However, surfaces with the maximum temperature, at the top surface of the melt, are reduced with the melt height. Since the density of the molten steel is varied with the temperature, the buoyancy forces are formed in the tundish due to the temperature difference in the melt. The presence of the buoyancy forces changes the flow behavior such that the inclusion removal and floating are influenced by them. Therefore, the heat transfer in the tundish is another important factor that needs to be considered. The temperature changes of the melt are due to pouring melt with different temperatures from the ladle and heat losses from the tundish walls, through the conduction, and the slag coverage through the radiation.

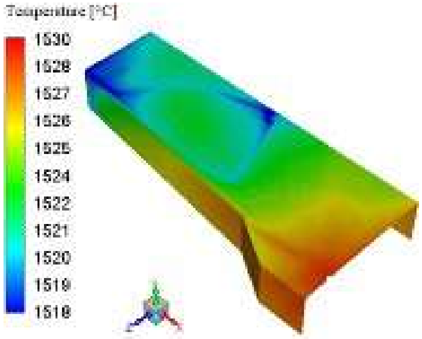

Fig. 17. The melt temperature contours on the top and side surfaces of the tundish in the case of an obstacle h=0.5m.

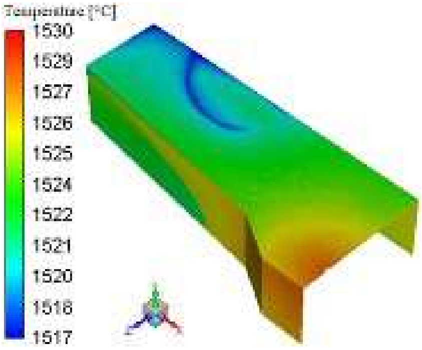

Fig. 18. The melt temperature contours on the top and side surfaces of the tundish in the case of an obstacle h=0.75m.

## 4. Conclusions

The following results are obtained from modeling and simulation of the steel continuous casting tundish for evaluating and comparing the flow pattern:

- The use of turbo stops to melt movement in the tundish makes the melt flow more uniform, and a more regular flow can have certain advantages for the quality of the steel, such as better thermal homogenization and greater particle removal.
- A strong circulating flow is formed inside the tundish because the input melt flow directly enters the obstacle center.
- The molten fluid flow turbulence is reduced by increasing the melt height in the tundish.
- Analysis of the input flow into the tundish indicates that the input flow has a maximum and minimum effect on the middle and side regions of the tundish, respectively.
- The average flow velocity on the top surface of the melt is decreased by %3 by increasing the melt height from 0.5 to 0.75 meters.
- Since the heat transfer and loss are highly dependent on the velocity of the molten fluid flow, increasing the melt height leads to a more laminar fluid flow inside the tundish and thus the heat loss and temperature gradient inside the tundish are reduced.
- Tundish with a higher melt height has more static melt areas which negatively influence the amount of particle absorption.

## Acknowledgments

This research was accomplished with the support of SKS. Special thanks to the generous help of R&D and the steel-making unit of SKS; the authors would like to gratefully appreciate H. Soltani, T. Adhami, and S. Lak for their help in this study.

## Reference

[1] S. Louhenkilpi, Continuous casting of steel, Elsevier, 2014. https://doi.org/10.1016/B978-0-08-096988-6.00007-9.

[2] S. Yang, L. Zhang, J. Li, K, Structure optimization of horizontal continuous casting tundishes using mathematical modeling and water modeling. ISIJ international. 49 (2009) 1551-1560. https://doi.org/10.2355/isijinternational.49.155.

[3] X. Zhou, Z. Tang, G. Qu, Thermal stress and thermal fatigue analysis of the continuous casting tundish cover. Materials Science and Engineering: A. 527 (2010) 2327-2334. https://doi.org/10.1016/j.msea.2009.11.068.

[4] Z. Li, M. Zhang, F. Zhou, Y. Lu, X. Zhang, H. Gu, 2022. Numerical simulation of slag entrapment process during the end of casting in tundish, Ironmaking & Steelmaking. (2022) 1-9. https://doi.org/10.1080/03019233.2022.2078261.

[5] M.R. Mosalman Yazdi, A.R. Faghih Khorasani, S. Talebi, Physical modeling of melt flow in steel continuous casting tundish, Modares Mechanical Engineering. 17 (2017) 385-392 (in Persian). https://dorl.net/dor/20.1001.1.10275940.1396.17.6.25.5.

[6] J.G. Liu, H.C. Yan, L.I.U. Liu, X.H. Wang, Water

modeling of optimizing tundish flow field, Journal of iron and steel research International. 14 (2007) 13-19. https://doi.org/10.1016/S1006-706X(07)60036-3.

[7] A. Kumar, D. Mazumdar, S.C. Koria, Modeling of fluid flow and residence time distribution in a four-strand tundish for enhancing inclusion removal, ISIJ international. 48 (2008) 38-47. https://doi.org/10.2355/isijinternational.48.38.

[8] Y. Miki, B.G. Thomas, Modeling of inclusion removal in a tundish, Metallurgical and materials transactions B. 30 (1999) 639-654. https://doi.org/10.1007/s11663-999-0025-6.

[9] J.R. de Sousa Rocha, E.E.B. de Souza, F. Marcondes, J.A. de Castro, Modeling and computational simulation of fluid flow, heat transfer and inclusions trajectories in a tundish of a steel continuous casting machine, Journal of Materials Research and Technology. 8 (2019) 4209-4220. https://doi.org/10.1016/j.jmrt.2019.07.029.

[10] S.G. Zheng, M.Y. Zhu, Y.L. Zhou, W. Su, Flow characteristics and inclusion removal in a ten-strand continuous casting tundish: Physical Modelling and Industrial Trials, Journal of Iron and Steel Research International. 23 (2016) 92-97. https://doi.org/10.1016/S1006-706X(16)30018-8.

[11] L. Zhang, S. Taniguchi, K. Cai, Fluid flow and inclusion removal in continuous casting tundish, Metallurgical and Materials Transactions B. 31 (2000) 253-266. https://doi.org/10.1007/s11663-000-0044-9.

[12] P.K. Jha, P.S. Rao, A. Dewan, Effect of height and position of dams on inclusion removal in a six strand tundish, ISIJ international. 48 (2008) 154-160. https://doi.org/10.2355/isijinternational.48.154.

[13] C.M. Fan, R.J. Shie, W.S. Hwang, Studies by mathematical and physical modelling of fluid flow and inclusion removal phenomena in slab tundish for casting stainless steel using various flow control device designs, Ironmaking & Steelmaking. 30 (2003) 341-347. https://doi.org/10.1179/030192303225004015.

[14] H.H. Zhu, M. Wang, C. Yao, Z.L. Wang, X.L. Wang, Y.P. Bao, Influence of non-iso-velocity casting on flow-field index of a 41-ton six-strand tundish by physical and numerical modeling, Journal of Iron and Steel Research International. (2022) 1-13. https://doi.org/10.1007/s42243-022-00821-4.

[15] Z.Y. Xin, H.N. Cui, T. Li, G.Z. Tang, Y.L. Zhu, J.C. Yan, J.G. Li, Numerical Simulation of Inclusion Removal by Bubble Injection in the Submerged Nozzle With Swirling Flow, Metallurgical and Materials Transactions B. (2022) 1-17. https://doi.org/10.1007/s11663-022-02552-z.

[16] J. Lu, S. Li, Z. Luo, Z. Zou, L. Shao, Numerical simulation of collision removal of inclusion in swirling flow tundish, International Journal of Chemical Reactor Engineering. (2022). https://doi.org/10.1515/ijcre-2021-0300.

[17] T. Merder, J. Pieprzyca, M. Warzecha, P. Warzecha, A. Hutny, Evolution of the Numerical Model Describing the Distribution of Non-Metallic Inclusions in the Tundish, Materials. 14 (2021) 2229. https://doi.org/10.3390/ma14092229.

[18] J. Liu, P. Zhou, X. Zuo, D. Wu, D. Wu, Optimization of the Liquid Steel Flow Behavior in the Tundish through Water Model Experiment, Numerical Simulation and Industrial Trial, Metals. 12 (2022) 1480. https://doi.org/10.3390/met12091480.

[19] O.S. Delgado Ramirez, E. Torres-Alonso, J.Á. Ramos Banderas, S.A. Arreola Villa, C.A. Hernández Bocanegra, J.S. Téllez Martínez, Thermal and Fluid-Dynamic Optimization of a Five Strand Asymmetric Delta Shaped Billet Caster Tundish, Steel research international. 89 (2018) 1700428. https://doi.org/10.1002/srin.201700428.

[20] O. Minin, I. Minin, Computational Fluid Dynamics Technologies and Applications. BoD–Books on Demand, 2011. https://doi.org/10.5772/686.

# Experimental Study of Mechanical Properties and Hardness in Gas Metal Arc Welding on SUH 310S Steel Using Response Surface Methodology

**A. R. Aghaeifar** *[1]

*Department of civil Engineering, Payame Noor University, Tehran, Iran*

## Abstract

Due to technological advances and the growing need to repair parts at low cost, the gas metal arc welding (GMAW) method has become increasingly popular among industrialists. The response surface methodology (RSM) and model validity were measured with standard statistical measures. In this research, the input parameters including; welding speed (mm/min), voltage (V), and wire feed rate (cm/min), have been selected as input parameters. Mini-tab software was utilized to carry out modeling and optimization using RSM. On heat resistance steel (SUH 310S) using the RSM method, 17 experimental experiments were designed with three center points. According to the signal-to-noise ratio (S/N), the effective parameters of mechanical properties and hardness are wire feed rate, voltage, and welding speed, respectively. The results showed that the analysis of variance (ANOVA) with the desirability model obtained 0.953. Optimum levels for each input variable were analyzed in terms of mechanical properties and welding hardness. Finally, the optimum levels obtained are welding speed of 250 mm/min, wire feed rate of 210 cm/min, and voltage of 17 volts.

*Keywords:* Gas Metal Arc Welding, Response surface methodology, SUH 310S steel, Mechanical properties, Optimization.

## 1. Introduction

Among many austenitic stainless steel materials, because SUH 310S stainless steel sheet has higher chromium and nickel content than ordinary 18-8 austenitic SUH 310S, its heat resistance and corrosion resistance are relatively better, and it can be used at temperatures as high as 1090 °C [1,2]. SUH 310S continuous used at high temperature [3]. SUH 310S plate should be forged at a temperature of about 1175 °C, and the forging temperature should not be lower than 980 °C [4,5]. After forging, rapid air cooling or direct water quenching of small forgings is required [6]. For optimum corrosion resistance, it should also be annealed after forging [7]. SUH 310S sheet can be used to produce furnace components, furnace plates, high temperature vessels and welding wire [8,9]. The material can also be used further in many applications by taking advantage of its thermal properties.

Gas metal arc welding (GMAW) is one of the welding methods in the industry, such as special structures of Power stations [10]. High flexibility, possibility of welding in different thicknesses, increased production capability and possibility of automatic implementation of reasons distinguish this method from other welding methods [11]. This process is widely used in various industries, including pipelines, petrochemicals, buildings, automobiles, and ships [12]. In this process, the continuity of the consumed electrode, welding discontinuity, lack of slag, and low thermal hazard in the base metal are considered the advantages of this method, in which the continuity of the consumed electrode is an essential advantage that increases the productivity

---

**Corresponding author*
*Email: alireza.aghaeifar@pnu.ac.ir*
*Address: Department of civil Engineering, Payame Noor University, Tehran, Iran*
*1. Scientific staff trainer*

rate [13]. In large industries, the cost is high, and this factor is entirely dependent on the determination of the welding variables in the welding process with gas protection and the equation between the existing parameters and how to achieve the desired state [14,15]. Among all techniques, one common method is GMAW welding with neutral gas [16].

J. Vora et al. [17] studied the wire arc additive manufacturing (WAAM) method based on GMAW welding to fabricate multilayer structures with optimized process parameters on SS316L using SS316L metal wires. The microstructure, macrostructure, and mechanical properties (tensile test, impact test, microhardness, and fractography) of the multilayer structure were examined. The results of all tensile properties of high, medium, and low surface tests developed by the WAAM process are within the range of SS 316L values. The UTS, YS, and elongation of the used SS316L were 485 MPa, 220 MPa, and 45%, respectively. The average number of specimens of UTS, the upper, middle, and lower zone and height of YS were 512.53 MPa, 256.57 MPa and 49.35%, respectively. Therefore, it can be concluded that the experimentally measured UTS, YS, and elongation of the WAAM process developed parts are within the limits of the SS 316L grade values used. Chen et al. [18] studied the fabrication of SS316L alloys by the GMAW process. The main objective of this study was to determine the effect of heat treatment on strength and corrosion behavior. The results showed that high temperature and time of treatment heat caused SS 316L to deteriorate. The ultimate tensile strength and yield strength were changed by the heat treatment carried out at 1000 °C. Also, the maximum strength of the AM components was found to be similar to SS 316L. Ahsan et al. [19] have developed a bimetallic additively manufactured structure of SS 316 L, and low alloy carbon steel to produce a WAAM structure of two different materials using the GMAW process. Two separate layers of low-carbon and stainless steel were shown on the welded area in the microstructure definition, and no defect was seen in the specified area. In the microhardness test, the hardness value was more significant in the stainless steel region due to Cr. However, the hardness value was observed at the lower part of the low-carbon steel. So the standard design failed from that point of view and that part of the carbon steel had less strength. Another study by Ji et al. [20] used the WAAM process to fabricate SS 304L. He studied mechanical properties through complex testing and micro-structures through metallographic research. The result is that when the components are placed in another place, the temperature increases, the dendrite's thickness increases, and the microstructure remains the same. In the presence of dendrites, the stiffness will be different in the vertical and horizontal directions, which will affect the mechanical properties. Their findings revealed that the presence of dendrites changed the strength of the boundary between longitudinal and lateral pathways. This resulted in anisotropy of mechanical properties.

In the present study, wire feed rate, welding speed, and voltage have been considered as effective input parameters of the process and according to the necessities of research, the parameters of mechanical properties and hardness are output parameters. RSM modeling was used to establish the interaction between process input and output parameters. The purpose of this research is to model the output parameters based on the input parameters and also to optimize the mechanical properties and hardness. Finally, the optimized part is examined regarding hardness and mechanical properties.

## 2. Materials and methods

The purpose of this research is to optimization mechanical properties and hardness to investigate the influence of effective parameters in neutral gas welding. For this purpose, as shown in Fig. 1, GMAW process devices Including the carry MIG 501 wire feed system and FP4M machine were used. Referring to the above, in this research, 17 experiments were carried out on heat resistance steel (SUH 310S) with 10×30×50 mm$^3$, as the base metal in GMAW welding. Failure to control the consumable electrode on the workpiece will lead to deviation from the welding center or false joining of the welding point. The reason for using the milling machine is to move in the direction of the X, Y, and Z-axis and to automate the GMAW process. The SUH 310S (base metal) and stainless steel 743 (wire electrode) chemical composition and mechanical properties are shown in Tables 1 and 2. Due to the use of GMAW welding, the feeding wire electrode is a consumable material in the form of welding electrodes the material is stainless steel 743, the diameter of the electrodes is 1 mm and produced by AMA company. Carbon dioxide ($CO_2$) gas was used as a shielding gas.

Table 1. Chemical composition of SUH 310S steel.

| Metal | Fe | C | Mn | P | Si | Cr | Ni | Cu |
|---|---|---|---|---|---|---|---|---|
| SUH 310S steel | Bal | 0.10 | 2.00 | 0.05 | 2.50 | 25.00 | 21.00 | -- |
| Stainless steel SS743 | Bal | 0.03 | 1.50 | 0.01 | 0.65 | 21.00 | 12.00 | 0.70 |

Table 2. Mechanical properties of SUH 310S steel.

| Mechanical properties | UTS | YS | Elongation | Hardness |
|---|---|---|---|---|
| Unit | (MPa) | (MPa) | (%) | (HB) |
| Value | 524 | 217 | 40 | 225 |

Fig. 1. GMAW process devices.

In this research, the input parameters including welding speed (mm/min), voltage (V), and wire feed rate (cm/min) have been selected as input parameters. Mini-tab software was utilized to carry out modeling and optimization using RSM. On heat resistance steel (SUH 310S) using the RSM method, 17 experimental experiments were designed with three center points. Properties sample welding that was measured directly from the tensile test. A standard tensile test was performed to evaluate the mechanical properties of the optimized part. In this test, sample is prepared according to the ASTM-E8 standard. It should be noted that the test was performed at room temperature at a speed of 10 mm/min.

## 3. Response Surface Methodology

The design of experiments (DoE) is a scientific solution that provides targeted changes to the factors affecting a process or product and then examines the resulting changes in output, which provide extensive information and understanding of the process, development, and how these factors affect the response. In designing an experiment, the first step is to determine the response variables. Then the parameters affecting the problem must be identified and the variable levels must be determined. Then, according to the parameters and levels considered for each parameter, experiments were performed. In this research, the aim is to the effect of material and process parameters on the mechanical properties and hardness of welded samples using the GMAW process. One of the essential mechanical properties can be mentioned tensile strength, which determines the amount of tolerable stress by the part under tensile loads, which is considered the response variable. The structure of boiling points of samples produced in different process conditions was also investigated. After identifying the response variables and parameters affecting the problem, the next step is determining the number of levels studied for the parameters and their range. According to the studies, the usual welding speeds of 200, 300, and 400 mm/min, the voltage of 17, 27, and 32 volts, and wire feed rates of 210, 231, and 253 cm/min were selected. The purpose of choosing the minimum welding speed, equal to 200 mm/min, was that the possibility of performing a welding process lower than this speed in the method used was impossible and a connection between the electrode and sample was not accepted. Also, the reason for choosing the welding speed of 400 mm/min as the maximum welding speed was the limitation of the machine used for welding. Therefore, it is necessary to use a suitable test design to reduce the number of tests. In this research, wire feeding speed (electrode), welding voltage, and welding speed as effective input parameters have been placed on the welding cross-section. The data and intervals of each process variable can be seen in Table 3. The experiments were performed in the same laboratory conditions based on RSM with different parameters. The DoE methods such as the RSM method are an effective way to reduce the number of experiments. The parameters and levels tested for each parameter in the present study are in Table 4. The experiments of the said research were designed as a table using the Minitab software.

Table 3. Input parameters of GMAWed process.

| GMAW parameter | Voltage (V) | | | Wire feed rate (cm/min) | | | Welding speed (mm/min) | | |
|---|---|---|---|---|---|---|---|---|---|
| Unit | low | medium | high | low | medium | high | low | medium | high |
| Code | -1 | 0 | +1 | -1 | 0 | +1 | -1 | 0 | +1 |
| Range | 17 | 27 | 32 | 210 | 231 | 253 | 200 | 300 | 400 |

Table 4. Input and output parameter.

| | Coded | | | Actual values | | | Responses | |
|---|---|---|---|---|---|---|---|---|
| No. | Welding speed | Voltage | Wire feed rate | Welding speed | Voltage | Wire feed rate | Mechanical properties | Hardness |
| #1 | 1 | -1 | 1 | 400 | 17 | 253 | 674 | 88 |
| #2 | 0 | 0 | 0 | 300 | 27 | 231 | 643 | 85 |
| #3 | -1 | -1 | -1 | 200 | 17 | 210 | 611 | 86 |
| #4 | 0 | 0 | 1 | 300 | 27 | 253 | 635 | 85 |
| #5 | -1 | 1 | -1 | 200 | 32 | 210 | 655 | 89 |
| #6 | -1 | 1 | 1 | 200 | 32 | 253 | 639 | 86 |
| #7 | 0 | 0 | 0 | 300 | 27 | 231 | 643 | 85 |
| #8 | -1 | 0 | 0 | 200 | 27 | 231 | 623 | 83 |
| #9 | 1 | 0 | 0 | 400 | 27 | 231 | 634 | 86 |
| #10 | 0 | 1 | 0 | 300 | 32 | 231 | 655 | 87 |
| #11 | 1 | 1 | 1 | 400 | 32 | 253 | 623 | 86 |
| #12 | 1 | 1 | -1 | 400 | 32 | 210 | 641 | 89 |
| #13 | 0 | 0 | -1 | 300 | 27 | 210 | 678 | 91 |
| #14 | 1 | -1 | -1 | 400 | 17 | 210 | 612 | 84 |
| #15 | 0 | -1 | 0 | 300 | 17 | 231 | 594 | 82 |
| #16 | -1 | -1 | 1 | 200 | 17 | 253 | 612 | 87 |
| #17 | 0 | 0 | 0 | 300 | 27 | 231 | 643 | 85 |

The RSM approach is a method to determine the interaction between different process parameters with varying criteria of welding and investigate the effect of these process parameters on related responses. RSM is a set of mathematical and statistical techniques that are useful for modeling and analyzing problems in which the desired answers are affected by several variables. The RSM method is a strategy for building experimental and optimization models. By performing experiments and using regression analysis, a response model to some independent input variables is obtained. In the surface response method, independent parameters can be shown based on Eq 1.

$$y = f[x_1.x_2.x_3 \dots\dots\dots x_n] \qquad \text{Eq. (1)}$$

When Y is the answer, F is the function's answer, X is an experimental error, and $X_1$, $X_2$, …., $X_n$ are independent parameters. By plotting the expected response Y, a level known as the RSM is obtained. The shape of the F function is unknown and can be very complex. Therefore, the RSM method intends to compare the F-value with a lower-order polynomial in some independent process variables. If the response is well modeled by a linear function of the independent variable, Eq 1 can be equated with Eq 2:

$$y = \beta_0 + \beta_1 x_1 + \beta_2 x_2 + \beta_3 x_3 + \cdots \dots\dots + \beta_n x_n \qquad \text{Eq. (2)}$$

However, if a curvature appears in the system, higher-order polynomials, such as the Quadratic equation model can be used according to Eq 3:

Eq. (3)

$$y = \beta_0 + \sum_{i=1}^{k} \beta_i x_i + \sum\sum_{i<j} \beta_{ij} x_i x_j + \sum_{i=1}^{k} \beta_{ii} {x_i}^2 + \varepsilon$$

Regression analysis is performed when the dependent set related to the experimental orientations is collected. Then, an appropriate statistical analysis such as ANOVA analysis, is performed to identify the effects of factors on dependents as well as the interactions between factors. Then, the developed model is justified by a validation test.

## 4. Results and discussion

### 4.1. Tensile test

Improving mechanical properties has always been one of the most important challenges. In this research, the tensile test at room temperature was used to check the mechanical properties. Fig 2 shows the tensile test sample after the GMAWed process in SUH 310S Steel. The tensile test of the samples showed that all the samples behave close to each other in the tensile stress. This same behavior shows the significant potential of the base metal. The range of low changes in tensile stress indicates the quality of welding, the compatibility of the used electrode with the BM, and the low residual stress of the welding site. After the tensile test, the prepared test samples were all broken from the base metal or HAZ area and based on the results, the fracture occurred in a part of the triple HAZ area, which has the lowest strength due to the grain size.

Fig. 2. Tensile test samples.

## 4.2. Responses optimization of RSM mothed

The data output was obtained by entering the results of the tensile test in Minitab software and analyzing it by the Ryan-Joyner method. The P-value in the obtained diagram is greater than the risk probability value of 0.05. It's concluded that the results related to the tensile strength of the welded sample follow the normal distribution. Due to the normal distribution of the data, the ANOVA of the data obtained from the tensile test is checked. One of the essential topics in analyzing the results of experimental tests is to study the interaction effects of parameters on the response variable. The two-parameter interactions that had the most significant effect on the tensile strength of welded sample have been investigated from the S/N table. The deal of tensile strength has increased with increasing speed welding. This is due to the decrease in melt strength, which increases the adhesion and improves the weld strength. The obtained interactions for modeling and predicting the outputs of the welding process are shown in Eqs 4 and 5.

Eq. (4)

Mechanical properties = 643.18 + 3.77 welding speed + 11.10 voltage - 3.17 wire feed rate - 5.73 welding speed*welding speed - 7.15 voltage*voltage + 4.17 wire feed rate*wire feed rate - 11.62 welding speed*voltage + 7.38 welding speed*wire feed rate - 12.13 voltage*wire feed rate

Eq. (5)

Hardness = 84.925 + 0.296 welding speed + 0.982 voltage - 0.812 wire feed rate + 0.083 welding speed*welding speed + 0.083 voltage*voltage + 1.320 wire feed rate*wire feed rate + 0.125 welding speed*voltage + 0.375 welding speed*wire feed rate - 1.375 voltage* wire feed rate

ANOVA was used to check the accuracy of the obtained modeling interactions. If the obtained P-value is less than 0.05, the accepted model has 95% confidence. Tables 5 and 6 show the results of ANOVA of the proposed models.

Due to the appropriateness of the modeling equations, the interaction of the input parameters with the output parameters is reported separately below. Fig 3 shows the 3D surface plot of the wire speed and voltage parameters related to the mechanical properties. By increasing the voltage and wire feed rate, the width of the mechanical properties increases. The modeling results performed in Minitab software were reviewed separately in this section.

Table 5. ANOVA for the mechanical properties model.

| Source | DF | Adj SS | Adj MS | F-Value | P-Value |
|---|---|---|---|---|---|
| Model | 9 | 6101.92 | 677.99 | 2.51 | 0.019 |
| Linear | 3 | 2014.22 | 671.41 | 2.48 | 0.025 |
| welding speed | 1 | 194.20 | 194.20 | 0.72 | 0.025 |
| voltage | 1 | 1682.62 | 1682.62 | 6.22 | 0.041 |
| wire feed rate | 1 | 137.39 | 137.39 | 0.51 | 0.099 |
| Square | 3 | 1395.33 | 465.11 | 1.72 | 0.049 |
| welding speed * welding speed | 1 | 370.49 | 370.49 | 1.37 | 0.080 |
| voltage * voltage | 1 | 575.84 | 575.84 | 2.13 | 0.088 |
| wire feed rate * wire feed rate | 1 | 195.73 | 195.73 | 0.72 | 0.023 |
| 2-Way Interaction | 3 | 2692.37 | 897.46 | 3.32 | 0.087 |
| welding speed * voltage | 1 | 1081.13 | 1081.13 | 4.00 | 0.086 |
| welding speed * wire feed rate | 1 | 435.13 | 435.13 | 1.61 | 0.045 |
| voltage * wire feed rate | 1 | 1176.12 | 1176.12 | 4.35 | 0.075 |
| Error | 7 | 1892.55 | 270.36 | 3.55 | 0.634 |
| Lack-of-Fit | 5 | 1892.55 | 378.51 | 3.24 | |
| Pure Error | 2 | 1873.32 | 412.11 | | |
| Total | 16 | 7994.47 | | | |
| | | $R^2 = 0.89$ | $R^2_{adj} = 0.81$ | $R^2_{predict} = 0.93$ | |

Table 6. ANOVA for hardness model.

| Source | DF | Adj SS | Adj MS | F-Value | P-Value |
|---|---|---|---|---|---|
| Model | 9 | 61.2878 | 6.8098 | 2.33 | 0.039 |
| Linear | 3 | 23.3707 | 7.7902 | 2.66 | 0.029 |
| welding speed | 1 | 1.1983 | 1.1983 | 0.41 | 0.043 |
| voltage | 1 | 13.1656 | 13.1656 | 4.50 | 0.072 |
| wire feed rate | 1 | 9.0068 | 9.0068 | 3.08 | 0.023 |
| Square | 3 | 21.5421 | 7.1807 | 2.45 | 0.048 |
| welding speed * welding speed | 1 | 0.0767 | 0.0767 | 0.03 | 0.076 |
| voltage * voltage | 1 | 0.0767 | 0.0767 | 0.03 | 0.076 |
| wire feed rate * wire feed rate | 1 | 19.6410 | 19.6410 | 1.71 | 0.036 |
| 2-Way Interaction | 3 | 16.3750 | 5.4583 | 1.87 | 0.024 |
| welding speed * voltage | 1 | 0.1250 | 0.1250 | 0.04 | 0.051 |
| welding speed * wire feed rate | 1 | 1.1250 | 1.1250 | 0.38 | 0.055 |
| voltage * wire feed rate | 1 | 15.1250 | 15.1250 | 1.17 | 0.057 |
| Error | 7 | 20.4770 | 2.9253 | 1.11 | 0.636 |
| Lack-of-Fit | 5 | 20.4770 | 4.0954 | 1.37 | |
| Pure Error | 2 | 21.3281 | 4.9917 | | |
| Total | 16 | 81.7647 | | | |

$R^2 = 0.88$ $R^2_{adj} = 0.92$ $R^2_{predict} = 0.98$

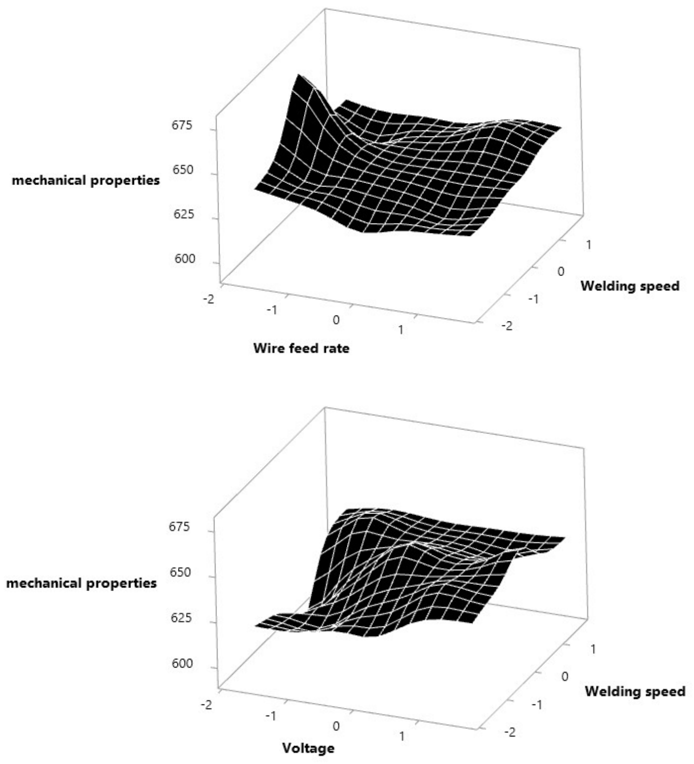

Fig. 3. 3D surface plot for mechanical properties.

The interactions mean of mechanical properties in Fig 4 show that the three primary parameters in the DoE are chosen correctly and they affect each other a lot. The results shown in each parameters are as follows: welding speed and voltage have an extreme point, but the opposite has been done in the wire feeding rate.

For better grain growth and optimal bonding, the maximum weld penetration depth in the SUH 310S steel is required. Therefore, the interaction of three-factors on the mechanical properties and hardness was investigated. Fig 5 shows the 3D plots of the objective response to different variables. The experimental results show that the three design variables have a significant impact on actual performance. As shown in Fig 5, when mechanical properties are constant, the objective function voltage first decreases and then increases with the increase of voltage and wire feed rate.

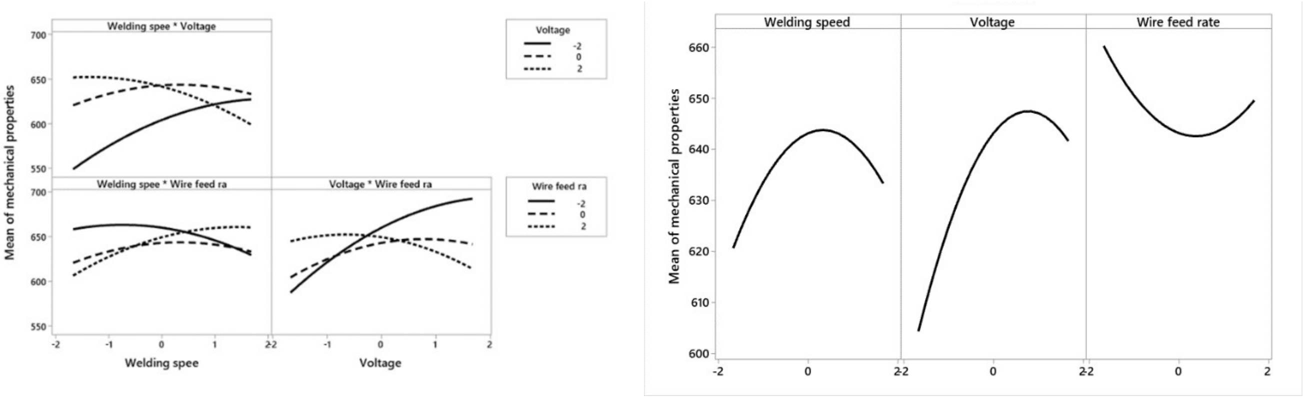

Fig. 4. Results mean of mechanical properties of optimization in RSM method.

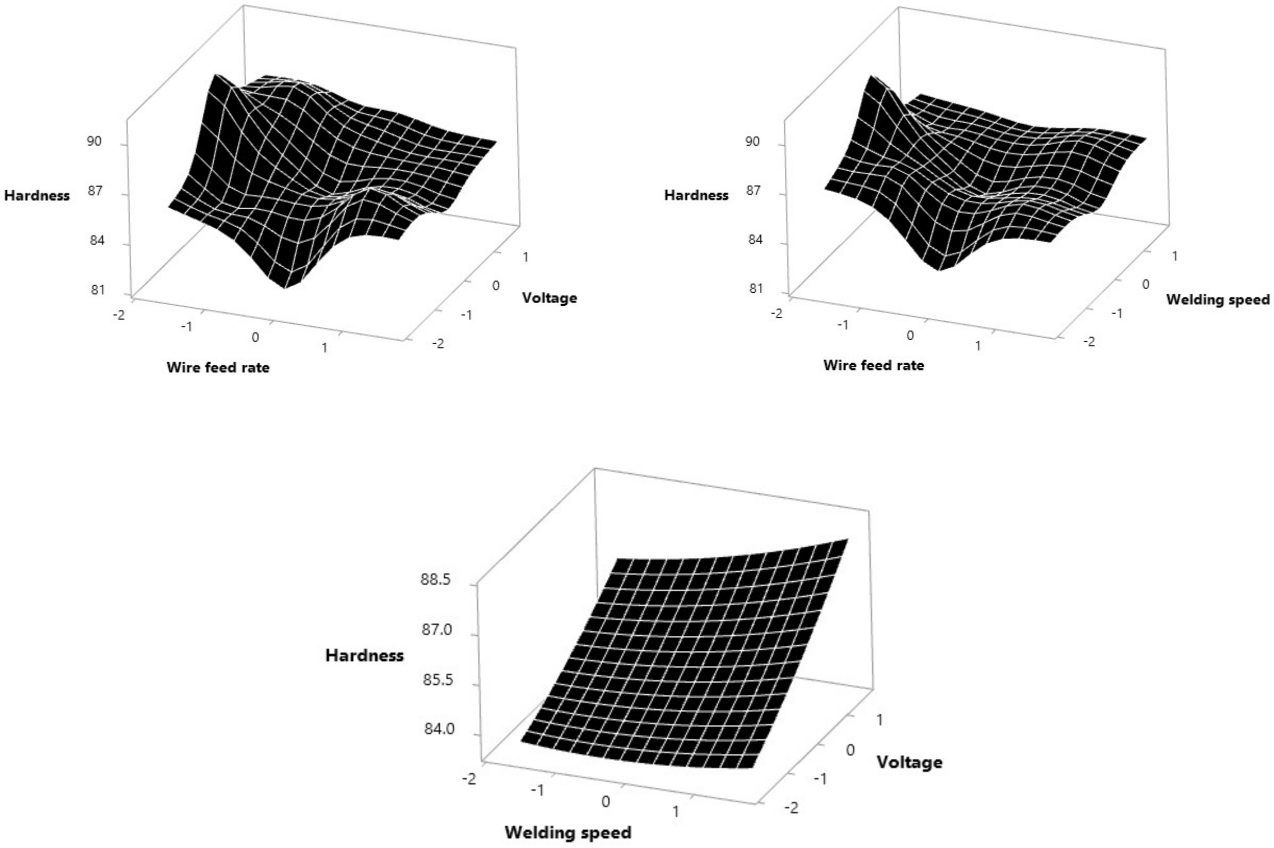

Fig. 5. 3D surface plot for hardness.

The interactions mean of hardness in Fig 6 shows that the three main parameters in the DoE are chosen correctly and they affect each other a lot. The results shown in each parameters are as follows: welding speed and voltage have a linear effect.

In this research, in addition to modeling the output parameters, optimization of the parameters of voltage, welding speed and wire feed rate concerning max model the mechanical properties and hardness with the Minitab software and RSM method are obtained. Table 7 shows the results of optimizing the input parameters. Voltage values of 17 volts, wire feed rate of 210 cm/min and welding speed of 250 mm/min. The desirability model value of 0.953 optimization result. The error rate is reported to be less than 0.1% and indicates that the optimization parameters are acceptable.

## 5. Conclusions

In this research, mechanical properties and hardness were investigated according to the parameters of the gas metal arc welding (GMAW) process. Input parameters including; voltage, welding speed, and wire feeding rate are modeled using response surface methodology (RSM) methods and the model's accuracy is measured by standard statistical measures.

- According to the P-value value in the analysis of variance (S/N) tables, we find that modeling by the RSM method has desirability.
- According to the validation test of the optimization, we find that the optimization has a level of reliability response.
- ANOVA results for the mechanical properties model are: $R^2 = 0.89$, $R^2$ (adj) = 0.81, and $R^2$ (predict) = 0.93, respectively.
- ANOVA results for the hardness model are: $R^2 = 0.88$, $R^2$ (adj) = 0.92, and $R^2$ (predict) = 0.98, respectively.
- The results of optimizing the input parameters are voltage values of 17 volts, wire feed rate of 210 cm/min, and welding speed of 250 mm/min. The desirability model is equal to 0.953.

## 6. Acknowledgments

The authors are very much thankful to the unknown reviewers for their valuable and constructive suggestions which improved the readability of the paper.

## 7. Conflict of Interest

The authors declared no potential conflicts of interest for the research, authorship, and publication of this article.

## 8. Funding

The authors received no financial support for the research, authorship, and publication of this article.

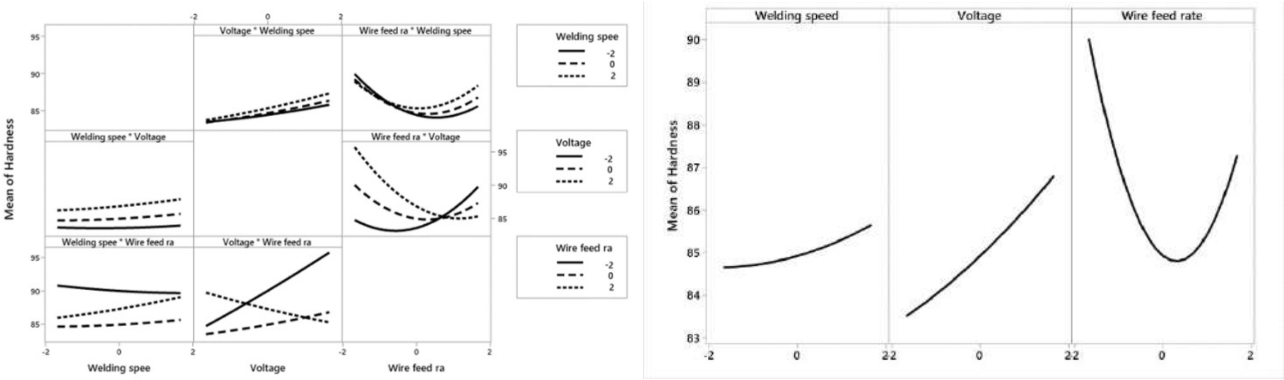

Fig. 6. Results mean of hardness of optimization in RSM method.

Table 7. Optimization of influential factors with the accuracy of the proposed model.

| | Welding speed | Voltage | Wire feed rate | Mechanical properties | Hardness |
|---|---|---|---|---|---|
| Importance | ***** | *** | * | *** | *** |
| Real-Predict | 250 | 17 | 210 | 676.331 | 88.9902 |

## References

[1] J. Liu, Y. Tan, E. Jiang, B. Gong, Y. Zhao, Y. Wang, Y. Lu: Mater corr., 70(2018), 871.

[2] Y. Zhong, C. Zhou, S. Chen, R. Wang: Chin Jour Mech Eng., 30(2017), 204.

[3] J.H. Lee, S. Yamashita, T. Ogura, K. Saida: Jour of ad join pro., 3(2021), 100044.

[4] K. Kadoi, A. Fujinaga, M. Yamamoto, K. Shinozaki: Weld World., 57(2013), 383.

[5] A. Mortezaie, M. Shamanian: Int Jour Pres Ves Pip., 116(2014), 37.

[6] Y. Zhong, C. Zhou, S. Chen, R. Wang: Chin Jour Mech Eng Engl., 30(2017), 200.

[7] X.K. Lian, Y. Li, Y. Xiong, Y.L. Wu, S. Han, T.T. He, C.X. Wang, F.Z. Ren: Jour Iron Steel Res Int., 39(2022).

[8] Y.Z. Zhang, J.J. Wang, N.R. Tao: Jour Mater Sci Technol., 36(2020), 67.

[9] A. Amininejad, R. Jamaati, S.J. Hosseinipour: Trans Ind Inst Metals., 74(2021), 1799.

[10] G. Li, B. Jiang, H. Liu, L. Ning, D. Yi, X. Wang, Z. Liu: Pro in Org Coat., 137(2019), 105315.

[11] Y. Peng, L. Yu, Y. Liu, Z. Ma, H. Li, C. Liu, J. Wu: Mater Sci Eng: A., 767(2019), 138419.

[12] R. Zong, J. Chen, C. Wu: Jour of Mater Pro Tech., 285(2020), 116781.

[13] Y. Han, J. Tong, H. Hong, Z. Sun: The Inter Jour of Ad Manu Tech., 101(2019), 992.

[14] B. Wu, Z. Qiu, Z. Pan, K. Carpenter, T. Wang, D. Ding, S.V. Duin, H. Li: Jour Mat Sci Tech., 52(2020), 231.

[15] C. Chen, S. Lin, C. Fan, C. Yang, L. Zhou: The Inter Jour of Ad Manu Tech., 97(2018), 3622.

[16] T. Xiang, H. Li, Y. Geo, S.Y. Zhao, L.Y. Lou, H. Wang: The Inter Jour of Ad Manu Tech., 102(2019), 862.

[17] J. Vora, H. Parmar, R. Chaudhari, S. Khanna, M. Doshi, V. Patel: Jour Mat Res Tech., 20(2022), 2751.

[18] X. Xhen, J. Li, X. Cheng, H. Wang, Z. Huang: Mater Sci Eng, A., 715(2018), 312.

[19] M.R.U. Ahsan, A.N.M. Tanvir, T. Ross, A. Elsawy, M.-S. Oh, D.B. Kim: Rapid prototype J., 26(2020), 528.

[20] L. Ji, J. Lu, C. Liu, C. Jing, H. Fan, S. Ma (Eds.): MATEC Web of Conferences., 2017.

# Failure Modes Analysis System in Casting Parts by PFMEA Method

**K. Boroumand *[1], T. Khanali [2], A. Meshkinfar [3]**

[1, 3] *Isfahan, Sejzi Industrial Zone, Ghaltak Sazan Sepahan, Research and Development Department*
[2] *Isfahan, Sejzi Industrial Zone, Ghaltak Sazan Sepahan, Human Resources Department*

## Abstract

Improving the level of quality of products and services provided by companies is the first and main factor of development to get a major market share. In this regard, the failure mode and effects analysis are an effective method to improve the quality and reduce waste in products. To eliminate the existing defects, especially melt run out from the casting molds, the analysis of potential failure modes by multiplication of three numbers 1-intensity2- occurrence and 3- detect probablity was estimated. The results of the study showed that to reduce the melt run out defect, the most important potential for failure is the lack of skills and experience of personnel in assembly, inadequate quality of raw materials, non-compliance with continuous molding process with a risk priority number of 300,400,450, respectively. Continuous training, preparation of a checklist for input items and controlling the molding continuity reduced waste run outs defect by 70%.

*Keywords:* Failure Effects, Melting Run Out, PFMEA.

## 1. Introduction

Failure mode and effects analysis (FMEA) is an engineering technique which is widely used to design, identify, classify, analyze potential or known problems and failures in a system, process, or service before it reaches the customer; It provides a framework for analyzing the cause and effect of potential product failures [1]. The purpose of FMEA in a process or product is to prevent the failure before the mass production to identify the potential defects in the process. FMEA reduces the costs by optimizing processes, continual improvement and corrective and preventive action [2]. Efforts to prevent failures during the production and development of products and processes, as well as failures prediction and finding the least costly way to prevent failures are the main goals of using this method. In other words, FMEA is a process failure analysis method that tries to maximize the potential hazards in the area where the production process takes place and scores it based on a specific mechanism [2].

The results of the research conducted by the Fraunhofer Institute in 2011, which surveyed 180 manufacturing companies, show that FMEA is a method which often used in these companies. In this survey, 60.3 percent of the companies use the common FMEA method, and 52.5 percent of the risks are assessed in workshops and team meetings. Also, the methods of Design Review Based on Failure Mode (DRBFM) (9.5 percent) and Failure Tree Analysis (FTA) (7.3 percent) have been used less in risk analysis [4].

In FMEA, the goal is failure mode and analysis of its effects on products and processes during the initial stages of development in the case of potential failure and initiation of measures to prevent failure through integrated risk analysis. As a result, FMEA reduces development time and costs, while the increase in quality will result in the reduction of product defects; Therefore, FMEA is a

---

**Corresponding author*
*Email: khalilboroumand@gmail.com*
*Address: Isfahan, Sejzi Industrial Zone, Ghaltak Sazan Sepahan*
*1. M. Sc*
*2. PhD*
*3. M. Sc*

valuable tool for risk management. Common arguments against FMEA are the high costs of implementation, the impact of mental perceptions and the difficult interpretation of the number of risk priority number (RPN), which will not be considered as an absolute level for risk. Also, it is not possible to determine the financial risk based on the priority number of risks; Therefore, the only application of FMEA is a quantitative determination of risk objectives and is not a solution to eliminate the causes of failure; But it allows the systematic and organized collection of explicit and implicit knowledge about the probability of failure. In the framework of FMEA, the risk analysis begins from the partial system stage and a list of ordered failure cases and the effect of those failure cases is analyzed by calculating an index called the RPN. Also, this method has been used in the field of project management, and finally, the use of this method has led to the reduction of project costs [4,5].

In this regard, one of the process defects with high reproducibility was selected and its causes were studied by the above method.

## 2. Method

Many studies have been done to analyze the modes and effects of failure. According to the FMEA topics, the aim of the research was to analyze the failure modes and effects in the production process which was the melt run out, in different parts of the assembled mold being melted in all cast parts with tonnage above five tons and by static casting method.

The flow of melt from the inside of the mold to the outside, during pouring is defined as the melt run out. According to the variety of molds and the different molding processes and the type of related equipment and assembly tools, different places for melt run out can be predicted. Therefore, in the following, different molding process with different molding methods will be examined in regard of the location of the run out defect (Figure 1).

There is a possibility of melt run out in an ingot mold assembly with quadrangular machined grooves, where the ceramic gating system is embedded inside the grooves, from 5 locations:

A- From below the base plate (A).
B-from the gap between base plate and the ingot mold (B).
C- from the gap of the in ingot mold that is usually one peice ( therefore weak probability of run out), (C).
D- Among the ingot mold and cope molding box (D).
E- From the junction of the pouring basin and ceramic gating system(E).

In the sand molds where the main gating system is connected to the mold by means of ceramic tubes, the following items are added to it in addition to the above items:

G- Run out of the melt from the ceramic tube joints (M).
H- Run out of the melt from the ceramic tubes (N).

In permanent molds for roll manufacturing that by assembling one or more round cast iron metal molds on top of each other, there is also the possibility of melt run out from these locations:

H-Among the gaps between assembled metallic molds (P).
I-from gaps between sand molding box and metallic chill molds (R).

In all molds, the entry of melt into the mold space (melt penetration into the mold space) is also called a type of melt run out from the mold, and this possibility is intensified in three areas:

J- under the coreprint (F).
K- From the gap of cope box (G).
L- From the cope box to reinforcing bars (H).
M- melt run out to the core, as a result of transverse cracking of the of core or the presence of volatile substances such as foam inside the core (very low probability).
N- melt run out to gas vents in molding box.

After identifying the most important causes of the defect through the priority risk number, current controls were identified and future actions were presented by team members (Figure 2). The obtained data were analyzed after plotting the graphs (Figure 3).

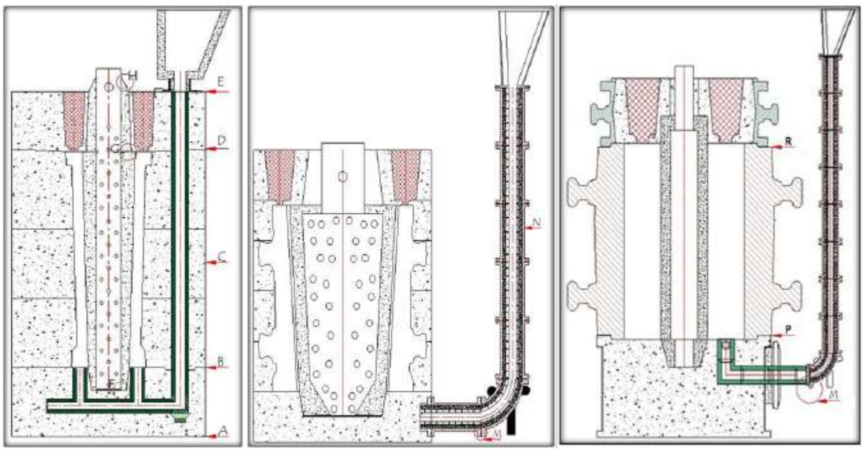

Fig. 1. Most Probably Melt Run Out Positions In Different Molding Processes.

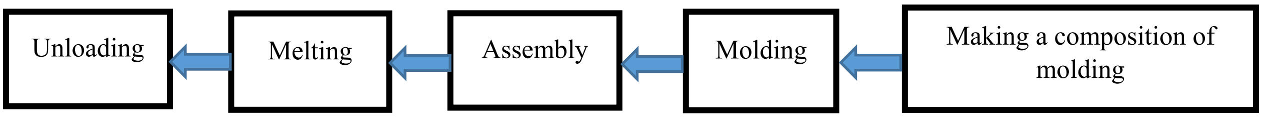

Fig. 2. workflow process form.

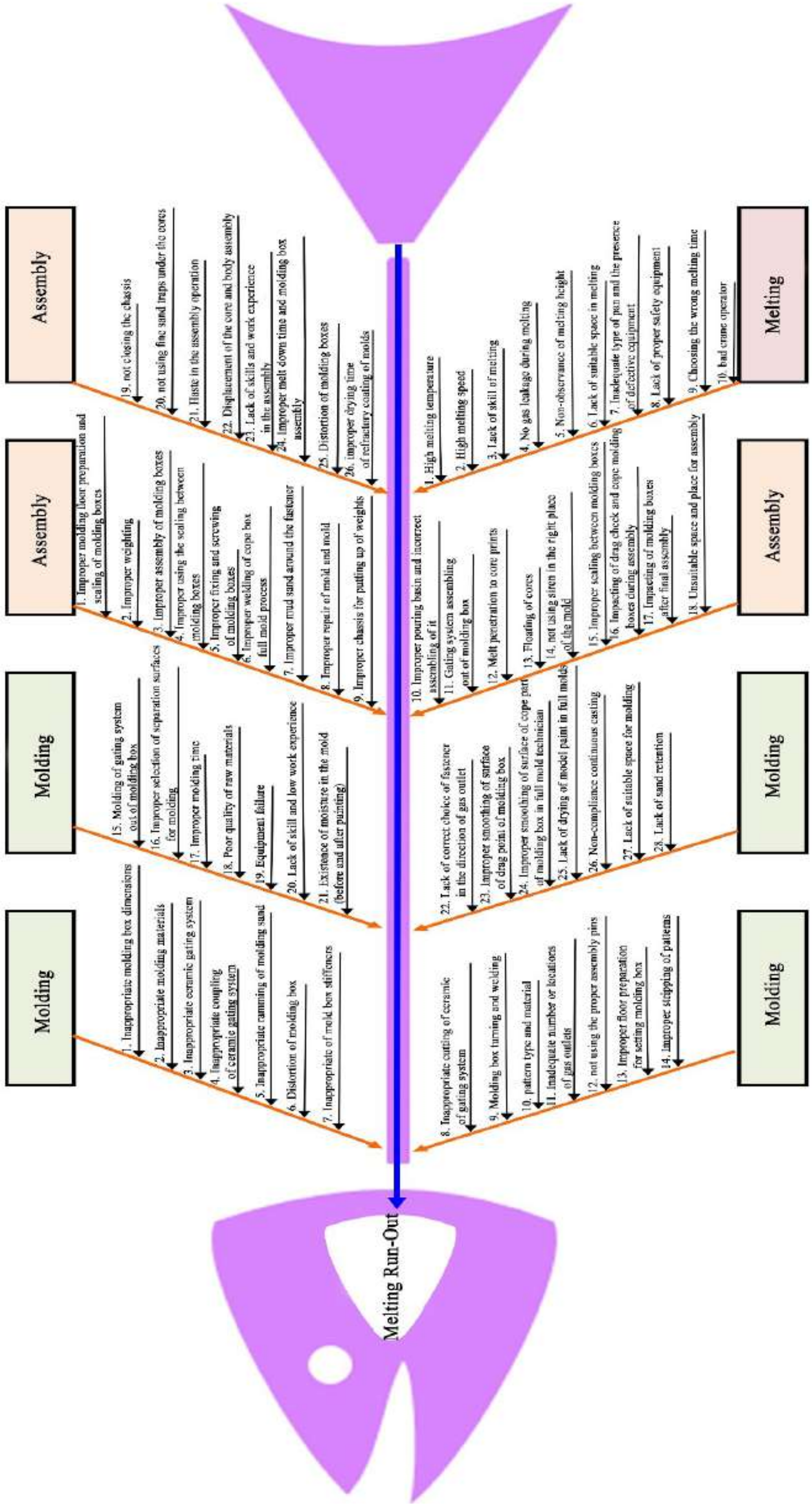

Fig. 3. Fishbone diagram related to melting run-out fault.

The production process in three stages of molding, assembly and melting, were identified and considered to investigate the potential causes of the melting run out process. In the next step, identifying failure modes using customer feedback, defect reports observed in manufactured products, and performing a brain storming to identify potential failure modes were considered and registered in the relevant form. In this method, the evaluation team evaluated three indices of severity (Table 1), the probability of occurrence and the capability to detect for each failure, and then a number between 1 and 10 was assigned to them. The following tables provide qualitative scales on these three common indices. The probability of occurrence also determines the frequency a potential cause or mechanism of danger occurs. It is only by eliminating or reducing the causes or mechanisms of each hazard that can be hoped to reduce the number of events (Table 2). Risk detection probability (detect) is the detection probability of an assessment from the point of capability that identifies a cause or mechanism of occurrence of a hazard; In other words, the possibility of discovering the capability to detect danger before it occurs (Table 3).

Table 1. Form related to the severity of potential failure mode effect.

| Ranking / impact factor | | | | |
|---|---|---|---|---|
| | Impact on the internal process | Example / Description | Impact on the customer process | Example / Description |
| 1 | no effect | fastener difference in size of 3 to 5 cm | no effect | Subsurface defects in areas of the part that are not affecting application of part |
| 2 | Like the process goes on by spending time and without much change. | High temperature when casting unbreakable cast iron | The part works and there is no possibility for the customer | Improper structure in some cast iron grades |
| 3 | The process continues with minor repairs | Staining while molding | The part works and there is a possibility of fault detection for the customer | Welding repair on non-critical location of casting parts and surface defects |
| 4 | A part of the process needs to be reworked | The color of the mold must be repainted | The part works and the defect can be solved by the customer | Blistering or sandblasting in invisible places of parts |
| 5 | The part can be sent with major repairs and rework. | Welding the part | The part works with lower efficiency | Low strength |
| 6 | The part runs into problem in casting by the melt run-out | small explosion inside mold | The part works with lower efficiency and the customer is dissatisfied | Welding repair of parts |
| 7 | The piece is lost in the casting stage | crack after evacuation | The part works with lower efficiency and causes severe customer dissatisfaction | Dislodging of ingot mold inner surface by melt |
| 8 | The part is lost without any loss of life | melt run-out or reduction of melt volume inside the mold due to penetration into the mold | The melt runs out from the ingot and the plates and can be remanufactured. | Washing and erosion of ingot mold base or bare plate by melt |
| 9 | The part is lost and the equipment is damaged | high melt run-out or high tonnage | The part is lost and causes damage and stops the customer's production line | Ingot mold cracking and melt run-out and destruction of base plate and trumpet |
| 10 | The part is lost and there is a loss of life | Mold explosion | The part is lost and causes the customer's production line to stop | Ingot mold breaking during pouring and severely melt run-out |

Table 2. Form related to the probability of occurrence of potential failure modes.

| Ranking / impact factor | occurrence | |
|---|---|---|
| | occurrence | Example / Description |
| 10 | Over 50% | Very high occurrence / rejecting of 7 pieces out of 10 |
| 9 | Over 20% | Very high occurrence / rejecting of 4 pieces out of 10 |
| 8 | Over 15% | Very high occurrence/ rejecting of 3 pieces out of 10 |
| 7 | Over 10% | Very high occurrence / rejecting of 2 pieces out of 10 |
| 6 | Over 7% | moderate occurrence and waste / 1 out of 10 parts |
| 5 | Over 5% | Moderate occurrence / rejecting of 4 pieces out of 10 |
| 4 | Over 3% | Low occurrence / rejecting of 3 pieces out of 10 |
| 3 | Over 1% | Low occurrence and waste with rework/ rejecting of 2 pieces out of 10 |
| 2 | Over 0.001% | Low occurrence / rejecting of 1 piece out of 10 |
| 1 | Less than 0.001% | Rare occurrence with little surface defects, rejecting of 3 pieces out of 10 |

Table 3. Form related to the possibility of detect of potential failure modes.

| Ranking / impact factor | detection | |
|---|---|---|
| | occurrence | Example / Description |
| 1 | There are definite controls for defect detection. | Loss of the part due to melt run-out |
| 2 | It can be detected by visual inspections / (it is detectable) | Loss of the part due to melting run-out |
| 3 | It can be detected by visual inspections / (it is detectable) | surface defects as sand burning and surface cracks and fines |
| 4 | It can be detected by visual inspections / (it is detectable) | Surface cracks and voids that revealed after grinding |
| 5 | It can be detected by visual inspections / (it appears after casting) | Surface shrinkage draws |
| 6 | There are special tools for detection / can be detected by testing | Voids in casting parts due chemical analysis fault after determination by remelt |
| 7 | Requires special non-routine tests / can be possibly detected | Tensile strength or ultrasonic testing as necessary |
| 8 | It is recognizable, but it is not seen in the initial examinations / it appears in the turning phase | Inside voids that revealed after machining |
| 9 | Cannot be identified or not checked / will be identified by customer inspections at the post-delivery stage | Subsurface cracks that are identified after machining |
| 10 | Unrecognizable / will definitely not be discovered and will be identified during operation | Cracking and failure of ingot mold during pouring |

The basis of analysis in FMEA technique is calculating the multiplication of the values of these three indices for each failure mode; In this way the risk priority number (RPN) of the failure mode is obtained. To determine the weight of the considered risks, the severity (S), occurrence (O) and detect or detection (D) have been evaluated. Higher-numbered failures are a priority, and the assessment team must first analyze the higher-priority failures. In the mentioned questionnaire, the colleagues were asked to assign a number from very low to very high for each of the effective cases in melting: intensity, occurrence and detect. The value of RPN for each index is:

$$RPN = S \times O \times D \qquad \text{Eq. (1)}$$

In this relation, RPN = risk priority number, D = detection, O = occurrence and S = severity [1]. There is another new way to classify the severity or risk of failures. This new method, called "Area Chart", is of particular importance for the severity and occurrence [1, 3, 6]. This chart focuses on three areas: high priority area, medium priority area, and low priority area.

Detection is an estimate of the control process capability that is used to diagnose the causes of design failure or the capability to detect faults. Occurrence indicates the probability of any cause of failure being determined. The severity of failure is an estimate of the severity of failure on the process. To number each of these factors, a summary and localization of special tables presented in various sources was used. Ranking is done by group members using the brainstorming method. Usually a number of high-process RPNs are considered to examine the high-risk process [1, 3, 6].

## 3. Discussion

### 3.1. Summary, potential modes of failure

The result of the RPN in three stages of molding, assembly and casting is presented in the diagram below to obtain the critical points (Diagram 1).

### 3.2. Determine the Acceptable Risk

In the method used in this research, the risk criterion number has been used for the acceptable point of risk. Risk criteria is an index for separating acceptable and unacceptable risk. A failure whose RPN number is more than the risk criteria is unacceptable and will be acceptable if it is less than the risk criteria. To determine the risk criteria, a scatter diagram was drawn for each component of the device based on the RPN number and the critical point of that component. According to the diagram, the first point that is placed in critical point 3 is the risk criteria for the process.

### 3.3. Define the Critical Point

In the ranking of factors, from the number 6 and above, the effect has the probability of occurrence of waste in the state of failure, then this number is chosen as the basis of the criticality of the factors in this research [9,10].

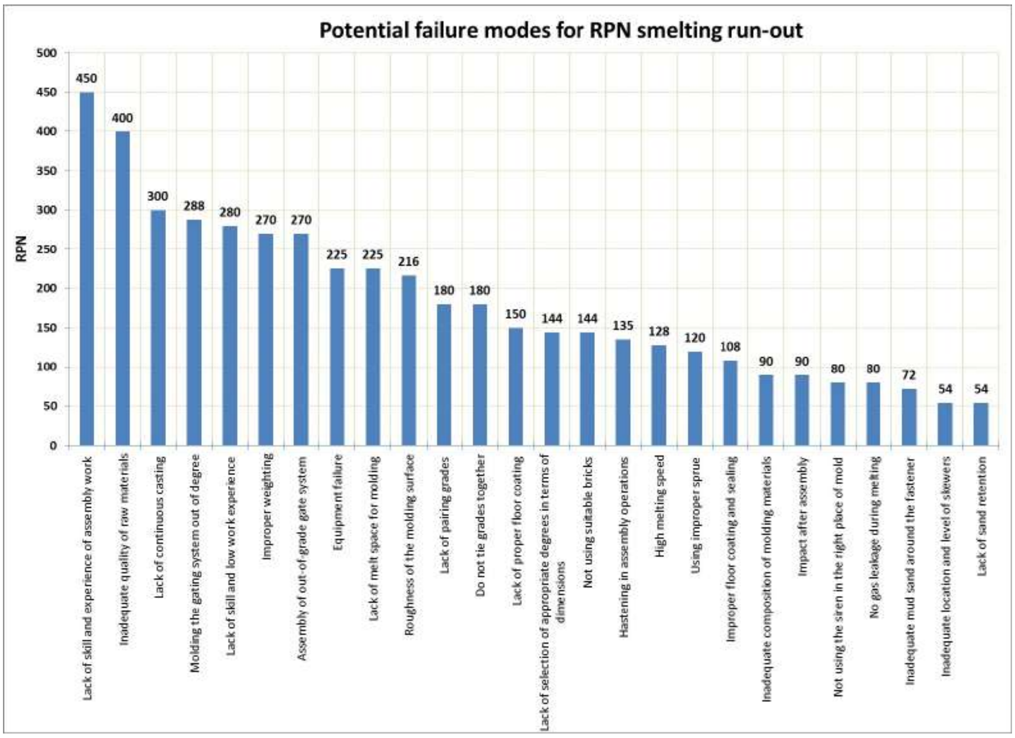

Diagram 1. RPN potential mode of total system failure.

Point 1- Normal point which all three factors of the RPN number have a number less than 6 or the RPN number is low and therefore need for preventive actions is not felt.

Point 2 - The semi-critical point which a maximum of one of the three factors of the RPN number has values higher than 6 but the RPN number is low. In this case, it is necessary to take preventive actions.

Point 3 - Critical point in which at least two of the three factors of the RPN number have values higher than 6. It is clear that this point requires immediate preventive actions (Diagram 2 and Table 4).

Table 4. Analysis of potential failure modes in production processes at the critical point 3.

| row | Operation phase | Potential failure mode | Intensity | occurrence | detection | RPN | Critical Points | Needed measure |
|---|---|---|---|---|---|---|---|---|
| 1 | Assembly | Lack of skills and work experience in assembly | 9 | 5 | 10 | 450 | 3 | Needs immediate preventive action |
| 2 | Molding | Inadequate quality of raw materials / lack of control of input materials | 8 | 5 | 10 | 400 | 3 | Needs immediate preventive action |
| 3 | Molding | Failure to observe continuous molding | 5 | 6 | 10 | 300 | 3 | Needs immediate preventive action |
| 4 | Molding | Molding the out of molding box gating system | 8 | 4 | 9 | 288 | 3 | Needs immediate preventive action |
| 5 | Molding | Lack of records and low work experience | 7 | 5 | 8 | 280 | 3 | Needs immediate preventive action |
| 6 | Assembly | Improper weighting | 9 | 3 | 10 | 270 | 3 | Needs immediate preventive action |
| 7 | Assembly | Assembling the out of molding box gating system | 9 | 3 | 10 | 270 | 3 | Needs immediate preventive action |

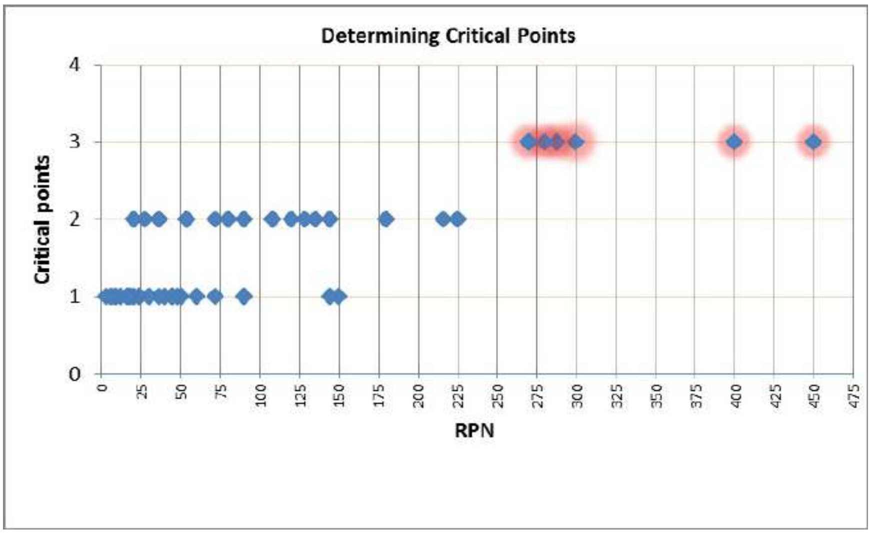

Diagram 2. Determination of critical points.

### 3.4. Proposed Actions

After prioritizing failure modes based on RPN number, corrective and preventive actions should first focus on priority and critical cases. The intention of any proposed action must be to reduce the number of at least one of the three cases of "occurrence", "severity" and "detection". All the proposed actions in the study were defined for potential failure modes that have a critical point of 3.

### 3.5. Recommendations

After determining the corrective and preventive actions, the person responsible for its execution and the time required to perform it were also determined. To do this, the following recommendations are presented as corrective and preventive actions.

A- Immediate training for personnel (defects  training class for personnel)

B- Performing specialized training at the beginning of employment for semi-skilled technical workers in the production line by the technology unit

C- Using the monitor to monitor the drawings and instructions on a daily basis and with the plan for the production line

D- Examining the  gating system designs in different parts that use double-sprue design and revising them to single-sprue gating system design

## 4. Conclusions

After performing all the initial phases of FMEA, the following results were obtained to reduce the losses in the run-out process in three points of critical (point 3), semi-critical (point 2) and insensitive (point 1):

- The highest RPN is related to lack of skill and experience of personnel in assembly, inadequate quality of raw materials, non-compliance with continuous molding, molding of out-of-box gating system, low staff experience and improper weighting, with RPN number 270, 270,280,288,300,400,450, respectively which also included critical points. For solving this problem we decide to more experienced molding workers and as a result the severity of problem due to this matter considerably reduced.
- According to the obtained results, it was decided that the training of casting defects in the production line for the executive personnel should be in the forefront. By this action and after evaluating the results the run out problem reduced considerably.
- It was also decided to be on the agenda the checklist of input items affecting the direct quality of parts production, and review the quality specifications of the input and, if necessary, adding the technical specifications, as well as provide tools or control methods for input items that have no criteria for entering the line.
- Controlling the mechanized molding machine , placing a continuous technical expert next to the molding system to eliminate possible defects in a timely manner, reviewing the designs made in the appropriate gating system, and using gating systems inside molding box and application of standard weights for the production line were some decisions that were made .At the end by permanent control of an expert on sand mixer working process the problem due to mixer and sand quality that caused run out defect considerably reduced .

## References

[1] Stamatis, D. H. “Failure Mode and Effect Analysis: FMEA from Theory to Execution.” ASQ Quality Press, 2003.

[2] Pazireh E. FMEA, An Efficient Method for Failure Mode and Effects Analysis, Nassaji Emrouz Magazine, December 1996, No. 180 (in Persian).

[3] McDermott, Robin; Mikulak, Raymond and Beauregard, Michael. “The Basics of FMEA.” Taylor and Francis Group, 2009.

[4] Zentis, T. Schmitt, R. “Technical Risk Management for An Ensured and Efficient Product Development on The Example of Medical Engineering”, Smart Product Engineering, pp. 3 7-39, 2013.

[5] Abdullah Zadeh G. Haghighi F. R. Taheri M. J. Rastgou S. Seismic Risk Assessment of Bridges in Babolsar City in Operational Mode Using FMEA-FUZZY Method", Haml-o naghl Research No. 3, Vol. 13, 2015.

[6] Seung, Rhee; Kosuke, Ishii. “Using Cost Based FMEA To Enhance Reliability and Serviceability.” Advanced Engineering Informatics, 2003, Vol.17, pp.179-188.

[7] Bahramian, Mahdi; Hadizadeh, Danial and Sajjadi, Mojtaba. “Innovation and Improvements in Project Implementation and Management; Using Fmea Technique.” Procedia-Social and Behavioral Sciences, 2012, Vol.41, pp. 418-425.

[8] Zhou, J and Stalhane, T. “Using FMEA for early robustness analysis of Webbased systems.” Proceedings of the 28th Annual International Computer Software and Applications Conference, 2004, Vol.2, pp. 28-29.

[9] Jabbari, M., Asilian, H., Mortazavi, S. B., Zarringhalam, A., Hajizadeh, E., and Khavanin, A. (2009). “Risk Assessment and Management of Petrochemical Transportation Pipelines.” Journal of Industrial Engineering, Vol. 3, No. 1, 13-23.

[10] Liu, M. and Wu, F. F. (2007). “Risk management in a competitive electricity market.” Electrical Power and Energy Systems, 29, 690-697.

International Journal of ISSI, Vol. 19(2022), No. 2, pp. 51-58

# Microstructure and Mechanical Properties of Service-Exposed HP-MA Heat-Resistant Steel Tube, Used in Cracking Furnaces

**A. Torabi** [1], **H. Pourmohammad** *[2], **A. Bahrami** [3], **A. Eslami** [4]

*Department of Materials Engineering, Isfahan University of Technology, Isfahan 84156-83111, Iran*

## Abstract

Cracking tubes as the main part of an olefin unit, are exposed to very harsh working conditions at both outer and inner surfaces, associated with major microstructural changes during service. Carburization, oxidation, alloying elements depletion, carbide coarsening, and secondary carbide formations are common phenomena, expected to take place in cracking tubes. This research tries to experimentally investigate the implications of cracking service exposure on microstructure and mechanical properties of the service-exposed HP-MA cracking tubes. In this regard, two tube samples after 20000 and 45000 h service at approximately 900 °C were selected. Microstructure degradation at the inner and outer surfaces of the tubes and their mid-thickness were investigated with optical and electron microscopes. By microstructural characteristics of both tube samples, it was concluded that in the 45,000-hour sample, which was more exposed to carbon, the number of secondary carbides formed on the outer surface was higher. Hardness variation across the thickness was also measured for both tubes and according to the results, in total thickness of the 45,000-hour sample, the hardness was more than the 20,000-hour specimen.

*Keywords:* Carburization, Cracking Tubes; Heat-resistant steels; HP-MA steel; Oxidation.

## 1. Introduction

Cracking furnaces are the main part of an olefin unit, in which valuable products such as ethylene are produced, through a cracking chemical reaction [1]. The heat generated to perform the thermal cracking process is radiated to the outer surface of cracking tubes in which the feed is passing by. Heat resistant cast steels are used as coils and tubes in cracking furnaces, as they have excellent high temperature corrosion resistance, oxidation resistance and high temperature creep strength [2-5]. These steels are constantly subjected to the process of decoking and on/off cycles and exposed to very harsh working conditions such as high temperatures and existence of oxidizing, nitriding and carburizing agents and atmospheres. Also, the operating temperature of these tubes varies from 800-1100 °C. [6-10]. Heat resistant cast steels are austenitic alloys, contain large amounts of carbide-forming elements in their chemical analyses, providing the room for the formation of significant amounts of uniformly distributed primary and secondary inter-dendritic carbides [11-14]. The optimal life of cracking tubes is approximately 100,000 hours if they are exposed to a temperature of 900 °C. However, it is known that oxidation and carburization reactions in cracking furnaces take place rather early, typically after 10,000 hours of operation, increasing the tubes' length and reducing their weldability [15]. This is associated with some major microstructural changes and deterioration of mechanical properties. Initially, the presence of chromium oxide layer at the surface of the tubes prevents the inter-diffusion of carbon towards the bulk of tubes.

---

*Corresponding author
*Email: hodapourmohammad@ma.iut.ac.ir*
*Address: Department of Materials Engineering, Isfahan University of Technology, Isfahan 84156-83111, Iran*
[1] *B.S.*
[2] *M.S.*
[3] *Assistant Professor*
[4] *Associate Professor*

Over time, the oxide layer is damaged, resulting in the oxygen and carbon penetrations into the tubes. The diffusion of the former with high temperature oxidation, while the latter phenomenon causes carburization. Carburization is accompanied by the formation of secondary carbides and degradation of primary carbides. The effect of carburizing on the tubes can be represented by a continuous carbide network formed on the grain boundaries at elevated temperatures, which may be a favorable site for crack growth and imposes the risk of creep degradation and deterioration of ductility at high temperatures. Although some negative aspects of carburization are known, not much is known about how microstructure is evolved during carburizing service condition. This research tries to methodically investigate the implications of carburization for the microstructure and mechanical properties of service-exposed cracking tubes.

## 2. Materials and Methods

The microstructure and mechanical properties of service-exposed G4852-Micro steels, also known as HP-MA steels (which were prepared by centrifugal casting), with the thickness of 10 mm, were investigated in this study. In this regard, tube samples were taken from cracking tubes after 20000 and 45000 hours service exposure in the temperature range of 900-950 °C. Samples were cut from aged tubes to analyze the mechanical properties and to perform various tests. Chemical composition of the tube is given in Table 1.

The cross section of the samples was grounded with silicon carbide grinding papers of 80 to 1200 and then polished with 0.1 micron alumina particles. In addition, $H_2O/HF/HNO_3$ etching solution according to NACE TM0498 standard was used to prepare samples for metallographic examinations. The cross sections of the samples were also investigated by scanning electron microscope at different magnifications. Also, the inner edge, the middle region and the outer edge, were examined by chemical analysis. Vickers microhardness profilometry was carried out by applying 1 kg force on the cross section of the specimens at distances of about 1 mm from the inner to the outer surface of the tube.

## 3. Results and discussion

Fig. 1 shows microstructure of the as-cast heat-resistant specimen, before service exposure. In the image taken from the cross section of the sample, austenitic background and primary skeletal $M_{23}C_6$ carbides at grain boundaries, where M comprises Fe and Cr, can be seen.

Fig. 2 depicts EDS analyses of different phases in the as-cast specimen. The white phase in this structure is rich in Nb, which can be concluded it is a niobium carbide phase. The grayish phase, on the other hand, is rich in chromium, inferring that this phase is a chromium carbide phase.

Table 1. Chemical composition of the investigated tube.

| Sample | C | Ni | Cr | P | S | Si | Mn | Mo | Nb | Ti |
|---|---|---|---|---|---|---|---|---|---|---|
| **Service-Exposed Tube** | 0.4 | 35.0 | 26.3 | 0.015 | 0.01 | 0.9 | 1.0 | 0.1 | 0.9 | 0.008 |
| **ASTM A 608-20** | 0.38 –0.45 | 34.0 – 37.0 | 24.0 – 27.0 | 0.03 max | 0.03 max | 0.50 – 1.50 | 0.50 –1.50 | 0.50 max | 0.50 –1.50 | - |

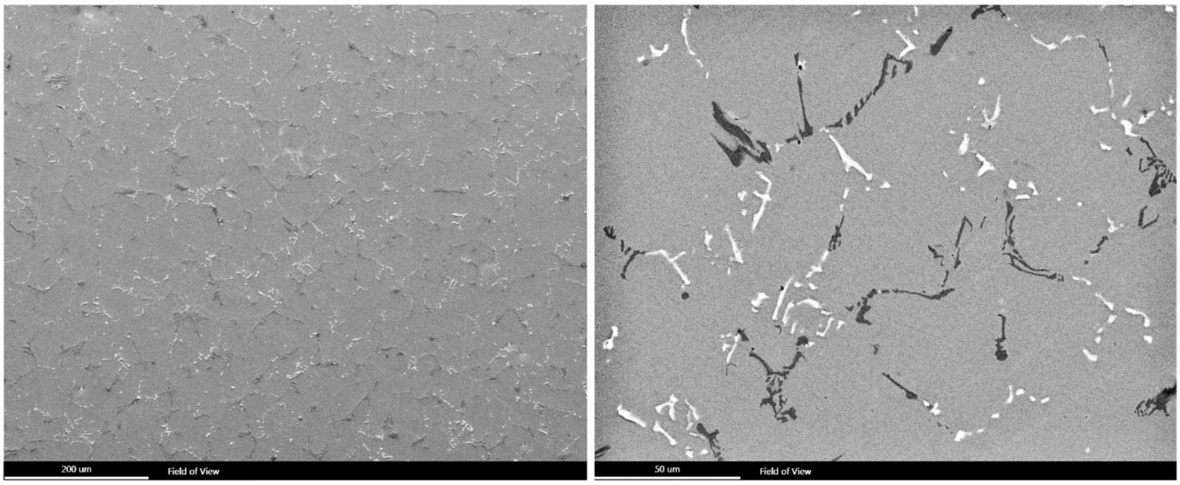

Fig. 1. Typical SEM micrograph of as-cast HP-MA alloy.

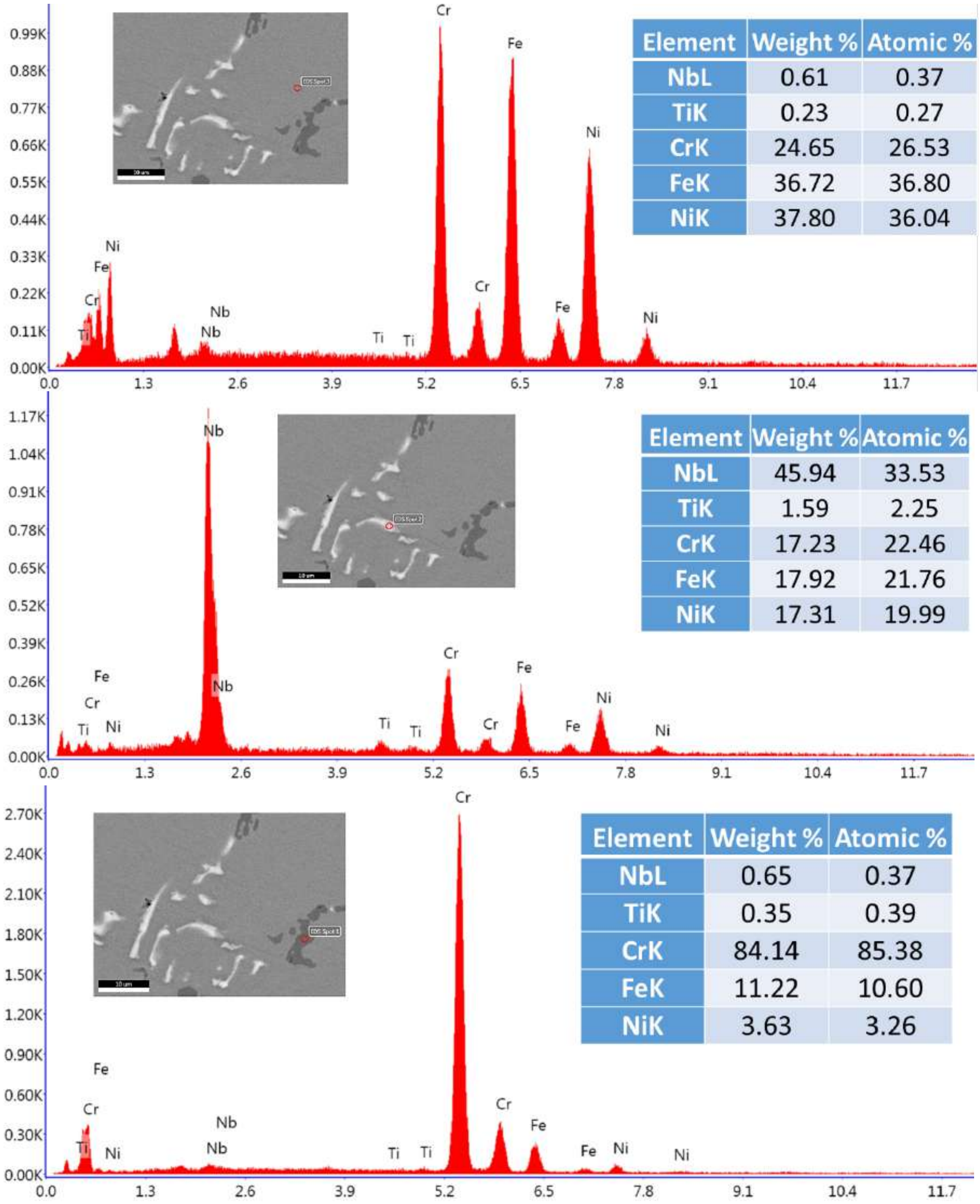

| Element | Weight % | Atomic % |
|---|---|---|
| NbL | 0.61 | 0.37 |
| TiK | 0.23 | 0.27 |
| CrK | 24.65 | 26.53 |
| FeK | 36.72 | 36.80 |
| NiK | 37.80 | 36.04 |

| Element | Weight % | Atomic % |
|---|---|---|
| NbL | 45.94 | 33.53 |
| TiK | 1.59 | 2.25 |
| CrK | 17.23 | 22.46 |
| FeK | 17.92 | 21.76 |
| NiK | 17.31 | 19.99 |

| Element | Weight % | Atomic % |
|---|---|---|
| NbL | 0.65 | 0.37 |
| TiK | 0.35 | 0.39 |
| CrK | 84.14 | 85.38 |
| FeK | 11.22 | 10.60 |
| NiK | 3.63 | 3.26 |

Fig. 2. EDS analyses of different phases: the matrix, the white phase and the grayish phase in the as-cast structure.

Figs. 3 to 7 show microstructures and EDS chemical analyses of different phases at the inner, the middle and the outer surfaces of aged tubes after 20000 and 45000 hours of service exposure, which are shown from the outer surface towards the inner surface, respectively. As can be seen, both the inner and outer surfaces are heavily influenced by the service exposure, with the thickness of influenced surface layer being larger for the 45000 hours service exposed specimen. The influenced surface layer at both sides contains large blocky shaped islands of black/grayish phases. Moreover, the surface layer appears to be lean in carbide phases. One can also notice that moving towards the outer surfaces, number of fine secondary carbide particles ($M_7C_3$ and $M_{23}C_6$ secondary carbides) increases. It is known that the outer surface is more exposed to carbon, resulting in the penetration and diffusion of carbon towards the bulk of the tube. This, in turn, is associated with the conversion of primary

$M_{23}C_6$ carbides to $M_7C_3$ carbides and formation of newly-formed fine carbide particles [15].

Figs. 5 and 6 depicts SEM micrographs of aged samples, after 20000 and 45000 hours of service. Again, these micrographs show how the structure at both inner/outer surfaces are degraded. In fact, the protective layer of chromium oxide ($Cr_2O_3$) on the surface is an extremely important feature of this alloy, as it prevents the penetration of oxygen and carbon and other harmful elements towards the bulk structure. It appears that service exposure has severely degraded the mentioned protective layer, meaning that the surface structure can no longer resist the penetration of carbon. The fact that Si-rich oxide phases (black phases, see Fig. 7a) have been formed is an indication that the surface and internal oxidation reactions have become active at the early stage of service and operations. EDS results show that while Si-rich oxides are more formed further away from the surface, Cr-rich oxide phases (grayish phase, see Fig. 7b) are observed as a rather thick and porous layer at the surface. This possibly has to do with the difference in the diffusion rates of Cr and Si. This mentioned service-originated Cr-rich oxide layer is typically very porous and in some areas it is further developed to the bulk of the alloy. As a result, the diffusion of carbon into the structure becomes easier, resulting in the carbide coarsening and formation of secondary carbides. The former phenomenon leads to a decrease in high temperature mechanical properties, more specifically creep resistance. The penetration of carbon into the substrate is associated with carburization, and therefore matrix hardening. In order to regenerate the degraded $Cr_2O_3$ layer, the existing chromium in the matrix diffuses towards the surface, resulting in the formation of Cr-depleted areas near the surface. On the other hand, inside the tubes, there is oxygen that has penetrated into the structure and formed dark oxides, which are shown in the inner surface images of the samples. For the sample with 20000 hours service life, this surface layer has a thickness of 250 µm, while in sample with 45000 hours service life, this thickness has increased to 450 µm.

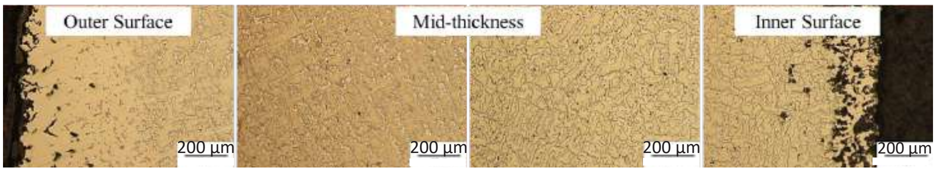

Fig. 3. Typical optical microscope images of the sample after 20,000 hours of service.

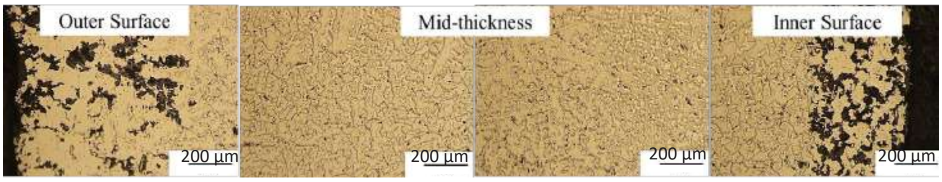

Fig. 4. Typical optical microscope images of the sample used after 45,000 hours of service.

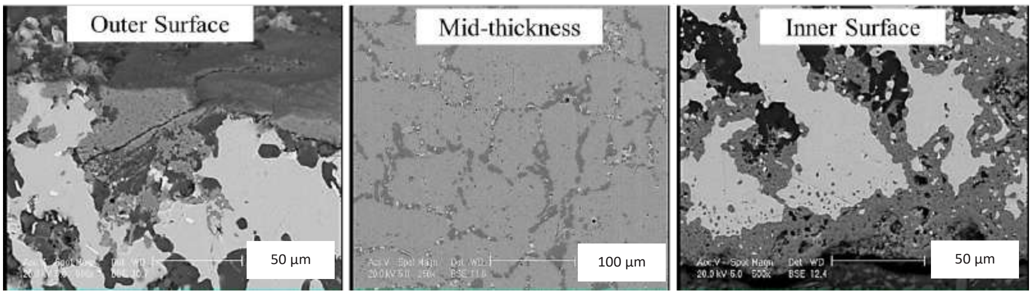

Fig. 5. SEM microscope images of the sample after 20,000 hours of service.

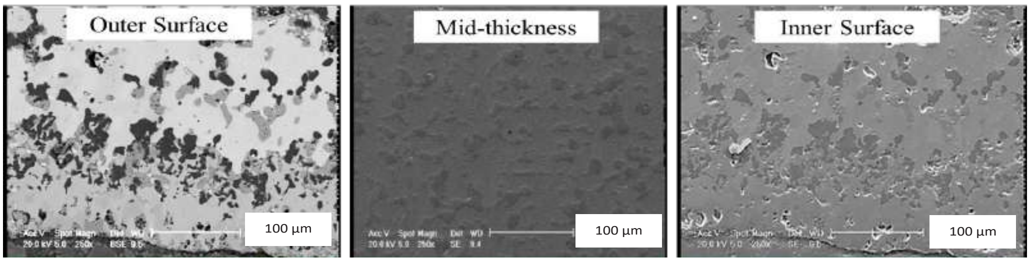

Fig. 6. SEM microscope images of the sample after 45,000 hours of service.

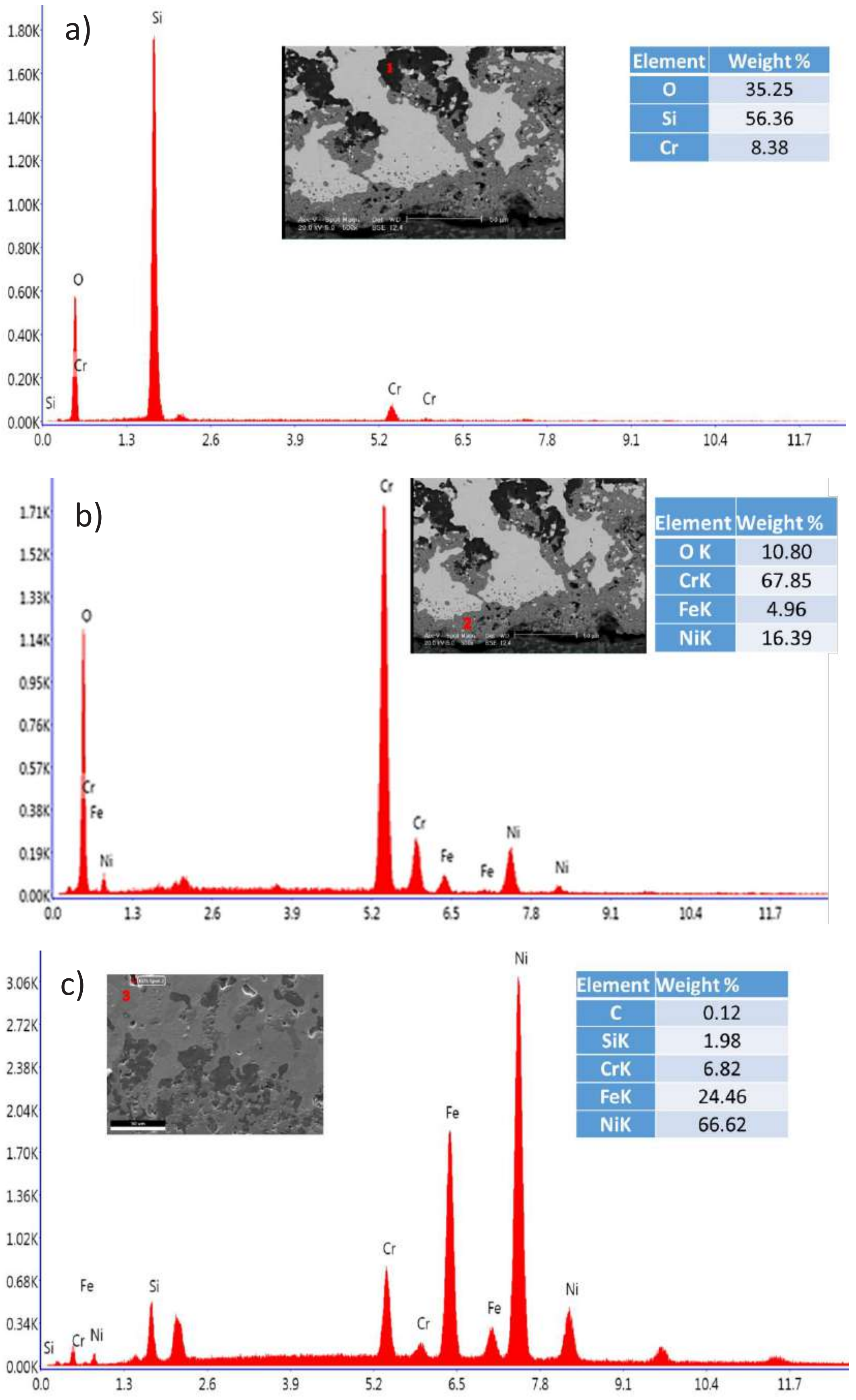

a)

| Element | Weight % |
|---|---|
| O | 35.25 |
| Si | 56.36 |
| Cr | 8.38 |

b)

| Element | Weight % |
|---|---|
| O K | 10.80 |
| CrK | 67.85 |
| FeK | 4.96 |
| NiK | 16.39 |

c)

| Element | Weight % |
|---|---|
| C | 0.12 |
| SiK | 1.98 |
| CrK | 6.82 |
| FeK | 24.46 |
| NiK | 66.62 |

Fig. 7. EDS analyses of a) black phase, b) grayish phase, and c) the matrix in aged samples.

Fig. 8 depicts macro images of the cross-section of the tube after 20000 and 45000 hours of service. The color difference is attributable to the carburized layer. The lighter area is the carburized layer. Fig. 8 shows that the higher the ageing time, this thicker is the carburized layer is, such a way that in 45000-hour aged specimen, almost 70% of the total thickness is carburized.

Figs. 9 and 10 depict elemental mapping at the inner and outer surfaces of the 20000-hour aged specimen, respectively. It appears that both the inner and the outer surfaces are heavily influenced by oxygen, as a thick oxygen layer is seen at both surfaces. Also, it is seen that the segregation of Mn and Cr towards the surface is more pronounced at the outer surface, which has to do with more aggressive environment at the outer side of tubes. A heavily depleted Cr/Mn zone is also visible at the outer surface of the tubes. Another noticeable difference between the outer and the inner surface of the tubes, is morphology of silicon oxide phase. A distribution of rather fine globular silicon oxide particles are observed at the outer surface of tubes, while that is not seen in the inner surface.

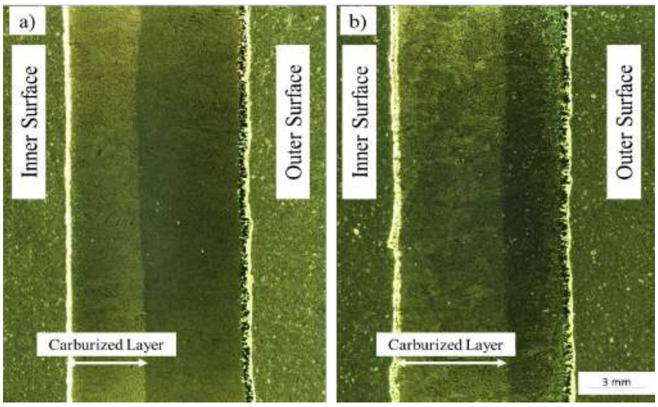

Fig. 8. Macro images of aged tubes, after a) 20000 hours and b) 45000 hours of service exposure.

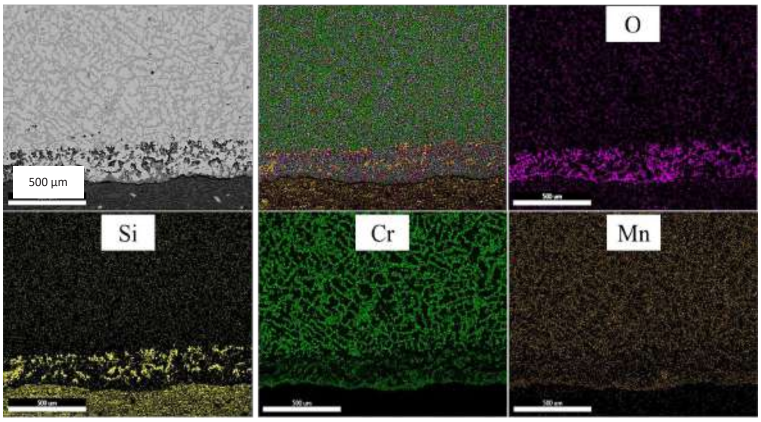

Fig. 9. Elemental mapping at the inner surface of the 20000-hours aged tube sample.

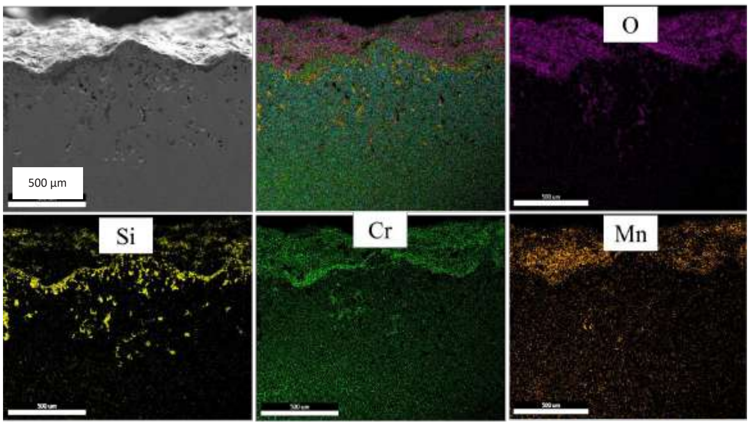

Fig. 10. Elemental mapping at the outer surface of the 20000-hours aged tube sample.

Figs. 11 and 12 depict elemental mapping at the inner and outer surfaces of the 45000-hour aged tube specimen, respectively. It is seen that longer service exposure from 20000 to 45000 hours is associated with the extension of surface-influenced layer. For example, the thickness of oxygen-rich layer at the inner surface has increased to values over 1000 µm after 45000 hours of service, while that in the 20000 hours exposed tube is roughly 200 µm. A comparatively more extensive Cr/Mn-segregated and depleted zones are also noticeable in this sample.

The formation of oxides at the inner/outer surfaces of tube samples, leads to the depletion of elements such as chromium and silicon compared to the middle thickness, which causes a decrease in oxidation resistance, while in the middle thickness, these oxide phases are rarely formed. In addition, because the inner surface of the tube is more exposed to carburizing gases, chromium, in particular, has a strong tendency to react with carbon and secondary carbides are formed in the structure. Due to the presence of oxygen in the furnace atmosphere, it can easily penetrate into the surface of the tubes and oxide phases are formed on the outer surfaces. Since around these oxide phases, it is a suitable place for formation of micro cracks, and network and continuous carbides have changed to separated carbides at a microscopic scale, according to the images, it can be concluded that oxide particles at the surface are preferential sites for the nucleation of micro-cracks. An example of a micro-crack, formed at the end of an oxide island is represented in Fig. 13. The micro-crack in this case is roughly 200 µm.

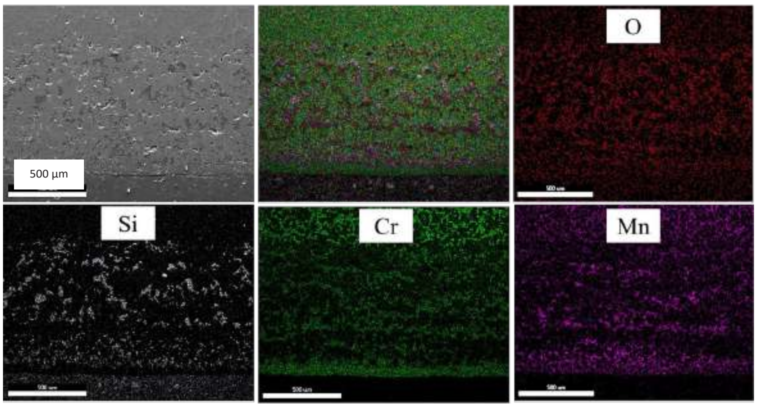

Fig. 11. Elemental mapping at the inner surface of the 45000 hours aged tube sample.

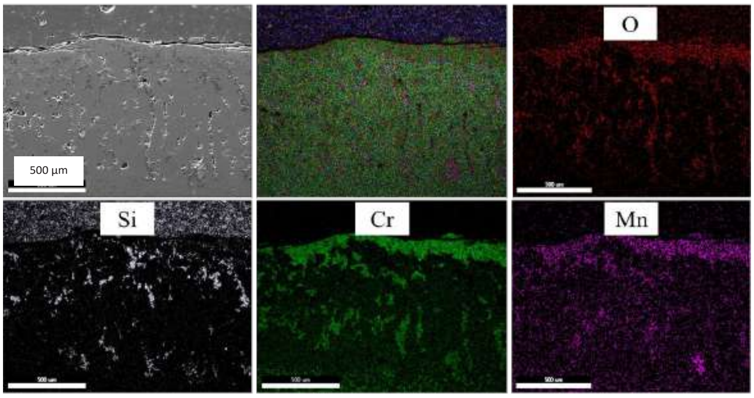

Fig. 12. Elemental mapping at the outer surface of the 45000 hours aged tube sample.

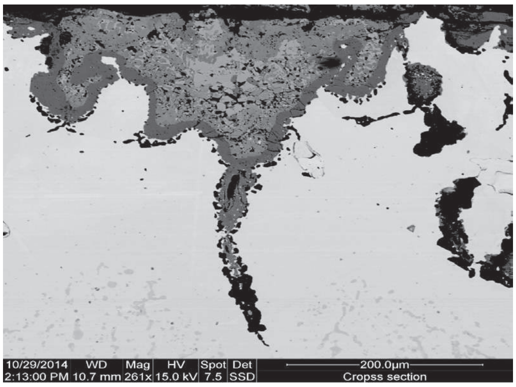

Fig. 13. Micro-cracks, formed at the inner surface of service-exposed tube.

Vickers microhardness measurements for sample with 45000 hours of service, and sample for 20000 hours of service are shown in the Fig. 14. By comparing the presented data, it is concluded that the sample with 45000 hours of service has higher hardness than the sample with 20000 hours of service because it had been exposed to carburization and oxidation for a longer period, associated with the formation of secondary carbides in the structure. According to this diagram, for the 45000 hours service-exposed tube, the hardness is significantly reduced in chromium-depleted areas. However, moving towards the middle thickness of the sample, the hardness gradually increases. 20000 hours service-exposed tube has less hardness changes through the thickness due to lower service time. With mentioning to say that, hardness differences through the thickness can be deleterious when it comes to thermal shock resistance.

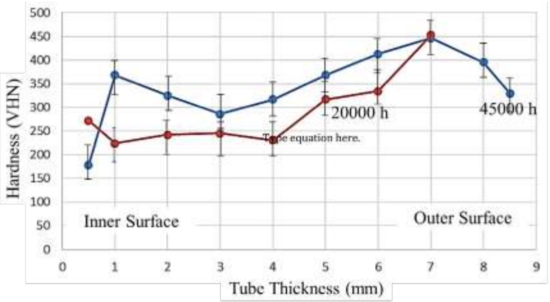

Fig. 14. Microhardness of the tubes from inner surface towards the outer surface.

## Summary

According to this study, it can be concluded that the causes of degradation of alloy steel used in ethylene cracking tubes in petrochemical industry was severe carburization and oxidation. Two tube samples were examined in this investigation: one with service exposure of 20,000 hours and the other after 45,000 hours of service. The investigated tubes had several microstructural characteristics. In this regard, the inner and outer surfaces of the investigated tube samples were exposed to severe oxidation and depletion of chromium and manganese. In addition, carbide particles for the 45,000 hours aged sample were coarser in appearance. Eventually, these continuous and lattice carbides were dispersed, forming suitable locations for initiation of micro cracks; and cracks are expected to form in the samples. As these micro cracks grow, the tube could eventually fail.

## Acknowledgment

The authors would like to thank Isfahan University of Technology for its support.

## References

[1] L.H. Almedia, A.F. Ribeiro, I. Le May, Microstructural characterization of modified 25Cr–35Ni centrifugally cast steel furnace tubes. Materials Characterization, 49(3), pp.219-229.

[2] C.J. Liu, Y. Chen, Variations of the microstructure and mechanical properties of HP40Nb hydrogen reformer tube with time at elevated temperature. Materials & Design, 32(4), pp.2507-2512.

[3] N. Roy, A. Raj, B.N. Roy, A.K. Ray, Creep deformation and damage evaluation of service exposed reformer tube. Canadian metallurgical quarterly, 54(2), pp.205-222.

[4] A.R. Andrade, L.H.C. Bonazzi, Influence of niobium addition on the high temperature mechanical properties of a centrifugally cast HP alloy. Materials Science and Engineering: A, 628, pp.176-180.

[5] S. Shi, J.C. Lippold, Microstructure evolution during service exposure of two cast, heat-resisting stainless steels—HP–Nb modified and 20–32Nb. Materials Characterization, 59(8), pp.1029-1040.

[6] R. Viswanathan, An Overview of Failure Mechanisms in High Temperature Components in Power Plants. Electric Power Research Institute, 122, 246-255.

[7] A. Goswami, S. Kumar. Failure of pyrolysis coils coated with anti-coking film in an ethylene cracking plant. Engineering Failure Analysis, 39, pp. 181-187.

[8] F.C. Nunes, L.H. de Almeida, J. Dille, J.L. Delplancke, I. Le May, Microstructural changes caused by yttrium addition to NbTi-modified centrifugally cast HP-type stainless steels. Materials Characterization, 58(2), pp.132-142.

[9] M. Santos, M. Guedes, R. Baptista, V. Infante, R.A. Cláudio. Effect of severe operation conditions on the degradation state of radiant coils in pyrolysis furnaces. Engineering Failure Analysis, 56, pp. 194-203.

[10] J. Yan, Y. Gao, F. Yang, C. Yao, Z. Ye, D. Yi, S. Ma, Effect of tungsten on the microstructure evolution and mechanical properties of yttrium modified HP40Nb alloy. Materials Science and Engineering: A, 529, pp.361-369..

[11] J.M. Yu, V.H. Dao, V. Lok, T.G. Le, K.B. Yoon, Asymptotic creep deformation behavior of modified HP steel after long-term service. Journal of Mechanical Science and Technology, 34(5), pp.1997-2009.

[12] A. Bahrami, P. Taheri, Creep failure of reformer tubes in a petrochemical plant. Metals, 9(10), p.1026.

[13] C. Maharaj, A. Marquez, R. Khan, Failure analysis of Incoloy 800HT and HP-modified alloy materials in a reformer. Journal of Failure Analysis and Prevention, 19(2), pp.291-300.

[14] A.C. McLeod, C.M. Bishop, K.J. Stevens, M.V. Kral, Microstructure and carburization detection in HP alloy pyrolysis tubes. Metallography, Microstructure, and Analysis, 4(4), pp.273-285.

[15] H. Pourmohammad, A. Bahrami, A. Eslami, M. Taghipour, Failure investigation on a radiant tube in an ethylene cracking unit. Engineering Failure Analysis, 104, pp.216-226.

# Investigating the contribution of wear caused by impact and abrasion in semi autogenous grinding mills

**M. Mohammadi Soleymani *[1], M. Bahiraie [2], M. Rezaeizadeh [3]**

*[1] Department of Mechanical Engineering, Payame Noor University (PNU), Tehran, Iran*
*[2] Department of Mechanical Engineering, University of Applied Science and Technology (UAST) - Misagh, Simin Dasht, Karaj, Iran*
*[3] Department of Mechanical Engineering, Graduate University of Advanced Technology, Kerman, Iran*

---

## Abstract

Milling is one of the most important operational stages in steel and copper processing. Liners and lifters are used inside mill to extend their life and to enhance the grinding and crushing efficiency. The wear of lifters is influenced by a range of parameters such as: media charge level and mill speed. In this work, the researcher used a pilot mill of 1m diameter and 0.5m length to investigate the influences of ball filling and the mill speed on the impact wear of lifters under wet condition. The contribution of impact wear and abrasive wear from the total wear was investigated with new mechanical test method. A copper ore smaller than one inch was used to prepare slurry at 60% solids concentration of mass and slurry filling U=1. The ball filling is 10%, 20% and 30% of mill volume at different mill speeds from 60% to 100% of the critical speed. It was found that while there is an increase in ball filling the wear impact decreases. The wear rate was maximum when the mill speed varied between 80% and 90% of the critical speed. To find out the role of impact on the wear, a mechanism was devised and installed on the pilot mill to prevent the cascade motion.

*Keywords:* Semi autogenous grinding mill, Wear of lifter, Impact wear, Abrasive wear, Wet grinding.

---

## 1. Introduction

Milling is one of the most important operational stages in processing the minerals. Ball mills and semi autogenous grinding (SAG) mills are of the common types. SAG mills include a rotary cylindrical pipe that made of steel plates. Inside a mill, materials change from large dimensions into small due to impact and abrasion processes. For wear protection, the inner surface of the mill is covered by liner. The wear of lifters/liners has dramatic effects on the mill performance due to the loss of lifting. Also the replacement of the worn lifters takes a long time. Besides, unsystematic breakage and the lifters replacement would cause several undesirable downtime of the mill. Therefore, the recognition of the effective parameters on the wear may improve the efficiency of the mill [1-3]. The mechanism (or processes) of wear is in five categories; adhesive wear, abrasive wear, surface fatigue, fretting wear and erosive wear [4-7]. Also, it should be noted that the impact wear (type of erosive wear) happens particularly in the SAG mills. Fig.1 shows the exterior view and interior view of a SAG mill. Fig.2 shows the load behavior in a wet SAG mill.

To predict the lifter/liner wear, different methods have been proposed. To anticipate the lifters wear, Radziszewski [9] suggested a correlation with laboratory data. Cleary have explained how the Discrete Element Method (DEM) could be used for the wear prediction [10]. The wear of lifter profiles in dry coal grinding mills was stud-

---

*Corresponding author
Email: mmsoleymani@pnu.ac.ir
Address: Payame Noor University (PNU), P.O. Box. 19395-3697, Tehran, Iran.
1. Assistant professor
2. M.Sc
3. Associate Professor

ied by Kalala et al. [11]. In order to measure the mass loss due to the wear in a real SAG mill, Banisi, Yahyaei and Hadizadeh [12, 13] employed a mechanical lifter wear monitor. Moreover, Radziszewski has proposed an equation for mass loss in a tumbling mill [14]. In order to examine the forces in the mill charge region, a theoretical model was exploited by Rezaeizadeh et al. [15]. They employed the DEM model to compute the balls velocity profile in the mill.

In another work carried out by Rezaeizadeh et al. [16], an experimental mill with the possibility of working under both dry and wet conditions was exploited to investigate the influence of mill speed, ball filling, size of ore and the material of the lifters on the wear. Also, they studied the distribution of particles in the mill using DEM. They found that the effect of impact in the toe region is higher on the liner wear [17]. In addition, Teeria [18] studied the wear impact of different materials. The effect of lifter wear on the load behavior of an industrial dry tumbling mill [19], and then the effect of lifter shape and number of lifters on lifter wear, were investigated [20, 21]. It is important to note that a few studies have been published for the assessment of wear of lifters in tumbling mills under the wet condition and available data in this area are rather limited and scarce [22, 23]. However, some articles reported experimental results of impact forces, slurry concentration and slurry filling on the wear of lifters in tumbling mills [8, 24]. The impact wear and abrasive wear of lifters in dry SAG mill were studied experimentally by Bahiraei in his master thesis [25].

The previous works reported that the wear impact provides a negligible contribution to the wear of lifters in SAG mills. Hence, it was proposed that abrasion wear provides the prime contribution to the lifter wear in tumbling mills. Therefore, in this study, abrasive wear and the effect of the impact forces are considered. The wear of lifters in this work is due to a combination of corrosion, impact and abrasive wear. To find the contribution of wear due to impact and abrasion a mechanism was devised and installed on the pilot mill to prevent the cascade motion under wet condition.

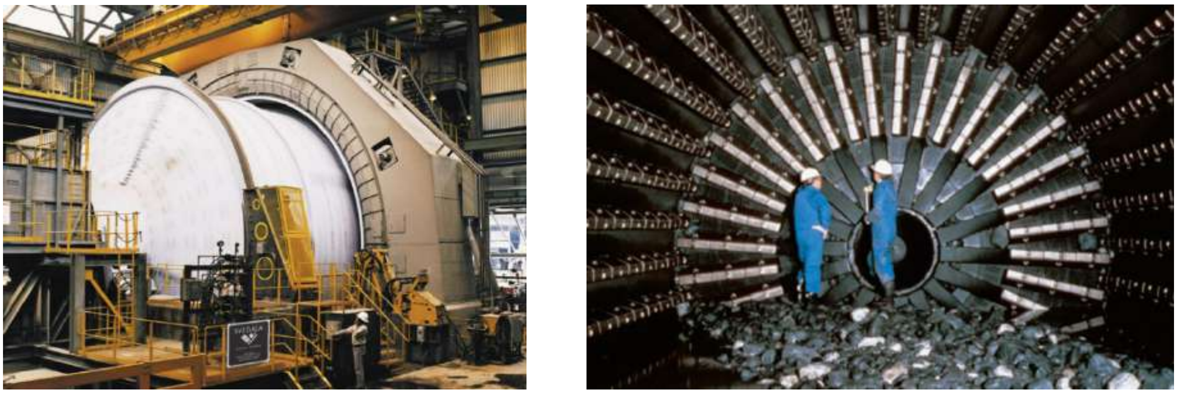

Fig. 1. Exterior view and interior view of a SAG mill [2].

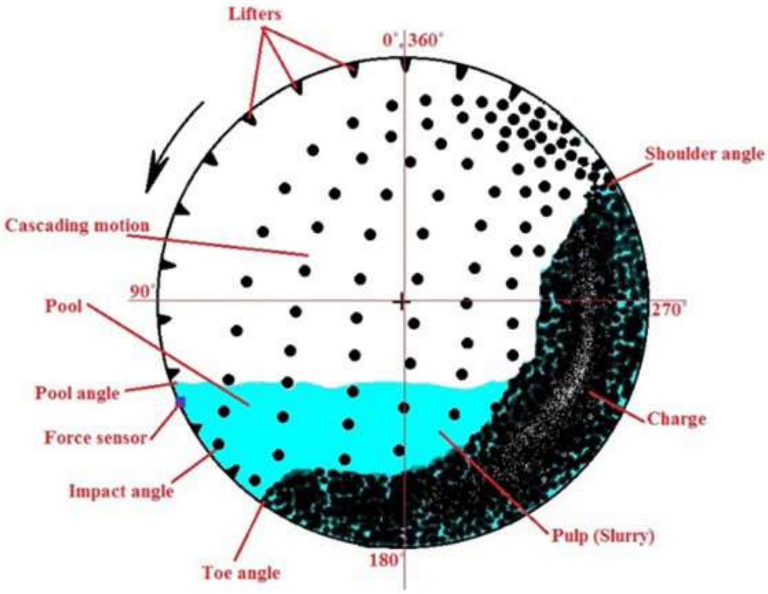

Fig. 2. Definition of the load behavior in a wet tumbling mill [8].

## 2. Materials and Methodology

A schematic view of the experimental pilot mill is illustrated in Fig. 3. In the rig, there are 15 lifters with 50mm height and face angle of 30˚. In the present work, the combination of the balls (40% of the balls with 60mm diameter, 40% of the balls with 40mm diameter and 20% of the balls with 25mm diameter) was used as grinding media with 10%, 20% and 30% of the total volume of the mill. The mill motor was capable of adjusting its rotation up to 100% of critical speed. The critical speed is defined as the rotational speed where centrifugal forces equal gravitational forces at inside surface of the mill's shell. This is the rotational speed where balls will not fall away from the mill's shell. The applied speeds to this study were 60%, 70%, 80%, 90% and 100% of the critical speed. In Table 1, the mill characteristics and grinding conditions are listed.

To find out the role of the wear occurred because of impact and abrasion a mechanism was invented (Fig. 3). This device was installed on the pilot SAG mill to prevent the cascade movement under the wet condition. This device can be adjusted to different angles for various speeds to the specified direction. The device consists of a curved plate which was connected through a shaft to a fixed anchor out of the mill. To adjust the angular position of the curved plate, a scaled plate was employed.

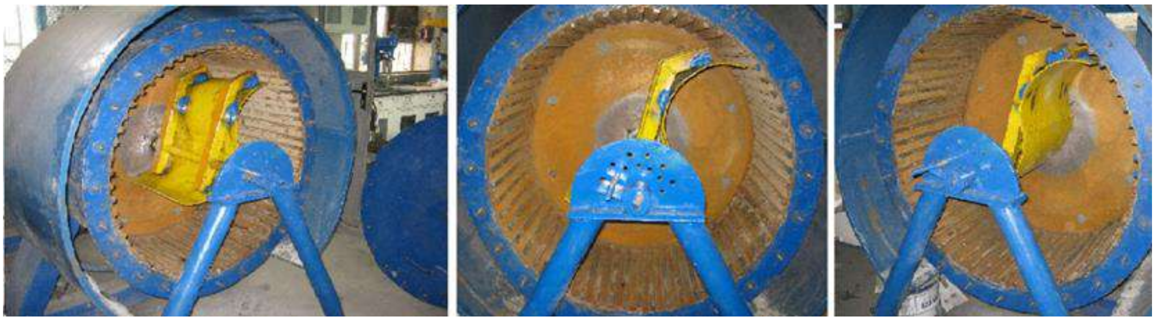

Fig. 3. Lateral device that installed in pilot SAG mill to prevent cascading motion.

Table 1. Mill characteristics and grinding conditions.

| | |
|---|---|
| Mill | |
| Diameter | 1000 mm |
| Length | 500 mm |
| Speed | 25, 29, 34, 38 and 42 rpm |
| Fraction of critical speed ($\Phi_c$) | 0.6, 0.7, 0.8, 0.9 and 1 |
| Lifters | |
| Number | 15 |
| Height | 50 mm |
| Face angle | 30 degree |
| Shape | Trapezoid, leg thickness 50 mm |
| Grinding media | |
| Material | Chrome alloy steel |
| Ball diameter | 40% of the balls with 60mm, 40% of the balls with 40mm, and 20% of the balls with 25mm diameter |
| Density | 7800 kg/m$^3$ |
| Ball filling ($J_b$) | 0.1, 0.2 and 0.3 fraction of mill volume |
| Total ball mass | 176, 352 and 528 kg |
| Feed | |
| Material | Copper ore |
| Particle size | $F_{100} = 25.4$, $F_{80} = 12.7$, $F_{50} = 8$ and $F_{10} = 0.3mm$ |
| Ore density | 2700 kg/m$^3$ |
| Slurry concentration (C) | 0.6 (mass fraction of solid in slurry) or 35 (vol.% solid) |
| Slurry density | 1610 kg/m$^3$ |
| Slurry filling (U) | U=1 (as volume fraction of ball bed voidage) |

In order to investigate the wear, the wear specimens are installed in two of the lifters. These lifters have special location for the specimen placement which was able to protect the specimens. The specimens are mounted in a slot on the top of the lifters they are screwed in their place (Fig. 4). The specimens were made from ductile steel (120 HB). To prevent the overheating and the variation of surface properties, during their production, cold-working processes were used. To improve the surface finishing, the specimens were completely polished. Also, in order to assess the effect of size and shape of the specimens, one of them was chosen with a larger size and another one with a smaller size. Since the thickness and density of the specimens is constant, the mass difference between them can be a suitable criterion for the wear measurement. So, to measure the wear, the mass of specimens is quantified before the test by an accurate scale (GR-200) with the precision of 0.1mg. After the test, the specimens are weighted again. Using the difference between the mass before and after the test, the wear can be obtained. According to Eq. (1), to make the wear independent of surface and density, a parameter called "rate of wear" is used which states the ratio of mass variation to the initial mass in a given time.

$$rate\ of\ wear = \frac{\Delta m}{m_1 \Delta t} \qquad \text{Eq. (1)}$$

The feed of the mill is copper ore smaller than 1 inch, which $F_{80}$ and $F_{50}$ of them are 1/2" and 5/16", respectively. The slurry concentration used in the tests was 60% (mass % solid). The amount of slurry is increased till the slurry volume becomes 1 time of the balls bed voidage. The concept of the slurry filling (U) in the mills was first introduced by Austin et al. [26]. In a pilot mill with 1m diameter, in cascading motion, the ball velocity rapidly approaches 4m/s and it has impacts at high speed in the toe region [14]. The kinetic energy of the balls with 60mm diameter and 0.88kg mass is approximately 7J. The energy of balls to grinding the copper ore feed with dimensions less than 1 inch and the average hardness is enough [27]. The mill grinding mechanism is a combination of both impact and abrasion mechanisms [28].

The experiments will be performed once without the device to prevent cascading motion (to calculate the total wear) and once with the device (to calculate the abrasion wear). The difference in the value of these two tests shows the wear caused by impact. For each experimental condition, the mill is allowed to rotate for 15 minutes, and then the specimens are taken out from the mill to be weighted and eventually the rate of wear is calculated. During the experiments, the slurry temperature was regularly monitored and the changes were observed to be 20-23°C. All experiments are repeated and in order to measure the experimental error, one experiment was repeated three times, and their variability is seen to be within ±0.00002 1/hr at 98% confidence level.

## 3. Results and Discussions

In Fig. 5, contribution of wear due to impact and abrasion for different speeds and ball filling 10% are presented in the wet condition. As Fig. 5 indicated, initially with the increase of speed, the wear increases, then after approaching the peak point, the wear decreases. The pick point relies on the speeds range from 80% to 90% of the critical speed. When the mill speed increases, the shoulder of load moves up, and the falling height of particles is increased in the cascading motion and as a result, the materials which impacted on the toe region with more speed and more energy, leads to the increase of the impact wear. At the speeds higher than 90% of the critical speed, the cascade path is changed due to the lifting of shoulder angle and it moves toward the end of the toe. Therefore, the falling height, impact speed and impact force are lowered. Consequently, the particles and the balls have direct impact on the lifters, but due to the reduction of the speed, the wear caused by the impact is lowered. Moreover, the centrifugal forces are augmented as the speed got increased. As a result, the relative velocity between the materials and the balls increases and consequently this causes the increase of the abrasion wear rate.

Fig. 4. View of the holder liner and samples used in the research.

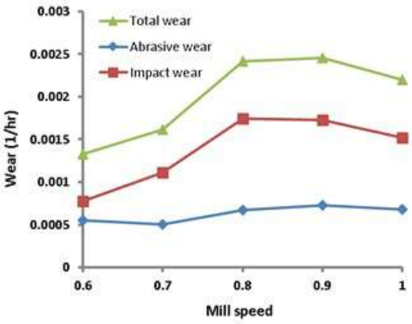

Fig. 5. Contribution of wear due to impact and abrasion at different mill speeds for ball filling 10%.

Figures 6 and 7 show contribution of wear due to impact and abrasion at different mill speeds for ball filling 20% and 30%. As observed from Fig. 5 to Fig. 7, the wear rate reduces when the ball filling increases. When the charge volume is small and the mill speed is high, the balls land upper than load toe and strike the lifters directly which causes the rapid failure and wear of them. With the rise of charge and transmission of the load toe to the top, direct impact between the balls and the mill shell reduces and the balls land on the toe region, consequently the impact wear decreases. With the increase of ball charge, the shoulder angle remains almost constant while the toe height increases, thus, the balls have short falling height and in turn, the wear due to the impact is reduced.

Contribution of impact wear and abrasive wear for different ball filling at 80% of critical speed is depicted in Table 2. According to Table 2, the impact wear decreases remarkably with the increase of the ball filling. When the charge volume is small and the mill speed is high, the balls land upper than load toe and strike the lifters directly which causes the rapid failure and wear of them. With the rise of charge and transmission of the load toe to the top, direct impact between the balls and the mill shell reduces and the balls land on the toe region, consequently, the impact wear decreases. However, with the enhancement of the ball charge, the abrasive wear increases slightly with the increase of normal forces.

## 4. Conclusions

In this study, an experimental method was used to investigate the effects of the mill charge and mill speed on the wear of lifters/liners in wet condition. The wear specimens were installed on the top of lifters in order to compare the mass loss under different conditions. It was found that the mill speed and the ball filling remarkably affect the wear rate of the liner. The following remarks can be drawn from this study:

- As mill charge increases the impact wear rate decreases.
- As mill speed increases to a certain value (about 80-90% of critical speed) the rate of impact wear increases to a peak value and thereafter it decreases.
- The contribution of impact wear and abrasive wear from the total wear depends on the mill speed and ball filling.

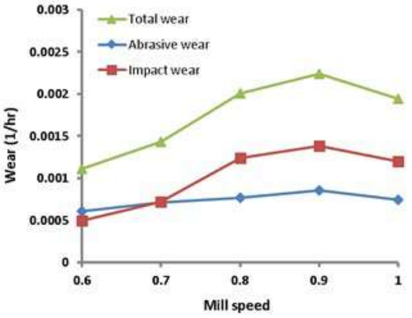

Fig. 6. Contribution of wear due to impact and abrasion at different mill speeds for ball filling 20%.

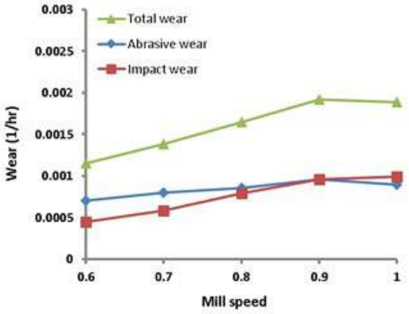

Fig. 7. Contribution of wear due to impact and abrasion at different mill speeds for ball filling 30%.

Table 2. Contribution of impact wear and abrasive wear for different ball filling ($\Phi_C$=0.8, U=1, C=0.6).

| Ball filling | Impact wear | Abrasive wear | Total wear |
|---|---|---|---|
| $J_b$=10% | 0.001747 1/hr<br>72.34% | 0.000668 1/hr<br>27.66% | 0.002415 1/hr<br>100% |
| $J_b$=20% | 0.001240 1/hr<br>61.75% | 0.000768 1/hr<br>38.25% | 0.002008 1/hr<br>100% |
| $J_b$=30% | 0.000795 1/hr<br>48.18% | 0.000855 1/hr<br>51.82% | 0.001650 1/hr<br>100% |

## Acknowledgments

The present work was supported by the NICICO. Special thanks to the generous helps of R&D and the concentrate unit of the NICICO.

## References

[1] R.P. King, Modeling and simulation of mineral processing systems, Elsevier, 2001. books.google.com

[2] B.A. Wills, Mineral processing Technology, Elsevier Science & Technology, Butterworth-Heinemann, 2006.

[3] F.C. Bond, Crushing and Grinding Calculations, Allis Chalmers Mfg. Co., 1961.

[4] P.C. Fazio, Annual Book of ASTM Standards, Wear and Erosion; Metal Corrosion. ASTM G102-89. Standard Practice for Calculation of Corrosion Rates and Related Information from Electrochemical Measurements, ASTM, Philadelphia, 2004.

[5] E. Rabinowicz, Friction and Wear of Materials, New York, John Wiley and Sons, 1995.

[6] S.M. Sehri, H. Ghayour, K. Amini, M.N. Seftejani, H. Rastegari, V. Javaheri, Investigation of wear mechanism in quenched and tempered medium carbon-high chromium martensitic steel using dry sand/rubber wheel, Iron and Steel Society of Iran (ISSI). 12 (2015) 17-23. http://journal.issiran.com/article_18519.html?lang=fa

[7] H. Sharifi, M. Salehi, T. Dallali Isfahani, H. Rafiei Borujeni, Dry Wear Behavior of 42CrMo4 Steel/ZrO2 Composite Prepared by Pressure-Less Infiltration Method, Iron and Steel Society of Iran (ISSI). 13 (2016) 8-14. http://journal.issiran.com/article_20859.html?lang=fa

[8] M.M. Soleymani, M. Fooladi Mahani, M. Rezaeizadeh, Experimental study the impact forces of tumbling mills, Proceedings of the Institution of Mechanical Engineers, Part E: Journal of Process Mechanical Engineering. 231 (2017) 283-293.
https://doi.org/10.1177/0954408915594526

[9] P. Radziszewski, Ball charge dynamics and liner wear simulation, In Canadian Mineral Processors Conference, 1997.

[10] P.W. Cleary, Predicting charge motion, power draw, segregation and wear in ball mills using discrete element methods, Minerals Engineering. 11 (1998) 1061-1080. https://doi.org/10.1016/S0892-6875(98)00093-4

[11] J.T. Kalala, M. Bwalya, M.H. Moys, Discrete element method (DEM) modelling of evolving mill liner profiles due to wear. Part II. Industrial case study, Minerals Engineering. 18 (2005) 1392-1397. https://doi.org/10.1016/j.mineng.2005.02.010

[12] S. Banisi, M. Hadizadeh, 3-D liner wear profile measurement and analysis in industrial SAG mills, Minerals Engineering. 20 (2007) 132-139. https://doi.org/10.1016/j.mineng.2006.07.008

[13] M. Yahyaei, S. Banisi, Spreadsheet-based modeling of liner wear impact on charge motion in tumbling mills, Minerals Engineering. 23 (2010) 1213-1219. https://doi.org/10.1016/j.mineng.2010.08.013

[14] P. Radziszewski, R. Varadi, T. Chenje, L. Santella, A. Sciannamblo, Tumbling mill steel media abrasion wear test development, Minerals Engineering. 18 (2005) 333-341. https://doi.org/10.1016/j.mineng.2004.06.006

[15] M. Rezaeizadeh, M. Fooladi, M.S. Powell, S.H. Mansouri, N.S. Weerasekara, A new predictive model of lifter bar wear in mills, Minerals Engineering. 23 (2010) 1174-1181. https://doi.org/10.1016/j.mineng.2010.07.016

[16] M. Rezaeizadeh, M. Fooladi, M.S. Powell, N.S. Weerasekara, An experimental investigation of the effects of operating parameters on the wear of lifters in tumbling mills, Minerals Engineering. 23 (2010) 558-562. https://doi.org/10.1016/j.mineng.2009.12.010

[17] M. Rezaeizadeh, Investigating the kinematic and Dynamics of Mill Contents with DEM and Experimental Methods, PhD Thesis, Mech. Eng. Dept., Bahonar Un., Kerman, Iran, 2010.

[18] T. Teeri, V.T. Kuokkala, P. Siitonen, P. Kivikytö-Reponen, J. Liimatainen, Impact wear in mineral crushing, Proceedings of the Estonian Academy of Sciences, Engineering, Estonian Academy Publishers, 12 (2006) 408-418. books.google.com

[19] J.T. Kalala, M. Breetzke, M.H. Moys, Study of the influence of liner wear on the load behaviour of an industrial dry tumbling mill using the Discrete Element Method (DEM), International Journal of Mineral Processing. 86 (2008) 33-39. https://doi.org/10.1016/j.minpro.2007.10.001

[20] S. Bird, A.E. Lamb, W. Lamb, D.W. Partrifge, Evolution of sag mill shell liner design at Kennecott Utah copper concentrator, In International Autogenous and Semiautogenous Grinding Technology Conference, 2001.

[21] M. Kendrick, J. Marsden, Candelaria post expansion evolution of SAG mill liner design and milling performance, In International Autogenous and Semiautogenous Grinding Technology Conference, 2001.

[22] M.M. Soleymani, M. Fooladi Mahani, M. Rezaeizadeh, M. Bahiraie, Experimental study of mill speed, charge filling, slurry concentration, and slurry filling on the wear of lifters in tumbling mills, Modares Mechanical Engineering. 15 (2015) 265-271. http://mme.modares.ac.ir/article-15-2812-fa.html

[23] M.M. Soleymani, A. Majidi Jirandehi, A. Arab Solghar, Experimental Study on the Wear of Liner in Tumbling Mill under Dry and Wet Conditions, AUT Journal of Mechanical Engineering. 6 (2022) 331-340. 10.22060/AJME.2022.20778.6017

[24] I.R. Sare, Repeated impact-abrasion of ore-crushing hammers, Wear. 87 (1983), 207-225. https://doi.org/10.1016/0043-1648(83)90035-2

[25] M. Bahiraei, Experimental Study of the impact wear of lifters in SAG mills, M.Sc Thesis, Mech. Eng. Dept., Vali-e-Asr University, Rafsanjan, Iran, 2014.

[26] L.G. Austin, R.R. Klimpel, P.T. Luckie, Process engineering of size reduction: ball milling, American Institute of Mining, Metallurgical, and Petroleum Engineers, 1984.
[27] L.M. Tavares, Breakage of single particles: quasi-static, Handbook of powder technology. 12 (2007) 3-68. https://doi.org/10.1016/S0167-3785(07)12004-2
[28] M.M. Soleymani, Experimental study of operational parameters on product size distribution of tumbling mill, Proceedings of the Institution of Mechanical Engineers, Part E: Journal of Process Mechanical Engineering. (2021) 09544089211062763. https://doi.org/10.1177/09544089211062763

International Journal of ISSI, Vol. 19(2022), No. 2, pp. 66-72

# Analytical and numerical instability analysis of functionally graded low-carbon steel

**K. Amirian [1], Z. Abbasi [2], R. Ebrahimi *[3]**

*[1, 3] Department of Materials Science and Engineering, School of Engineering, Shiraz University, Shiraz, Iran*
*[2] Physics of Nanostructured Materials, Dynamics of Condensed Systems, Faculty of Physics, Vienna University, Vienna, Austria*

## Abstract

The instability point of a material is one of the most important factors when choosing a material, as it could be a good representation of its formability. In this study, the instability of functionally graded materials (FGM) was investigated. An algorithm is proposed for predicting the instability of functionally graded low-carbon steel with gradient work hardening exponent (n) and strength coefficient (K). The investigated work hardening exponent and strength coefficient of the FGM vary through the cross-section as a function of radius. Numerical methods like the Simpson rule of integration were utilized to solve the equations. The mathematical and experimental results are compared, and it can be seen that the algorithm has a reliable consistency with the experimental results. The presented analysis shows that the instability of the functionally graded low-carbon steel can be predicted using the calculation of the average strain hardening exponent. The calculated average work hardening exponent ($\bar{n}$ ) was 0.1095 and 0.1657 for the 550 °C and 650 °C annealed samples, respectively. The instability of more complicated FGMs can be predicted with the present algorithm.

*Keywords:* FGM, Low-carbon steel, work hardening exponent, Strength coefficient, Gradient grain size.

## 1. Introduction

Improvements in material quality are made every day thanks to research and development efforts, but there is still no way to ensure that widely used materials like pure metals, alloys, and standard composites always maintain the essential characteristics required by many different types of machinery and equipment [1,2]. Limitations in using traditional homogenous materials necessitated the creation of new materials with contrasting properties and a graded structure to fulfill the needs of applications caused by technological and industrial progress [3]. This resulted in the development of a new class of materials known as functionally graded materials (FGM).

In recent years, FGMs have gained considerable attention in many engineering applications. FGMs are considered potential structural materials for future high-speed spacecraft, biomedical implants, power generation, and nuclear industries [4]. The phrase "functionally graded material" was originally used in Japan in 1984 to describe the development and use of thermal barrier materials [5]. Conventional FGMs are a novel class of composites with no internal borders or interfacial stress concentrations, resulting in a continuous distribution of microstructure and mechanical characteristics [6]. These materials are also known as sophisticated engineered materials in which the properties are customized and vary smoothly and continuously from one surface to the other [7,8]. In an FGM, the composition and structure gradually

---

*Corresponding author
*Email: ebrahimy@shirazu.ac.ir*
*Address: Department of Materials Science and Engineering, School of Engineering, Shiraz University, Shiraz, Iran*
*1. B.S. student*
*2. Research Assistant*
*3. Professor*

change over volume, providing continuous graded macroscopic properties [9]. The gradual changes should be at least in one direction, which can be in the composition of the material or even its microstructure like grain size or porosity, resulting in at least one functional change in properties, such as hardness, wear resistance, corrosion resistivity, thermal conductivity, or specific heat [9,10].

Because of this smooth, continuous, and gradual transition in mechanical characteristics of FGM, they are better and more attractive than traditional composite materials, which have limitations such as sudden shifts along the composite borders [11]. Interest in FGMs has skyrocketed due to the vast opportunities it presents for producing individualized products well suited for many high-tech sectors. So, there has been a meteoric rise in the previous two decades in the number of scholarly articles covering this topic [11]. The concept of FGM was first developed for heat-resistant materials. Still, these materials have since been utilized to manage deformation, pressure, wear, and corrosion and to lessen stress concentration through a gradual transition across all product dimensions [12]. For example, metal cutting tools may benefit from having a composition gradient designed for the length of use and resistance to wear [13]. Likewise, the longevity and stability of dental implants may be enhanced by adjusting composition gradients and gradient thickness [14]. In the marine industry, FGMs may be utilized to create things like composite pipe systems, sonar domes, and propeller shafts. Due to their high price, FGMs are still not widely employed in the automotive industry. However, FGMs may be used in the production of a variety of car parts, including the combustion chamber, leaf spring, diesel engine piston, etc. [15].

By applying the many possibilities inherent in the FGM concept, it is anticipated that materials will be improved, and new functions for them and new processing solutions will be developed to simplify the process of making them [13]. Several studies have been performed to analyze the behavior of functionally graded plates and shells. Qiu et al.[16] developed an equation to determine the work hardening exponent for ultrafine grain low-carbon steels, resulting in a change in the work hardening exponent (n). Similarly, Sinclair et al. [17] investigated the relationship between work hardening and grain size. Wang et al. [18] used pre-torsion deformation and half an hour of 550 °C - 700 °C thermal annealing to create diverse low-carbon steel samples with grain size distribution.

One of the most important considerations when choosing a material for a particular application is its formability, or how easily it can be shaped while maintaining the desired quality. The capacity to undergo plastic deformation is what this term alludes to [19]. From a metallurgical standpoint, a metal's formability is determined by its elongation, the total amount of strain observed during tensile testing, which is the degree of deformation feasible during a metal-forming process without generating an undesirable condition, such as necking [20]. According to Considère, necking occurs as a consequence of instability in tensile deformation when the sample's cross-sectional area decreases at a faster rate than the material strain hardens, which for homogenous materials Considère approved that instability occurs at true strain equal to the work hardening exponent of the material obtained from the Hollomon equation [19].

Furthermore, in most cases, physical testing, such as tensile or microhardness testing, is required to measure the mechanical properties of materials such as functionally graded ones. This has some problems associated with it. Firstly, when doing most mechanical, the physical sample must be destroyed, which causes extra expenses. Secondly, the only place these tests can provide accurate readings is the exact spot where they are carried out. Because of this, numerical simulation and computation come into play, with which you are not bounded by the limitations of traditional tests.

In this study, an algorithm is driven to examine the instability of materials with grain size distribution along their radius, following a change in work hardening exponent (n) and strength coefficient (K). To confirm our work, we utilized our algorithm on Wang's samples and compared our results. Similar to Qiu et al. [16] the relationship between radius and work hardening exponent was found for the low-carbon steel samples with annealing temperatures of 550 °C and 650 °C. The relation between strength coefficient and radius was also found using the microhardness given for the samples; therefore, the technique was applied to model the low carbon steel specimens using the n and K grain size relations.

## 2. Mathematical procedure

The presented algorithm originated from the expression of force as stress integration on the area where the force is applied. As the considered material is functionally graded, its flow stress will vary with its location (r). Additionally, each point of material during deformation is susceptible to metallurgical changes, and therefore its flow stress will vary over time. Thus, the flow stress can be written as a function of both radius and time as follow:

$$F = \int_0^R \sigma(r,t)dA \qquad \text{Eq. (1)}$$

Where R is the radius of the specimen during deformation. The above equation is also valid for homogenous materials, with the main difference being that the stress is not a function of radius, as it is for the graded one. Furthermore, volume constancy can be used to understand R and the amount of strain as a function of time, as shown in Eqs. (2, 3).

$$R = \frac{R_0}{\sqrt{1 + t\frac{V}{L_0}}} \qquad \text{Eq. (2)}$$

$$\varepsilon = \ln(1 + t\frac{V}{L_0}) \quad \text{Eq. (3)}$$

Where $R_0$ is the initial radius of the tensile test specimen, v is the crosshead speed, and $L_0$ is the initial length of the sample. Moreover, one of the best methods to approximate true stress-true strain curves is the Hollomon equation, as seen in Eq. (4).

$$\sigma = K\varepsilon^n \quad \text{Eq. (4)}$$

Where, as understood, n is the work-hardening exponent, and K is the strength coefficient. For a homogeneous material, both variables are considered constant; however, for a functionally graded material, they can change through cross-section and be a function of radius. Accordingly, with the consideration of the Holloman equation and Eqs. (2-4), Eq. (1) can be rewritten as follow:

$$F = \int_0^{\frac{R_0}{\sqrt{1+t\frac{v}{L_0}}}} K(r)(\ln(1+t\frac{V}{L_0}))^{n(r)} 2\pi r dr \quad \text{Eq. (5)}$$

The numerical computation of the algorithm is based on Eq. (5) and Simpson's integration approach. The algorithm was evaluated on a homogeneous material with the assumption that n and K are constant values before being used for an FGM. For instance, Fig. 1 was plotted using Eq. (5) in the case of a homogenous material with n = 0.3 and K = 100 MPa. The true strain at the maximum force is 0.296, which is very close to what was expected from the Considère criterion [19], that for a homogenous material, necking occurs at a true strain equal to the strain-hardening exponent, which in this case is 0.3. The engineering stress-engineering strain graph shown in Fig. 2 and the true stress-true strain curve presented in Fig. 3 were obtained from the force-displacement data illustrated in Fig. 1 using the classical relationship.

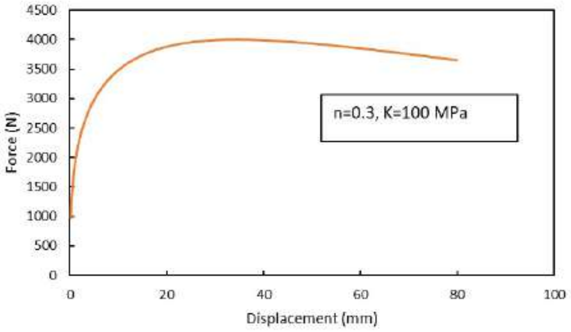

Fig. 1. The numerical force-displacement plot for a homogeneous material with n=0.3 and K=100 MPa.

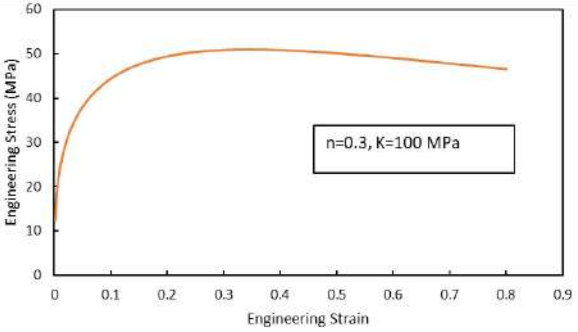

Fig. 2. The numerical engineering stress vs. engineering strain plot for a homogeneous material with n=0.3 and K=100 MPa.

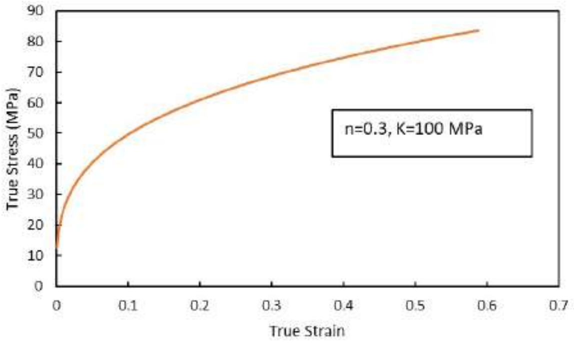

Fig. 3. The numerical and true stress-true strain plot for a homogeneous material with n=0.3 and K=100 MPa.

After the method has been validated for a homogeneous material, it can be applied to functionally graded materials. The data of functionally graded samples that this study was conducted on were adapted from Wang's study [18], in which he annealed the low-carbon steel dog bone samples with gauge dimensions of 5 mm diameter and 70 mm length at 550 °C and 650 °C after utilizing a pre-torsion test. His experiment led to the samples having grain size distributions and microhardness distributions with respect to the radius, as shown in Fig. 4 and Fig. 5, respectively. Moreover, in order to determine the distribution of n and K with respect to position using the indicated radius-to-grain-size relationships from Fig. 4, a similar work to Qui's experiment was utilized. Qui's investigation established Eq. (6) for relating grain size to the work hardening exponent in low-carbon steel.

$$n = 0.307 - 0.439D^{-\frac{1}{2}} \text{ (Qui et al, 2012)} \quad \text{Eq. (6)}$$

As it is understood, considering that each position of the sample has a different grain size and the method utilized by Qui to reach the Eq. (6), the correlation between n and r was found for each sample, as demonstrated in Eq. (7) and (8).

Eq. (7)

$$n = -0.02 * r + 0.18 \quad (550^{\circ}\text{C annealed sample})$$

Eq. (8)

$$n = -0.01 * r + 0.20 \quad (650^{\circ}\text{C annealed sample})$$

Similarly, equations for the strength coefficient can be derived, as will be described subsequently. Vickers hardness is related to stress, which for most materials, its coefficient of relation is 3 [19]. Also, it is known that stress is proportional to the strength coefficient owing to the power law equation, Eq. (4). Therefore, K is proportional to microhardness, and considering the microhardness distribution for the materials observed in Fig. 5, which is a linear relationship, the equation between K and r can be derived as follow, which are also linear:

Eq. (9)

$$K = 6.67 * r + 962 \quad (550^{\circ}\text{C annealed sample})$$

Eq. (10)

$$K = 3.13 * r + 1043 \quad (650^{\circ}\text{C annealed sample})$$

Additionally, an average was taken on the Eqs. (7,8) in order to provide a variable to present a single work-hardening exponent for the gradient materials. As the work-hardening exponents of the functionally graded samples are a function of radius, the average work-hardening exponent can be calculated

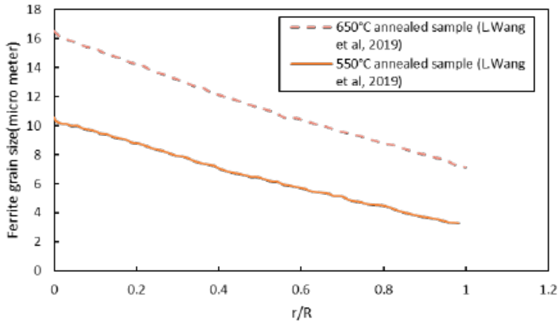

Fig. 4. The ferrite grain size distribution with respect to r/R for samples with 650 °C and 550 °C annealing temperatures. The data for the figure above was extracted from Wang et al. experiment [18].

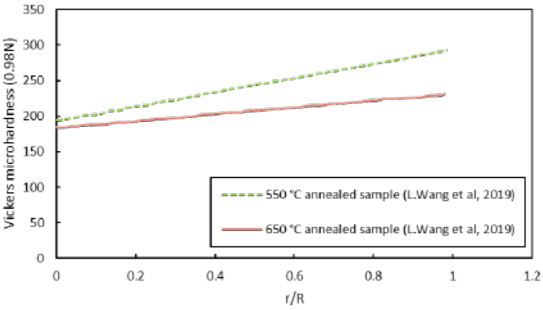

Fig. 5. The Vickers microhardness with respect to r/R for samples with 550 °C and 650 °C annealing temperatures. The data for the figure above was extracted from Wang et al experiment[18].

using Eq. (11).

$$\bar{n} = \frac{\int_A n\,dA}{A} \qquad \text{Eq. (11)}$$

For each sample after replacing Eqs. (7,8) in the above equation, the average work hardening exponent is calculated as follows:

$$\bar{n} = \frac{\int_0^5 2\pi(-0.02*r+0.18)dr}{\pi*5^2} \qquad \text{Eq. (12)}$$

$$(550^{\circ}\text{C annealed sample})$$

$$\bar{n} = \frac{\int_0^5 2\pi(-0.01*r+0.20)dr}{\pi*5^2} \qquad \text{Eq. (13)}$$

$$(650^{\circ}\text{C annealed sample})$$

For the 550 °C and 650 °C samples, $\bar{n}$ is 0.1095 (0.11) and 0.1657 (0.17), respectively. Ultimately, given the equations of K and n as functions of the position, the procedure can be utilized. Wang's experimental findings are compared to the numerical results.

## 3. Results and discussion

The numerical method was solved for the functionally graded samples after it was confirmed by the Considère criterion for a homogenous material with theoretical properties. The numerical algorithm was applied with the consideration of the work hardening exponent and strength coefficient equations of the 550 °C and 650 °C annealed functionally graded low carbon steel samples. The results of the numerical computation were graphed alongside the experimental results of the tensile test in Fig. 6 and Fig. 7. When comparing the experimental and numerical results; it can be seen that the algorithm accurately predicts the samples' behavior until the start of necking for the experimental graphs. After necking, the numerical graphs start to deviate from the experimental ones, which is explained subsequently. For a simulation of an ideal case where no imperfections and occurrence of necking are not considered similar to the presented method, in the beginning, work hardening prevails in the competition between the work hardening rate and the reduction rate of the cross-sectional area. However, the hardening rate decreases during the deformation and gradually falls behind the uniform cross-sectional reduction rate. Therefore, the force required to continue the deformation drops, and a peak can be seen. In a case where localization takes place or necking beings, and the samples are made ideally, with no imperfections, necking occurs, and with the start of necking, strain localizes, and the deformation becomes concentrated, resulting in more increase in the reduction rate of the cross-sectional area than before. This is because the rapid rise in the localized area reduction rate will aid the decrease of the work hardening rate in decreasing the load. Therefore, the reduction of force, in this case, will be more rapid than theoretically expected, which is the reason for a very sharp decrease in force after necking in all experimental graphs of engineering stress vs. engineering strain. Moreover, the peak happens much sooner in the experiment due to the possible presence of the geometrical and metallurgical imperfections, as shown in both experimental graphs in Fig. 6 and Fig. 7.

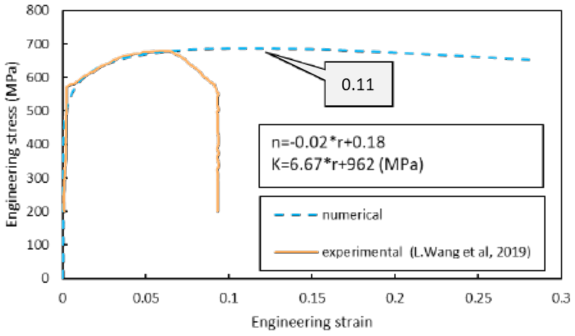

Fig. 6. The calculated engineering stress vs engineering strain for 550 °C annealed sample with $\bar{n} = 0.11$. The experimental data was extracted from [18].

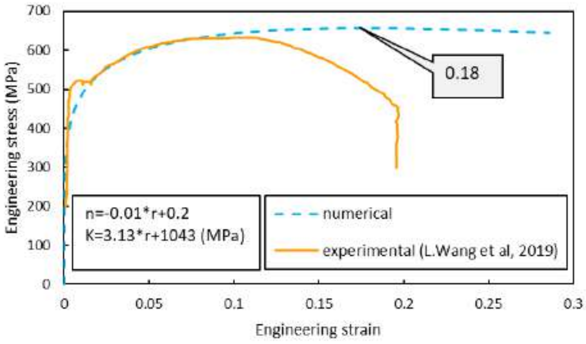

Fig. 7. The calculated engineering stress vs engineering strain for 650 °C annealed sample with $\bar{n} = 0.17$. The experimental result was extracted form [18].

Furthermore, interesting results can be found when comparing the strains at the maximum force in Fig 6 and 7 and the average work hardening exponent, which as calculated above for the 550 °C and 650 °C annealed samples, $\bar{n}$ is 0.1095 and 0.1657 respectively. The true strain at the position where the graphs show a peak for 550 °C and 650 °C annealed samples are 0.1064 and 0.1630, respectively. This demonstrates that the average work-hardening exponent is very close to the ones obtained from the graph, which can be suggested that the simplest way to predict the instability point for FGM is by making an average of n through its area.

## 4. Conclusions

The presented algorithm can be a good simulation of the tensile test behavior for the functionally graded low-carbon steels with gradients n and K through the radius of the tensile test samples. From our investigation, it can be concluded that:

- The mathematical algorithm predicts the point of instability of functionally graded material with good agreement with the Considère criterion and can be a good simulation as the diagrams attained from the algorithm showed similar behavior to the ones obtained from the experiment.
- Numerical analysis showed that instability in FGM could be easily predicted based on the calculation of the average strain hardening exponent, which is equal to the true strain at the onset of necking.
- The mathematical analysis showed that even in a case where necking does not occur, the maximum value of force or, in other words, a peak would be seen in the stress-strain graphs because the reduction of the work hardening rate will fall behind the rate of uniform reduction of area.

## References

[1] B. Saleh, J. Jiang, A. Ma, D. Song, D. Yang, Effect of main parameters on the mechanical and wear behaviour of functionally graded materials by centrifugal casting: A review, Metals and Materials International. 25 (2019) 1395–1409. https://doi.org/10.1007/s12540-019-00273-8.

[2] R. Fathi, A. Ma, B. Saleh, Q. Xu, J. Jiang, Investigation on mechanical properties and wear performance of functionally graded AZ91-SiCp composites via centrifugal casting, Materials Today Communications. 24 (2020). https://doi.org/10.1016/j.mtcomm.2020.101169.

[3] B. Saleh, J. Jiang, R. Fathi, T. Al-hababi, Q. Xu, L. Wang, D. Song, A. Ma, 30 Years of functionally graded materials: An overview of manufacturing methods, applications and future Challenges, Compos B Eng. 201 (2020). https://doi.org/10.1016/j.compositesb.2020.108376.

[4] Y. Miyamoto, W.A. Kaysser, B.H. Rabin, A. Kawasaki, R.G. Ford, Functionally Graded Materials, first ed., Springer US, New York, NY, 1999. https://doi.org/10.1007/978-1-4615-5301-4.

[5] M. Koizumi, FGM activities in Japan, Composites Part B: Engineering. 28( 1997) 1-4. https://doi.org/10.1016/S1359-8368(96)00016-9.

[6] G. Nie, Z. Zhong, Dynamic analysis of multi-directional functionally graded annular plates, Applied Mathematical Modelling. 34 (2010) 608–616. https://doi.org/10.1016/j.apm.2009.06.009.

[7] T.P.D. Rajan, R.M. Pillai, B.C. Pai, Functionally graded Al-Al3Ni in situ intermetallic composites: Fabrication and microstructural characterization, Journal of Alloys and Compounds. 453 (2008). https://doi.org/10.1016/j.jallcom.2006.11.181.

[8] E. Efraim, Accurate formula for determination of natural frequencies of FGM plates basing on frequencies of isotropic plates, Procedia Engineering. 10 (2011) 242–247. https://doi.org/10.1016/j.proeng.2011.04.043.

[9] M. Naebe, K. Shirvanimoghaddam, Functionally graded materials: A review of fabrication and properties, Applied Materials Today. 5 (2016) 223–245. https://doi.org/10.1016/j.apmt.2016.10.001.

[10] S. Kumar Bohidar, R. Sharma, R. Mishra, Functionally graded materials: A critical review, International Journal of Research (IJR). 1 (2014).

[11] M. Sam, R. Jojith, N. Radhika, Progression in manufacturing of functionally graded materials and impact of thermal treatment—A critical review, Journal of Manufacturing Processes. 68 (2021) 1339–1377. https://doi.org/10.1016/j.jmapro.2021.06.062.

[12] R.S. Parihar, S.G. Setti, R.K. Sahu, Recent advances in the manufacturing processes of functionally graded materials: A review, Science and Engineering of Composite Materials. 25 (2018) 309–336. https://doi.org/10.1515/secm-2015-0395.

[13] C.H. Xu, G.Y. Wu, G.C. Xiao, B. Fang, Al2O3/(W,Ti)C/CaF2 multi-component graded self-lubricating ceramic cutting tool material, International Journal of Refractory Metals and Hard Materials. 45 (2014) 125–129. https://doi.org/10.1016/j.ijrmhm.2014.04.006.

[14] P.I. Ichim, X. Hu, J.J. Bazen, W. Yi, Design optimization of a radial functionally graded dental implant, Journal of Biomedical Materials Research Part B: Applied Biomaterials. 104 (2016) 58–66. https://doi.org/10.1002/jbm.b.33345.

[15] P.S. Ghatage, V.R. Kar, P.E. Sudhagar, On the numerical modelling and analysis of multi-directional functionally graded composite structures: A review, Composite Structures. 236 (2020). https://doi.org/10.1016/j.compstruct.2019.111837.

[16] H. Qiu, L.N. Wang, T. Hanamura, S. Torizuka, Prediction of the work-hardening exponent for ultrafine-grained steels, Materials Science and Engineering A. 536 (2012) 269–272. https://doi.org/10.1016/j.msea.2011.11.064.

[17] C.W. Sinclair, W.J. Poole, Y. Bréchet, A model for the grain size dependent work hardening of copper, Scripta Materialia. 55 (2006) 739–742. https://doi.org/10.1016/j.scriptamat.2006.05.018.

[18] L. Wang, B. Li, Y. Shi, G. Huang, W. Song, S. Li, Optimizing mechanical properties of gradi-

ent-structured low-carbon steel by manipulating grain size distribution, Materials Science and Engineering A. 743 (2019) 309–313. https://doi.org/10.1016/j.msea.2018.11.042.

[19] W. F. Hosford, R. M. Caddell, Metal Forming Mechanics and Metallurgy, fourth ed., Cambridge University Press, New York, NY, 2011.

[20] C. V. Nielsen, P.A.F. Martins, Metal Forming: Formability, Simulation, and Tool Design, Elsevier, London, 2021. https://doi.org/10.1016/C2020-0-02428-X.

# The Empirical Test of Steel Price Volatility and Volatility Spillover between Energy (Oil & Gas) and Steel Markets

**S. A. Bahreini [1], H. Badie *[2], F. Ahmadi [3], J. Asadnia [4]**

*[1, 3, 4] Department of Accounting, Qeshm Branch, Islamic Azad University, Qeshm, Iran Tehran, Iran*
*[2] Department of Accounting, Faculty of Economic Science and Accounting, Tehran South Branch, Islamic Azad University, Tehran, Iran*

---

## Abstract

Interdependence of markets may cause fluctuations in one market to positively or negatively affect another market. Therefore, investigating the behavior of fluctuations in financial markets and their causes in financial asset pricing processes, implementation of global risk hedging strategies and asset portfolio preference decision-making is of great importance. Given the importance of this issue, the current research aims to model energy and steel price volatility and experimentally test the spillover of fluctuations between markets using the GARCH BEKK model, during a 10-year period of 2013-2022. The data of the current research were extracted from daily data from the World Data Bank, Coin and Currency Information Site, and Economic and Financial Data Banks; then, using the Dickey-Fuller and Phillips-Perron tests, the significance of the data was evaluated. After that, the spillover effect of fluctuations between the markets was tested using the univariate GARCH and GARCH BEKK tests. The results of the research showed that the steel and energy markets have significant volatility in the studied period. Also, the fluctuations in the oil and gas market are significantly transferred to the global steel price.

*Keywords:* Volatility Spillover, Oil Price, Gas Price, Steel Price.

---

## 1. Introduction

Market volatilities are one of the important and discussed topics in the macroeconomics and capital market field, and researchers in the financial and economic fields have made extensive efforts to study this issue and have conducted numerous studies in this area. These studies often include identifying factors creating fluctuations and the impact of fluctuations and turmoil on different sectors of the market and the economy. Limited research has also been done in the area of intra-market fluctuation spillover in stock markets. The term fluctuation (volatility) in the market refers to extensive and almost unpredictable changes that occur in market indicators for various reasons. The increase in oil prices leads to an increase in production costs and ultimately affects the final price [19]. In addition, the financialization of commodity markets is an important factor that helps the interdependence of various commodities such as metals and energy (such as oil and gas)[48]. Individual and institutional investors may prefer multiple investment instruments to benefit from the return on different investment instruments. Shareholders, when choosing investment instruments to hold in their portfolios, not only consider the return on

---

**Corresponding author*
*Email: badiei@iau.ac.ir*
*Address: Department of Accounting, Faculty of Economic Science and Accounting, Tehran South Branch, Islamic Azad University, Tehran, Iran*
*1. Ph.D. Student*
*2. Assistant professor*
*3. Assistant professor*
*4. Ph.D.*

one asset against another, but also consider the risk of each asset and its ability to protect against risk factors. The prices of goods and the relationships between product prices may affect production, consumption, investment, and savings decisions in economies, the reason for which is the fluctuations in prices, the increase in regions of use of goods, and the observed coordination in price changes. Oil and precious metals are among the most strategic commodities subject to production, consumption, investment, savings, and trade in global markets. Expensive metals such as gold, silver, platinum, and palladium, which have high economic value and have been as important as money throughout history, are now mostly used for industrial purposes or investment. Recently, many shareholders have paid attention to investing in metals due to their sensitivity to oil prices as an economic tool [46].

On the other hand, due to economic relationships between countries and the connections between capital markets, the possibility of the spread of fluctuations from one market to another exists. Some studies have focused on how fluctuations and volatilities from one market enter another. This is particularly evident in times of economic and financial crises. A prominent example of the volatility spillover from one market to another can be seen in the 2007-2008 financial crisis. During this period, severe fluctuations occurred in the US capital markets and their immediate effects were observed in many other countries such as Japan and European countries. According to researchers, these relationships between markets were seen as the volatility spillover, so it can be said that the spread of volatility between financial indicators is indicative of the process of information transfer between markets. Since many financial assets are traded based on gold and oil, it is important for financial market participants to understand the mechanism of transferring fluctuations over time and during these periods [13]. Oil and metal resources, which have high trading volumes in the market, have a high cash flow in the world. Today, capital markets encourage investors, especially during financial crises or financial fluctuations and high uncertainty in traditional securities markets, to turn to commodities and metals [24]. Therefore, including important commodity contracts in the portfolio may have a positive impact on improving financial transactions and extensive investments [17]. In other words, optimal asset allocation is done by optimizing the portfolio, reducing the risk of falling below the expected return, and modeling appropriate temporal correlation between risk hedging, commodity, and securities markets. Metals such as steel may provide a natural and effective hedge against inflation [35]. Therefore, combining commodity investments with other assets may provide better diversification compared to a similar portfolio that does not include commodities [31]. As this commodity drives the economy of many countries, a commodity-based risk hedging strategy may provide greater benefits for international diversification [46]. For this reason, in recent years, with the increase in the prices of strategic commodities such as gold, silver, steel, and other expensive metals, the attention of investors has been drawn to them, and the interest in expensive metals has increased. Therefore, fluctuations in the price of metal commodities are very important due to their potential impact on investment decisions [46].

Given that the steel industry is one of the important, strategic, and infrastructural industries and plays a major role in the development of other industrial and economic sectors of a country, it is expected that changes in energy prices can change the total cost and price of steel products. Therefore, the main issue of this research is whether the energy and steel prices have volatility during the study periods. If so, how is the behavior of price volatility between energy and steel markets? With these explanations, the present study examines the volatility of energy and steel prices and experimentally tests the volatility spillover between these markets. It is natural to expect that prices and volatility between energy and steel markets are related. In addition, the asymmetry of good and bad news in these markets suggests that accepting asymmetric news, both good and bad, in one market, such as the oil and gas market, can strengthen and increase the spillover of risk to the metal market, especially steel. Insufficient research in this regard motivates the researcher to cover some of the research gaps by examining the subject and modeling the volatility of energy and steel prices and the volatility spillover between these markets, and also provide accurate information to investors, managers, analysts, and other stakeholders.

## 2. Theoretical foundations and research backgrounds

The rapid development in commodity markets has led to rapid growth in investment in the past two decades, despite the fact that commodity prices experience significant fluctuations. Worldwide demand growth has been the driving force behind the upward fluctuations observed in commodity prices in recent decades. However, the Global Financial Crisis (GFC) that plunged many world economies into recession also impacted commodity markets significantly. Since investors have to make important choices in the asset allocation process and have increased access to information systems, rapid growth in commodity investment through commodity futures markets has been observed in recent years [5]. Precious metal commodity trading, which is an alternative investment instrument compared to the traditional portfolio containing stocks and bonds, has progressed remarkably in both the cash and derivative markets over the past decade. In this case, the use of commodities like precious metals for diversification in individual investments and hedge funds and other investment funds has increased [17].

Today, energy is one of the major consumptions of households and businesses. Therefore, oil is also considered an important investment instrument for shareholders. Oil price shocks are expected to impact alternative investment instruments and commodity prices due to the relationship between economic growth and financial markets. Economic decision-making units carefully monitor oil prices when deciding to invest. In general, oil price volatility requires close monitoring by market players, as it affects economic activities and stock markets through different channels and can be considered as an alternative investment instrument [46]. Oil is not only an important commodity for all economies but also a determining factor in financial trading. The increase in oil prices directly impacts inflation through increased energy costs. This scenario may limit demand and costs of goods and services, resulting in a decrease in company profits. An increase (decrease) in oil prices leads to a decrease (increase) in demand for oil, which leads to an increase (decrease) in demand for expensive metals and consequently, the price of expensive metals [45]. Therefore, the possibility of using expensive metals as a hedge against inflation increases (Reboredo, 2013). The second factor may be explained by financial investment tendencies and is accompanied by price growth. High oil prices have a negative impact on the economy and hinder growth. As a result, shareholders who are looking for alternative investments tend to choose expensive metals [15]. In this case, the price of oil indirectly affects the price of expensive metals. Oil price shocks (fluctuations) may lead to uncertainty, concerns, and speculative attacks, especially in net oil-importing countries. Therefore, high inflation and inflation expectations increase the tendency to use expensive metals as a hedge, provided that all other goods remain unchanged [39].

In general, there are many approaches to the relationship between strategic commodities. For example, [19] found that the volatility of oil and silver is negatively affected by past oil price shocks. However, they did not find a significant relationship with copper. Also, they showed that precious metal price volatility increased significantly during the second Persian Gulf War. [37] concluded that precious metal prices are not statistically affected by world oil prices. [49] examined the price discovery process between the oil and gold markets and found a positive correlation between oil and gold prices. The results of the linear Granger causality test indicate the existence of a one-way causality from oil prices to gold prices. On the other hand, the lack of causality is determined based on the results of the nonlinear causality test. [30] examined the relationship between oil prices and precious metal prices using unconditional and conditional value at risk methods for the period 2015 to 2000. They found that big downward and upward movements in oil prices have spillover effects on all metal markets and this effect is valid both before and after the GFC. [34] examined the spillover effects of Bitcoin, gold and oil. Based on the results, Bitcoin and gold are safe havens and provide diversification benefits for oil price changes. [35] also investigated the relationship between oil prices and the prices of five different precious metals using the CoVar approach. The results showed that there is spillover from oil prices to precious metal prices. In addition, [24] found evidence in favor of bi-directional returns and volatility spillovers between oil and precious metal prices. They also showed that the magnitude of volatility spillovers increases significantly during periods of financial turmoil.

As mentioned, commodities are considered as separate assets within all classes of assets. It is envisioned that commodity markets are volatile. Therefore, price volatility leads to demand for risk hedging in the commodity market. Producers and consumers often seek ways to hedge risk and commercial risk. In response to this need, derivative markets emerged for commodity risk trading and their use has grown increasingly widespread. The instruments traded in these markets include financial instruments such as futures contracts, options, swaps and physical instruments such as inventories. Futures contracts are among the most important of these instruments and provide substantial information about cash markets and storage. A futures contract is also an agreement to deliver a specified amount of a commodity at a specified date in the future, at a price (the futures price) to be paid at the time of delivery. Future contracts are usually traded on organized exchanges and have a greater tendency towards liquidity compared to future contracts. Besides this, a futures contract differs from a future contract only in that a future contract is "defined in a specified market", meaning that at the end of each trading day there is settlement and transfer of the related funds. The futures market performs several economic functions including the risk hedging function, the price discovery function, the financing function, the liquidity function and price stabilization [36]. Financial market pricing theory states that the efficiency of the market is a function of the speed and extent of information reflected in prices. The rate at which market information is shown is the price at which this type of information is disseminated to market participants [47]. However, in reality, institutional factors such as liquidity, transaction costs and other market constraints may cause an empirical relationship with a lag between price changes in the two markets. Risk transfer and price discovery are two of the major contributions of futures markets in organizing economic activities [43]. Risk transfer refers to the use of futures contracts to transfer price risk to others. Price discovery refers to the use of futures prices to price spot market transactions or price discovery means that the futures price acts as the market's expectations of the next instantaneous price [16]. In other words, price discovery is a process by which markets combine information to reach equilibrium [42]. In the static concept, price discovery means the existence of an equilibrium price and in the dynamic concept, the process of price discovery describes how information is produced and transmitted in markets. In addition, it also transfers information to all market participants. Price discovery is the primary function of a commodity futures market. Information about price discovery is essential because these markets are widely used by companies that produce, market and process commodities. The nature of the price discovery function of futures markets depends on whether new information is initially reflected in futures prices or reflected in spot prices [20]. Conventionally, it is argued that the futures market is the dominant point of price discovery more than the spot market. Multiple studies show that futures markets play an important role in discovering prices for the essential spot market. This price discovery function indicates that prices in futures and spot markets are systematically related in the short term and/or long term [25]. [33] have studied the spillover of fluctuations between oil price, currency price, gold price and stock market under the influence of gaps and structural failure and using BEKK Garch model and ICSS algorithm and have come to the conclusion that the rate change It is done on it. The price of oil has no effect, but it has a significant effect on the price of gold and the stock index.

[48] investigated the predictability of precious metal price volatility with global economic policy uncertainty in the pre-pandemic period and during the COVID era. The results show that there is a significant relationship between global economic policy and precious metal price volatility. It can be inferred that any uncertainty recorded in global economic policy intensifies the volatility of gold, palladium, platinum, and silver prices. [11] examined the contagion of dynamic volatility spillovers between iron ore prices and crude oil prices during the COVID period. Empirical results indicate that: First, the dependence between the Baltic dry index, iron ore prices, and Brent crude oil prices is time-varying and lagged. Second, dynamic dependencies and volatility spillovers between the Baltic dry index, iron ore prices, and Brent crude oil prices have been significantly strengthened during the COVID period, indicating that the impact of market turmoil has strengthened the linkage between markets.[3] studied discernible trends in international metal prices in the presence of unstable volatility. Findings generally show that unpredictable changes in demand, extraction costs, and reserve discoveries affect the slope estimate of this fundamental trend. In addition, low demand and supply elasticities cause high price volatility, making trend estimation difficult. [44] tested oil resource price volatility in identifying barriers to economic recovery. Based on the Granger causality test, impulse response functions and variance decomposition, economic recovery and investment have been significantly impacted by oil price volatility from Q1 2000 to Q4 2020. Based on this research, commercial investment and oil price have demonstrated high power throughout the international economic crisis. Given the recent spread of COVID-19, volatility in economic activities and oil prices is expected during this crisis. In addition, during the GFC and the COVID-19 crisis, oil prices and economic growth are highly correlated. [18] examined the predictability of oil price volatility based on global economic conditions. [40] examined oil price shocks and return and volatility spillovers between base and precious metals. The findings show that demand shocks and risk-receiving (sending) shocks are the dominant shocks from (to) metal returns. Net return directionality and volatility comovement indicate that some metals like tin, gold and even nickel, lead, and aluminum appear as net senders at least over some intervals of the sample period under analysis.

[14] investigated the transmission of fluctuations among precious metals, energy, and stocks during the COVID-19 pandemic. The main findings show a significant impact of the pandemic on the links between market fluctuations, as the correlation between different asset fluctuations reached its peak during the outbreak. [46] tested the time-varying fluctuations between the prices of oil and precious metals. The empirical results indicate a causal relationship between the average of the oil return series and the precious metal return series. The causality test of average indicates that the oil price is the Granger cause of all precious metals. [13] examined the commodity markets of energy and non-energy based on the spillovers of fluctuations and the effectiveness of risk hedging. The results showed that the oil market transmits fluctuations to the metal and overall non-energy markets.[12] studied the asymmetric relationship between the price of oil and the COVID-19 pandemic with the value of trading on the stock exchange. The results showed that in the long run, the increase in oil prices has a significant asymmetric effect on the value of trading on the stock exchange. On the other hand, in the short term, the number of COVID-19 patients has a positive but insignificant relationship, while the coronavirus media index has a negative and significant relationship with the value of trading on the stock exchange. [32] investigated the role of fundamental factors in the global oil price. The results showed that in the estimation pattern, world GDP has the most significant impact with a demand elasticity of 0.6039, while world military and security tensions have the least impact with a demand elasticity of 0.0110. [5] examined the impact of the coronavirus on the global oil and gas market and its prospects for the future. The results of this study suggest reduction of OPEC production and prevention of price collapse, which weaken the global economy, or maintenance of stable production and acceptance of the risk of price collapse.

[41] investigated the decomposition of crude oil prices and its impact on the return of selected stock price indices using the VECM method. The results of this study showed that positive price fluctuations affect the return of stock indices of all three groups, and have the greatest impact in order on the return of stock indices of the petroleum coke and nuclear fuel products group, oil and gas extraction and ancillary services excluding exploration group, and rubber and plastics group; while negative price fluctuations only affect the return of stock index of the oil and gas extraction and ancillary services excluding exploration group. With regard to the test of instantaneous response of all three groups of stock index returns to the positive shock in the model, the result showed that there is a dynamic response in all three groups of stock index returns to the positive shock of the two variables of positive and negative fluctuations in oil prices, so that it has a positive effect on the return of the stock index of the petroleum coke and nuclear fuel products group; but in the other two stock index return groups, a negative effect is observed. In a study by [4], the regional gas prices were examined in relation to crude oil prices in the global market. The findings showed a high level of susceptibility of regional gas and oil prices to market fluctuations in Asia and Europe due to their interdependence. However, in the American market, particularly in the shale oil sector, this relationship was not observed due to excess energy supply. In another study by [27], the response of natural gas prices to changes in crude oil prices in the European and Asian regional gas markets was investigated. The results showed that the crude oil price had a direct or inverse effect on the natural gas price in different regimes. In Europe, the first crude oil price interruption had an inverse effect for one month and a direct effect for 18 months and the second crude oil price interruption had a direct effect on natural gas prices in both regimes. In Asia, the effect of crude oil prices on natural gas prices was direct in both regimes, with prices of 28 months in regime one and 26 months in regime two. [27] conducted a study to examine the response of natural gas prices to changes in crude oil prices in regional gas markets in Europe and America. The results show that the oil price directly affects gas prices in some regimes and has an inverse effect in other regimes. In Europe, oil price shocks have had a reverse effect for one month and a direct effect for 16 months on gas prices. In this region, the second oil price shock has had a direct impact on gas prices in both regimes. In America, the first oil price shocks for 2 months and the second oil price shocks for 18 months have had a direct impact on gas prices. Furthermore, the Granger causality test shows the causality is from oil price to gas price. [33] investigated the volatility of oil, currency, gold and stock markets using BEKK bivariate GARCH model and Granger causality test. The results of their research showed that the fluctuations in the oil market can spread to the stock market of the supplying countries. Also, exchange rate fluctuations have a significant effect on the price of gold and the stock index of the studied countries. In another study by [8], the relationship between natural gas prices and crude oil prices in the global gas markets was examined. The results showed that although the long-term relationship between gas and oil prices in the American market has been separated, it still exists in the UK, Europe, and Asia, and a high percentage of gas price fluctuations are explained by oil price shocks.

## 3. Research Method

The present study is applied in terms of its objectives, and descriptive and exploratory in terms of its methodology. In this research, a library method was used to investigate the theoretical literature and collect the statistical data. It should be noted that the statistical information related to daily data during the 10-year period of 2013-2022 was extracted from the World Bank database[1], the Economic and Financial Database[2] , and the Coin and Currency Information website[3] , which includes daily energy prices (oil and gas) and the performance of steel companies in the Tehran Stock Exchange. The spillover effect of fluctuations between these markets was tested using the bivariate GARCH models and the diagonal BEKK model. The statistical population of this study includes oil and gas prices and the performance of steel industries. Accordingly, the information related to the 10-year period was selected in the relevant sections and examined and tested as the sample of the study.

*BEKK Model*

Another type of multivariate GARCH model called "Diagonal BEKK" has been proposed as an extension of the MGARCH model. Its most important feature is its generality, and one of its other features is that its conditional variances and covariances of this time series affect each other and it estimates fewer parameters than other methods. This method allows for the examination of the impact of shocks and disturbances in one series on the disturbances of another series. This effect can be symmetric or asymmetric.

The BEKK specification is as follows:

$$H_t = \acute{C}C + A\acute{\acute{\varepsilon}}_{t-1}\varepsilon_{t-1}A + \acute{B}H_{t-1}B \qquad \text{Eq. (1)}$$

Base on [33], Parameter estimation for the multivariate Generalized Autoregressive Conditional Heteroskedasticity (GARCH) model can be performed using the maximum likelihood estimation method. The logarithm of the likelihood function is expressed

---

1. https://data.worldbank.org/
2. https://databank.mefa.ir/
3. https://www.tgju.org/

as follows:

Eq. (2)

$$L(\theta) = T \log 2\pi - 0.5 \sum_{t-1}^{T} \log|H_t(\theta)| - 0.5 \sum_{t-1}^{T} \varepsilon_t\,(\acute{\theta}) \log H_t^{-1}\,\varepsilon_t(\theta)$$

Where, T is the number of observations and θ is the vector of parameters to be estimated. The maximum likelihood estimation algorithm proposed by [10] is used to estimate the parameters. As previously mentioned, the drawback of conventional multivariate GARCH models is that they assume no structural breaks in the volatility process, but financial time series are subject to sudden changes and thus, structural breaks in volatility are likely to occur. Ignoring these breaks may lead to false results regarding the transmission of information and spillover of fluctuations between financial markets.

### 3.1. Research Model

In this study, the first and second hypotheses are examined using univariate GARCH, and the following model is used to test the third hypothesis. It should be noted that the following model is also applicable to the first and second hypotheses, but oil and gas prices are separated for analysis.

Eq. (3)

$$Steel_{it} = \alpha_0 + \beta_1 Oil_{it} + \beta_2 Gas_{it} + \varepsilon_{i,t}$$

### 3.2. Research Variables

The research variables include global energy prices, which consist of daily global oil and gas prices (independent variable).

Global oil prices (Oil): which are extracted daily from the World Bank database and global economic and financial databases, and their logarithm is taken. Each barrel is calculated in US dollars.

Global gas prices (Gas): are extracted daily from the Coin and Currency Information website and global databases, and their logarithm is taken and calculated in US dollars.

The dependent variable is global steel prices.

Global steel prices (Steel): which are extracted daily from the Coin and Currency Information website and global databases, and its logarithm is taken. It should be noted that each ton of steel is calculated in US dollars.

### 3.3. Research Hypotheses

H1: The energy market experiences volatility during the study period.

H2: The steel price experiences volatility during the study period.

H3: There is a spillover effect of fluctuations from oil and gas prices to steel prices.

### 3.4. Descriptive Statistics

Descriptive statistics for the variables used in this study are summarized in Table 1. The table shows the mean, median, maximum, minimum, standard deviation, kurtosis, skewness, and Jarque-Bera statistic and probability, respectively. As seen in Table 1, the standard deviation specified for the variables indicates that there has been high volatility in these markets. Since the kurtosis is greater than 0.05, the variables have platykurtic distributions, and their skewness is also shorter than the normal limit. Furthermore, the Jarque-Bera test statistics reject the normality assumption of the research variables at a 95% significance level, as the p-value is less than 0.05.

As seen in the above table, the average price of oil during the study period was $68.28, which has experienced one of the highest price trends. The price of oil during this period increased to over $104.83 and experienced a minimum price on the border of $44.49. Therefore, it can be concluded that we have witnessed significant changes and volatility in its price during the study period. Additionally, the results of examining gas prices during the study period show that it was equal to 3.405, with the maximum value being 6.149 and the minimum value being 1.639 units. As observed, the average global steel price during the study period was 14.06 units, with the maximum and minimum values being 14.34 units and 11.79 units, respectively.

### 3.5. Data Stationarity Analysis

In time series data, it is essential to examine whether the data is stationary. Therefore, before estimating and predicting research models, data stationarity should be investigated.

Table 1. descriptive statistics.

| Variable | Mean | Median | Max. | Min. | SD | Kurtosis | Skewness |
|---|---|---|---|---|---|---|---|
| Oil | 68.28 | 65.76 | 104.83 | 44.49 | 20.97 | 0.1524 | 1.6648 |
| Gas | 3.4058 | 3.2630 | 6.1490 | 1.6390 | 0.8222 | 0.4541 | 2.7514 |
| Steel | 14.06 | 14.24 | 14.34 | 11.79 | 13.14 | 1.4890- | 3.7424 |

Table 2. Stationarity of Variables - Dickey-Fuller.

| Variables | Status | Interception without trend | | | | | Interception with trend | | | | |
|---|---|---|---|---|---|---|---|---|---|---|---|
| | | T-statistics | Critical values | | | Prob. | T-statistics | Critical values | | | Prob. |
| | | | 1% | 5% | 10% | | | 1% | 5% | 10% | |
| Gas | Level | -3.4332 | -3.4325 | -2.8623 | -2.5672 | 0.0100 | -3.9600 | -3.9613 | -3.4114 | -3.1275 | 0.0100 |
| | 1st order differential | -25.753 | -3.4325 | -2.8623 | -2.5672 | 0.0000 | -23.854 | -3.4325 | -2.8623 | -2.5672 | 0.0000 |
| Oil | Level | -0.2415 | -2.5657 | -1.9409 | -1.6166 | 0.5994 | -1.6686 | -3.4325 | -2.8623 | -2.5672 | 0.4472 |
| | 1st order differential | -54.663 | -2.5657 | -2.1501 | -1.9820 | 0.0001 | -20.904 | -2.5658 | -1.9409 | -1.6166 | 0.0000 |
| Steel | Level | -0.9199 | -2.5657 | -1.9409 | -1.7246 | 0.3180 | -1.3355 | -3.9613 | -3.4114 | -3.1275 | 0.8787 |
| | 1st order differential | -52.554 | -2.5657 | -1.9409 | -1.7246 | 0.0001 | -21.945 | -2.5658 | -1.9409 | -1.6166 | 0.0000 |

Table 3. Stationarity of Variables - Phillips-Perron test.

| Variables | Status | Interception without trend | | | | | Interception with trend | | | | |
|---|---|---|---|---|---|---|---|---|---|---|---|
| | | T-statistics | Critical values | | | Prob. | T-statistics | Critical values | | | Prob. |
| | | | 1% | 5% | 10% | | | 1% | 5% | 10% | |
| Gas | Level | -3.8340 | -3.4325 | -2.8623 | -2.5672 | 0.0026 | -1.58752 | -2.56579 | -1.94093 | -1.61662 | 0.1059 |
| | 1st order differential | -60.378 | -3.4325 | -2.8623 | -2.5672 | 0.0000 | -60.369 | -2.56579 | -1.94093 | -1.61662 | 0.0001 |
| Oil | Level | -07958 | -3.4324 | -2.8623 | -2.5672 | 0.8197 | -2.0787 | -3.96124 | -3.4113 | -3.1275 | 0.5569 |
| | 1st order differential | -55.007 | -3.4324 | -2.8623 | -2.5672 | 0.0001 | -55.055 | -3.96124 | -3.4113 | -3.1275 | 0.0000 |
| Steel | Level | -0.5646 | -3.4324 | -2.8623 | -2.5672 | 0.8758 | -2.8837 | -3.96124 | -3.4113 | -3.1275 | 0.2901 |
| | 1st order differential | -53.537 | -3.4324 | -2.8623 | -2.5672 | 0.0001 | -53.537 | -3.96124 | -2.7623 | -2.6672 | 0.0000 |

The results of the Dickey-Fuller and Phillips-Perron tests show that in both cases, the level of significance (probability) in the level test had values greater than 0.05. Therefore, the null hypothesis of data stationarity is rejected, but with one order of differencing, the level of significance changes, and stationarity is established.

**Results of H1: The energy market experiences volatility during the study period.**

The results of the univariate GARCH test for examining the first hypothesis are presented in tables 4 and 5.

The results of the volatility test in the energy market during the study period are presented in tables 4 and 5. Based on the Z statistic and its probability in the GARCH model, the results indicate that there are fluctuations and volatility spillover in the energy market (oil and gas). Therefore, it can be concluded that there is volatility in the energy market (oil and gas) during the study period.

**Results of H2: The steel price experiences volatility during the study period.**

The results of the volatility test in the global steel market are presented in table 6. Based on the Z statistic and its probability in the univariate GARCH model, the results indicate that there are fluctuations and volatility spillover in the global steel market. Therefore, it can be concluded that there is volatility and fluctuation in the steel market during the study period, and this hypothesis is confirmed.

**Results of H3: There is a spillover effect of fluctuations from oil and gas prices to steel prices.**

The results of the spillover effect of energy prices (oil and gas) on global steel prices using the diagonal BEKK GARCH model are presented in tables 7 and 8.

The results of the spillover effect of gas prices on global steel prices using the diagonal BEKK GARCH model are presented in table 7. In this test, if the level of significance for each variable is less than 0.05 and the test statistic is outside the range of ±1.96, it can be claimed that the changes in gas prices have a significant effect on steel prices. The corresponding values in row M (1,2) show the results of the spillover effect test of gas on global steel prices. As seen, the significance level of the test for gas prices on global steel prices is 0.0000, and the test statistic is Z=5.3165. Therefore, it can be claimed that spillover effects of gas prices on global steel prices exist.

Table 4. Gas market fluctuations using the univariate GARCH model.

| Description | Variables | Coefficient | Z-statistics | Sig. level |
|---|---|---|---|---|
| Global Gas Prices | c | 1.500105 | 4.214895 | 0.0000 |
| | RESID(-1)^2 | 0.111719 | 17.70960 | 0.0000 |
| | GARCH(-1) | 0.894483 | 205.8461 | 0.0000 |

Reference: research findings

Table 5. Oil market fluctuations using the univariate GARCH model.

| Description | Variables | Coefficient | Z-statistics | Sig. level |
|---|---|---|---|---|
| Global Oil Prices | c | 0.5406 | 2.781317 | 0.4346 |
| | RESID(-1)^2 | 3.5548 | 88.1902 | 0.0000 |
| | GARCH(-1) | 0.3115 | 68.0158 | 0.0000 |

Reference: research findings

Table 6. Steel market fluctuations using the univariate GARCH model.

| Description | Variables | Coefficient | Z-statistics | Sig. level |
|---|---|---|---|---|
| Global Steel Prices | c | 3.12895 | 0.781510- | 0.2173 |
| | RESID(-1)^2 | 4.15202 | 75.1022 | 0.0000 |
| | GARCH(-1) | 0.2415 | 60.1543 | 0.0000 |

Reference: research findings

Table 7. The effect of gas price fluctuations on the global steel price using the diagonal BEKK model.

| Description | Variables | Coefficient | Z-statistics | Sig. level |
|---|---|---|---|---|
| Global Gas Prices | M(1,1) | 1.053205 | 5.692242 | 0.0000 |
| | M(1,2) | 2.633210 | 5.316506 | 0.0000 |

Reference: research findings

Table 8. The effect of oil price fluctuations on the global steel price using the diagonal BEKK model.

| Description | Variables | Coefficient | Z-statistics | Sig. level |
|---|---|---|---|---|
| Global Oil Prices | M(1,1) | 1.663794 | 6.038197 | 0.0000 |
| | M(1,2) | 0.936023 | 4.22156 | 0.0000 |

Reference: research findings

The results of the spillover effect of oil prices on global steel prices using the diagonal BEKK GARCH model are presented in table 8. In this test, if the level of significance for each variable is less than 0.05 and the test statistic is outside the range of ±1.96, it can be claimed that the changes in oil prices have a significant effect on steel prices. The corresponding values in row M (1,2) show the results of the spillover effect test of oil on global steel prices. As seen, the significance level of the test for oil prices on global steel prices is 0.0000, and the test statistic is Z=4.2215. Therefore, it can be claimed that spillover effects of oil prices on global steel prices exist. Thus, according to the results of the tables, a significant relationship can be observed between the energy price and the global steel price using the diagonal BEKK GARCH model.

## 4. Conclusions

The steel industry is considered one of the most important foundational and primary industries in the world, providing the basis for the creation and development of many other industries and activities. Today, over 1 billion tons of steel are produced annually worldwide, with the majority being produced in China and some other Asian countries. Steel industry products have a wide range of applications in various industries and sectors, and any changes in their supply and demand, quality, and price quickly affect other industrial and economic activities. On the other hand, energy (especially gas and oil) is a very important and influential factor in the production process and the final cost of these products. The energy required for different sectors and processes of production, transportation, and conversion of steel products is supplied from fossil fuels, especially gas and oil, and due to the huge energy consumption in these products, the possibility of replacing or using other energy sources has not yet been possible. The energy market, especially oil and gas, is constantly changing under the influence of global economic conditions and sometimes experiences turbulence in prices and, as a result, changes in supply and demand. The spread of volatility between financial indicators indicates the process of transferring information between markets. Despite the relationship between financial markets, information created in one market can also affect other markets. In this research, the daily data related to the price of energy (oil and gas) and the global price of steel in the 10-year period ending at the end of 2022 was collected and analyzed using GARCH and Granger causality models. The research findings indicate that the global price of energy (oil and gas) can have a significant effect on the price of steel in the market. Part of this effect can be related to the role of energy prices in the cost of steel industry products. Therefore, the fluctuation in the energy market, based on this study, spreads to the global steel market. This claim is strengthened based on some past researches. Given the high level of uncertainty and the nature of market fluctuations in today's world, adopting effective risk management strategies and risk hedging opportunities is essential. Risk hedging opportunities provide better conditions for investors to maintain an optimal portfolio, while also reducing portfolio risk. The variable coverage ratios over time show that investors need to constantly adjust their hedging strategies. In terms of policy implications, findings of this study provide valuable insights for investors, policymakers, and portfolio managers. With the increase in integration, regulators need to carefully monitor systemic financial risks and act carefully when observing market movements. Policymakers are recommended to promote financial liberalization reforms in commodity markets to strengthen the transfer of information. Given the evidence of volatility in the energy (oil and gas) and steel markets, analysts in the capital markets, commodity and energy exchanges, and other stakeholders are suggested to monitor periods of volatility in these markets and consider them in their decisions and analyses.

## References

[1] W.S. Abanomey, I. Mathur, International Portfolios with Commodity Futures and Currency Forward Contracts, The Journal of Investing. 10 (2001) 61–68.

[2] A. Abdalisousan, M. Khalatbari, S.E. Zaker, N. Heidari, M.A. Tavana, M.R. Gharehdaghi, The Impact of the Corona Virus on the Global Oil and Gas Market and Its Future Prospects, Sustainability, Development & Environment. 2 (n.d.) 61–83.

[3] T. Addison, A. Ghoshray, Discerning trends in international metal prices in the presence of nonstationary volatility, Resource and Energy Economics. 71 (2023) 101334.

[4] A. AghiliMoghaddam, E. Abbassi, S. Nessabian, M. Damankeshideh. The effects of crude oil prices in the world market on regional prices of gas, Vector Error Correction approach. Economic Modelling, (2020)-14(49): 89-110. doi: 10.30495/eco.2020.674205.

[5] A.D. Ahmed, R. Huo, Volatility transmissions across international oil market, commodity futures and stock markets: Empirical evidence from China, Energy Economics. 93 (2021) 104741.

[6] P. Andreasson, S. Bekiros, D.K. Nguyen, G.S. Uddin, Impact of speculation and economic uncertainty on commodity markets, International Review of Financial Analysis. 43 (2016) 115–127. .

[7] J.A. Batten, C. Ciner, B.M. Lucey, The macroeconomic determinants of volatility in precious metals markets, Resources Policy. 35 (2010) 65–71.

[8] D. Behboudi, H. Asgharpour, K.N. Oskoui, 02 The Relationship Between Natural Gas And Oil Prices in Regional Gas Markets, Journal of Energy Planning And Policy Research. 2 (2016) 29–59.

[9] J. Bernard, L. Khalaf, M. Kichian, S. Mcmahon, Forecasting commodity prices: GARCH, jumps, and mean reversion, Journal of Forecasting. 27 (2008) 279–291.

[10] MM. Brent, II. Oster. Nutritional substitution: a new approach to microbial control for Drosophila cultures. Dro Inf Ser. (1974) 155-157.

[11] Y. Chen, J. Xu, J. Miao, Dynamic volatility contagion across the Baltic dry index, iron ore price and crude oil price under the COVID-19: A copula-VAR-BEKK-GARCH-X approach, Resources Policy. 81 (2023) 103296.

[12] M. Dadgar. V. Varahrami, Investigating the Asymmetric Relationship between Oil Price and the Covid-19 Pandemic with Trading Value on the Stock Exchange. Journal of Investment Knowledge, 2023; 12(47): 191-216.

[13] A. Dutta, M. Hasib Noor, Oil and non-energy commodity markets: An empirical analysis of volatility spillovers and hedging effectiveness, Cogent Economics &amp; Finance. 5 (2017) 1324555.

[14] S. Farid, G.M. Kayani, M.A. Naeem, S.J.H. Shahzad, Intraday volatility transmission among precious metals, energy and stocks during the COVID-19 pandemic, Resources Policy. 72 (2021) 102101.

[15] F.T.F.& R. Ingenito, Economic Review, Economic Review. (1996) 27–47.

[16] K.D. Garbade, W.L. Silber. Dominant satellite relationship between live cattle cash and futures markets. The Journal of Futures Markets.(1983) 123- 136.

[17] S. Gazel, Değerli Metaller ve Makroekonomik Değişkenler: Türkiye İçin Bir Fourier Eşbütünleşme Testi Uygulaması, Yönetim ve Ekonomi Dergisi. 25 (2018) 527–542.

[18] Y. Guo, F. Ma, H. Li, X. Lai, Oil price volatility predictability based on global economic conditions, International Review of Financial Analysis. 82 (2022) 102195.

[19] S. Hammoudeh, Y. Yuan, Metal volatility in presence of oil and interest rate shocks, Energy Economics. 30 (2008) 606–620.

[20] G. Wright Hoffman, Factors Affecting Prices on Organized Commodity Markets1, The ANNALS of the American Academy of Political and Social Science. 155 (1931) 91–99.

[21] https://data.worldbank.org/

[22] https://databank.mefa.ir/

[23] https://www.tgju.org/

[24] S.H. Kang, R. McIver, S.-M. Yoon, Dynamic spillover effects among crude oil, precious metal, and agricultural commodity futures markets, Energy Economics. 62 (2017) 19–32.

[25] M. Kumar Mahalik, D. Acharya, M. Suresh Babu, Price discovery and volatility spillovers in futures and spot commodity markets, Journal of Advances in Management Research. 11 (2014) 211–226.

[26] T. Mohamadi, A. R. Ghasemi, A. Nekounam, The Reaction of the Natural Gas Price to the Changes of the Crude Oil Price in Europe and Asia Regional Markets: MSVAR Approach. Iranian Energy Economics, 2018; 7(27): 1-30. doi: 10.22054/jiee.(2018) 9135.

[27] T. Mohammadi, A. Ghasemi, M. Asali, &, A. Nekonam. The Reaction of the Natural Gas Price to the Changes of the Crude Oil Price in Europe and American Regional Gas Markets: MSVAR Approach. Quarterely Energy Economics Review. 2018;14(58), 1-26.

[28] S.A. Raza, A. Masood, R. Benkraiem, C. Urom, Forecasting the volatility of precious metals prices with global economic policy uncertainty in pre and during the COVID-19 period: Novel evidence from the GARCH-MIDAS approach, Energy Economics. 120 (2023) 106591.

[29] J.C. Reboredo, Is gold a hedge or safe haven against oil price movements?, Resources Policy. 38 (2013) 130–137.

[30] J.C. Reboredo, A. Ugolini, The impact of downward/upward oil price movements on metal prices, Resources Policy. 49 (2016) 129–141.

[31] P. Sadorsky, Modeling volatility and correlations between emerging market stock prices and the prices of copper, oil and wheat, Energy Economics. 43 (2014) 72–81.

[32] N. Salek, M. Khorsandi, A. Faridzad, A.R. Ghasemi, T. Mohammadi, Evaluate the Fundamental Factors on the World Oil Price, Quarterly Energy Economics Review. 18 (2022) 35–82.

[33] E. sefidbakht, M.H. Ranjbar. Volatility Spillover between Oil Price, Exchange Rates, Gold Price and Stock Market Indexes with Structural Breaks. Financial Engineering and Portfolio Management, (2017)- 8(33):51-87.

[34] R. Selmi, W. Mensi, S. Hammoudeh, J. Bouoiyour, Is Bitcoin a hedge, a safe haven or a diversifier for oil price movements? A comparison with gold, Energy Economics. 74 (2018) 787–801.

[35] S.J.H. Shahzad, M.U. Rehman, R. Jammazi, Spillovers from oil to precious metals: Quantile approaches, Resources Policy. 61 (2019) 508–521.

[36] G. Skiadopoulos, Investing in commodities: Popular beliefs and misconceptions, Journal of Asset Management. 13 (2011) 77–83.

[37] U. Soytas, R. Sari, S. Hammoudeh, E. Hacihasanoglu, World oil prices, precious metal prices and macroeconomy in Turkey, Energy Policy. 37 (2009) 5557–5566.

[38] L. Spierdijk, Z. Umar, Are Commodities a Good Hedge Against Inflation? A Comparative Approach, SSRN Electronic Journal. (2010).

[39] S. Ks, R. Kumar. Study on dynamic relationship among gold price, oil price, exchange rate and stock market returns. International journal of applied business and economic research. (2011)- 9(2):145–165.

[40] Z. Umar, F. Jareño, A. Escribano, Oil price shocks and the return and volatility spillover between industrial and precious metals, Energy Economics. 99 (2021)

105291.
[41] V. Varharami, M. J. Moradalian. Decomposition Crude Oil Price and its Impact on the Efficiency of Selected Stock Price Index with VECM. Financial Economics, (2021)-15(55): 313-332.
[42] H. Working, Theory of the Inverse Carrying Charge in Futures Markets, Journal of Farm Economics. 30 (1948) 1.
[43] H. Working, "New Concepts Concerning Futures Markets and Prices," American Economic Review, Vol. 52, 1962. - References, Scientific Research Publishing. (n.d.).
[44] X. Xiuzhen, W. Zheng, M. Umair, Testing the fluctuations of oil resource price volatility: A hurdle for economic recovery, Resources Policy. 79 (2022) 102982.
[45] S. Yapraklı, F. Kaplan, Petrol Fiyatlarının Altın Fiyatları Üzerindeki Doğrudan ve Dolaylı Etkileri: Ekonometrik Bir Araştırma, Ekonomi Bilimleri Dergisi. 10 (2017.) 50–69.
[46] D.Ç. Yıldırım, E.I. Cevik, Ö. Esen, Time-varying volatility spillovers between oil prices and precious metal prices, Resources Policy. 68 (2020) 101783.
[47] H.O. Zapata, T.R. Fortenbery, D. Armstrong, Price Discovery in the World Sugar Futures and Cash Markets: Implications for the Dominican Republic, AgEcon Search. (2005) 12657.
[48] A. Zaremba, Z. Umar, M. Mikutowski, Commodity financialisation and price co-movement: Lessons from two centuries of evidence, Finance Research Letters. 38 (2021) 101492.
[49] Y.-J. Zhang, Y.-M. Wei, The crude oil market and the gold market: Evidence for cointegration, causality and price discovery, Resources Policy. 35 (2010) 168–177.

# Guide for Preparation of Manuscript

**International Journal of Iron & Steel Society of Iran (IJISSI)** is published semiannually by Iron and Steel Society of Iran (ISSI) with collaboration of Isfahan University of Technology (IUT). Original contributions are invited from worldwide ISSI members and non-members.

**1. Submission of manuscript:** This instruction gives you guidelines for preparing papers for IJISSI. Manuscripts should not be submitted if they have already been published or accepted for publication elsewhere. The full text of the paper including text, references, list of captions, tables, and figures should be submitted online and you will be guided stepwise through the creation and uploading of your files. The system automatically converts source files to a single PDF file of the article, which is used in the peer-review process. Please note that even though manuscript source files are converted to PDF files at submission for the review process, these source files are needed for further processing after acceptance. All correspondence, including notification of the Editor's decision and requests for revision, takes place by e-mail removing the need for a paper trail.

**2. Category**

**i) Research paper (maximum of ten printed pages):** An original article that presents a significant extension of knowledge or understanding and is written in such a way that qualified workers can replicate the key elements on the basis of the information given.

ii) Review: An article of an extensive survey on one particular subject, in which information already published is compiled, analyzed and discussed. Reviews are normally published by invitation. Proposals of suitable subjects by prospective authors are welcome.

iii) Research note: (maximum of three printed pages): (a) An article on a new finding or interesting aspect of an ongoing study which merits prompt preliminary publication in condensed form, a medium for the presentation of (b) disclosure of new research and techniques, (c) topics, opinions or proposals of interest to the readers and (d) criticisms or additional proofs and interpretations in connection with articles previously published in the society journals.

**3. Language:** Manuscripts should be written in clear, concise and grammatically correct English so that they are intelligible to the professional reader who is not a specialist in any particular field. Manuscripts that do not conform to these requirements and the following manuscript format may be returned to the author prior to review for correction. The full form of any abbreviation or acronym should be given in the text when the term is first used.

**4. Units:** Use of SI units is mandatory. Journal style is to use the form S m-1, A m-2, W m-1 K-1, not S/m, A/m2, W/m.K.

**5. Style of manuscript:** It is important that the file be saved in the native format of the word processor used. The text should be in single-column format. The manuscripts should be submitted in double-spaced typing, 12 points Times New Roman font, on consecutively numbered A4 pages of uniform size with 3.0 cm margin on the left and 2.0 cm margins on top, bottom and right. The manuscript must be presented in the order: (1) title page, (2) abstract and key words, (3) text, (4) references, (5) appendices, and (6) list of captions, each of which should start on a new page. All papers should be limited to 20 pages.

**Essential title page information**

**Title:** Concise and informative. Titles are often used in information-retrieval systems. Avoid abbreviations and formulae where possible.

**Author names and affiliations:** Where the family name may be ambiguous (e.g., a double name), please indicate this clearly. Present the authors' affiliation addresses (where the actual work was done) below the names. Indicate all affiliations with a lower-case superscript letter immediately after the author's name and in front of the appropriate address. Provide the full postal address of each affiliation, including the country name, and, if available, the e-mail address of each author.

**Corresponding author:** Clearly indicate who will handle correspondence at all stages of refereeing and publication, also post-publication. **Ensure that telephone and fax numbers (with country and area code) are provided in addition to the e-mail address and the complete postal address.**

**Present/permanent address:** If an author has moved since the work described in the article was done, or was visiting at the time, a "Present address" (or "Permanent address") may be indicated as a footnote to that author's name. The address at which the author actually did the work must be retained as the main, affiliation address. Superscript Arabic numerals are used for such footnotes.

**Abstract:** An abstract must state briefly and clearly the main object, scope and findings of the work within 250 words. Be sure to define all symbols used in the abstract, and do not cite references in this section.

**Keywords:** Between three and six keywords should be provided below the Abstract to assist with indexing of the article. These should not duplicate key words from the title.

Subdivision-numbered sections: Divide your article into clearly defined and numbered sections. Subsections should be numbered 1.1 (then 1.1.1, 1.1.2, ...), 1.2, etc. (the abstract is not included in section numbering). Use this numbering also for internal cross-referencing: do not just refer to "the text". Any subsection may be given a brief heading. Each heading should appear on its own separate line.

**Introduction:** This section should include sufficient background information to set the work in context. The aims of the manuscript should be clearly stated. The introduction should not contain either findings or conclusions.

**Materials and methods:** This should be concise but provide sufficient detail to allow the work to be repeated by others.

**Tables:** Tables should be numbered consecutively in accordance with their appearance in the text and referred as, for example, 'Table 1'. Tables must not appear in the text but should be prepared on separate sheets. They must have captions and simple column headings. Place footnotes to tables below the table body and indicate them with superscript lowercase letters. Avoid vertical rules. Be sparing in the use of tables and ensure that the data presented in tables do not duplicate results described elsewhere in the article. Captions should be 10 pt, and centered. Tables should be self-contained and complement, but not duplicate, information contained in the text.

**Figures:** All graphs, charts, drawings, diagrams, and photographs are to be referred to as Figures and should be numbered consecutively in the order that they are cited in the text. Figures should be cited in a single sequence throughout the text as ‘Fig. 1’, ‘Fig. 2’, …. Figures must be photographically reproducible. Figure captions must be collected on a separate sheet. Figures are normally reduced in a single column of 84 mm width. All lettering should be legible when reduced to this size.
i) Photographs should be supplied as glossy prints
and pasted firmly on a hard sheet. When several photographs are to make up one presentation, they should be arranged without leaving margins in between and separately identified as (a), (b), (c)... Magnification must be indicated by means of an inscribed scale.
ii) Line drawings must be drafted with black ink on white drawing paper. High-quality glossy prints are acceptable.
iii) Color printing can be arranged, if the reviewers judge it necessary for proper presentation. Authors or their institutions must bear the costs.
iv) Axis labels should be of the form: Stress (MPa), Velocity (m s-1).
v) Each figure must be supplied in digital form as a separate, clearly named file. Acceptable file formats are TIFF and JPEG. Images should be saved at a resolution of at least 600 dpi at final size (dpi=dots or pixels per inch; 600 dpi=240 dots per centimeter). Do not save at the default resolution (72 dpi). Crop any unwanted white space from around the figure before sizing.

**Equations:** Equations are numbered consecutively, with equation numbers in parentheses flush right. First use the equation editor to create the equation. Be sure that the symbols in your equation are defined before the equation appears, or immediately following. Refer to “Eq. (1),” not “(1)”. If what is represented is really more than one equation, the abbreviation “Eqs.” can be used.

**Results and discussions:** Results should be presented in a logical sequence in the text, tables and figures; repetitive presentation of the same data in different forms should be avoided. The results should contain material appropriate to the discussion.

**Conclusions:** Although a conclusion may review the main points of the paper, it must not replicate the abstract. A conclusion might elaborate on the importance of the work or suggest applications and extensions. Do not cite references in the conclusion as all points should have been made in the body of the paper. Note that the conclusion section is the last section of the paper to be numbered. The appendix (if present),acknowledgment (if present), and references are listed without numbers.
**Acknowledgements:** The source of financial grants and other funding must be acknowledged, including a frank declaration of the authors’ industrial links and affiliations. Financial and technical assistance may be acknowledged here.

**References: Reference style: Elsevier (numeric with Title)**
Text: Indicate references by number(s) in square brackets in line with the text. The actual authors can be referred to, but the reference number(s) must always be given.
Example: '.... as demonstrated [3,6]. Barnaby and Jones [8] obtained a different result ....'
List: Number the references (numbers in square brackets) in the list in the order in which they appear in the text.

**i) Journals:** [1] Author name(s), Article title, Journal title. Journal volume (Year) Pages. DOI
[1] A. Etemad, G. Dini, S. Schwarz, Accumulative roll bonding (ARB)-processed high-manganese twinning induced plasticity (TWIP) steel with extraordinary strength and reasonable ductility, Materials Science and Engineering: A. 742 (2019) 27–32. https://doi.org/10.1016/j.msea.2018.10.119.

**ii) Books**
[2] W. Strunk Jr., E.B. White, The Elements of Style, fourth ed., Longman, New York, 2000

**iii) Conference**
[3] F. Douglis, Th. Ball, Tracking and viewing changes on the web, in: Proc. 1996 USENIX Technical Conference, 1996.

**6.Reviewing:**
Every manuscript receivesreviewing according to established criteria.

**7. Revision of manuscript:** In case when the original manuscript is returned to the author for revision, the revised manuscript together with a letter explaining the changes made, must be resubmitted within three months.

**8. Proofs:** The corresponding author will receive the galley proofs of the paper. No new material may be inserted into the proofs. It is essential that the author returns the proofs before a specified deadline to avoid rescheduling of publication in some later issue.

**9. Copyright:** The submission of a paper implies that, if accepted for publication, copyright is transferred to the Iron and Steel Society of Iran. The society will not refuse any reasonable request for permission to reproduce a part of the journal.

**10. Reprint:** No page charge is made. Reprints can be obtained at reasonable prices.

# International Journal of Iron and Steel Society of Iran

*Subscription Order Form, 2022*

| | |
|---|---|
| Name: | Institution: |
| Mailing Address: | |
| Zip Code: | Country: |
| Telephone: | Fax: |
| E-mail: | |
| Date: | Signature: |

Please check the appropriate box to receive your annual subscription of
**International Journal of Iron and Steel Society of Iran**

| | Iran | Other Countries |
|---|---|---|
| ☐**Individual** | ☐**Rls 2000000** | ☐**US$ 100** |
| ☐**Institutional** | ☐**Rls 3000000** | ☐**US$ 200** |

Payments should be made via ISSI current account #. 0202831627002 Bank Melli Iran, Isfahan University of Technology Branch, Code: 3187. The receipt should be sent to ISSI Address:

**Iron & Steel Society of Iran**
No A306, 12th street, Isfahan Science and Technology Town,
Isfahan University of Technology, Isfahan, 84156-83228, Iran.
Tel: +98 31 33932121-24 Fax: +98 31 33932125
Web: journal.issiran.com E-mail: journal@issiran.com

# International Journal of

# ( Int. J. of ISSI )

# Iron & Steel Society of Iran

## *Contents*

**Iron & Steel Society of Iran**
**No A306, 12th street, Isfahan Science and Technology Town,**
**Isfahan University of Technology, Isfahan, 84156-83228, Iran.**
**Tel: +98 31 33932121-24 Fax: +98 31 33932125**
**Web: journal.issiran.com E-mail: journal@issiran.com**